THE INITIAL CONDITIONS OF STAR FORMATION

Nicholas Edgar Jessop

Presented for the Degree of Doctor of Philosophy

The University of Edinburgh
1998

This thesis is dedicated to my parents and my grandparents.

ACKNOWLEDGMENTS

The last four years has seen some astounding progress in science; animal cloning, discoveries of extra solar planets, production of Bose-Einstein condensates, as well as the production of the first molecular computer (albeit it a Bucky Ball abacus), and tantalizing hints of possible extra terrestrial life in the shape of a Martian meteorite (which seems to have had a more profound effect on NASA funding than life sciences).

I would first and foremost like to thank all the staff at the JCMT (with particular reference to Tim Jennes and Jim Pomeroy), the CPCC and the University of Kent (especially Andy Gibb) for supplying and advising on the Stenholm Code. Helpful advice from Matthew Yates, Phillipe Andre, Mark Casali and Peter Brand (in profuse amounts) has also been welcomely received. I would also like to thank my supervisor Derek Ward-Thompson.

I would like to thank several others for conversations; Henry Buckley, Matthew Horrobin, Neil Francis, Frederique Motte, Deborah Ruffle and Andrew Harrison.

Many people have been supportive over the past 4 years, including my parents and sister, Ross, Mike, Paul and Ford (OK he wasn't really supportive). Other people like Al, Rob and Iain have reminded me there is a lot more to life than work. Thanks to all the other PhD students in the department for putting up with me and occasionally taking me out for a few beers (that especially means Richards Knox). Finally thank you to anybody has helped me, whom I may not have mentioned.

This thesis is my own composition except where indicated in the text.

February 2, 1999

ABSTRACT

This thesis is a study of the physical conditions typical in regions of the Inter Stellar Medium which are likely to go on to form stars. In recent years considerable progress has been made in the understanding of low mass star formation following various studies of opaque regions in near by parts of the Galaxy. The regions' high densities and high opacities make them favourable environments for star formation to occur.

Using the IRAS Sky Survey Atlas a number of high latitude clouds are selected, and optical depth maps of these clouds are constructed. The most opaque regions in these clouds are identified and catalogued as a set of cloud cores. The column density and mass of each core is calculated. The majority of the cores are found to be gravitationally bound, and a small fraction are found to have signs of protostellar content; they contain IRAS point sources within them with spectral characteristics typical of Protostars or embedded Young Stellar Objects. An analysis of the typical properties of this set of cores and the typical properties found in previous studies of more opaque and more dense regions in the Inter Stellar Medium reveals that the timescale in which a cloud core forms a protostar decreases as both the opacity and density of the core increases. The results compare well with physical models of star formation in which the prestellar evolution is regulated by ambipolar diffusion, and the strong influence of various sources of ionization on the star formation timescale is discussed.

The very earliest protostars typically have a massive infalling envelope (visible in submillimetre continuum and molecular line observations), vigorous outflows, and radio emission due to shocks. The latter two processes are thought to be powered by the dynamically infalling envelope. Cores without any sign of protostellar content often contain dense regions similar in mass, but less dense, than the protostars' envelopes. Dense and massive enough to go on to form stars, these objects are precursors to the protostars; prestellar cores. A high resolution submillimetre study of a subset of these cores carried out with the JCMT in Hawaii is presented. Various isotopes of CO were detected towards the cores. One core in particular, L1689B, proved bright enough to map over a considerable region in both $C^{18}O(J=2\rightarrow1)$ and

$C^{18}O(J=3 \rightarrow 2)$. All these observations are presented.

In order to fully interpret the observations of L1689B, and to compare its properties with theoretical models of the early stages of star formation, a parameterised representation of L1689B is modelled with a radiative transfer code in order to produce predicted maps which can be compared with the observations. It is found that simple models of L1689B, assuming an isothermal gas temperature and constant abundance cannot adequately account for L1689B's appearance. Either a temperature drop or a drop in CO abundance towards its centre are needed to explain the observations. Neither however are uniquely implied by the $C^{18}O$ observations alone. A reanalysis of a submillimetre continuum map of L1689B is made, and using these results the degeneracy is partly lifted. L1689B appears to have a fall in CO abundance towards the centre, and perhaps a drop in temperature, both of which could be causally linked one to the other, or more likely, both of which are dependent on an external factor like the lack of ultra violet penetration towards the centre. Either way it is shown that the central region of L1689B may be unsupported by pressure gradients, and susceptible to rapid free fall unless the existence of magnetic fields is assumed. This core seems to be being supported by magnetic fields and evolving by ambipolar diffusion.

Contents

Chapter 1

Introduction

1.1 Star Formation: Models and Their Predictions

A complete theory of star formation should be able to predict the history and rate of star formation needed to explain the number of stars, and the observed distribution of stellar masses in a galaxy (known as the Initial Mass Function, or IMF), as well as the observed distribution of binary stars and star clusters. It should also predict the observed evolution leading to the birth of a main sequence star with its various stages: diffuse interstellar medium; molecular cloud; molecular clump; prestellar core; protostar; T-Tauri star and finally main sequence star (all these terms will be explained more fully later in the text). Part of this evolution is illustrated in figure 1.1. Star formation is typically studied with two different approaches (see Lada 1985): One approach examines global or macroscopic processes which govern where and how star formation occurs in galaxies or molecular clouds; the second investigates the formation and evolution of individual objects with the goal of describing and understanding the lifespan of protostars.

The initial mass function was first derived by Salpeter (Salpeter 1955) by analyzing the luminosity function of stars in the solar neighborhood. This luminosity function reveals that the number of stars of low intrinsic luminosity are more common per unit volume than those of high intrinsic luminosity. Furthermore, the number of high luminosity stars drops off more quickly than the low luminosity ones (there is an increase in the gradient of the the luminosity function) due to high luminosity stars burning $\sim$ 10 percent of their core hydrogen content quickly and then turning off the main sequence. When Salpeter took into account, amongst other things, stellar lifetimes he found that the the initial mass function, f(m), which is defined as the probability that a star should form in a given volume and have an initial

mass between m and dm is described by

$$f(m)dm \propto m^{-2.35}dm. \tag{1.1}$$

Further work (see Scalo 1986 for an extensive review) has revealed that in addition to following the general power law form there are two peaks at m $\sim$ 0.3 $M_{\odot}$ and at 1.2 $M_{\odot}$. The high mass peak may be a result of the observed bimodal nature of star formation which is inferred from observations of star forming clouds (which is discussed later) while the low mass peak may suggest a preferred minimum mass. This minimum mass could have two explanations (Shu, Adams & Lizano 1987, SAL 1987 hereafter), either that the ISM preferentially produces stars of that mass or that the prestellar evolution is the cause; the building up of a protostar's mass by accretion is only halted by a universal process like an outflow triggered by the onset of thermonuclear fusion.

Most stars occur in binary or multiple systems, of which one of the earliest studies was by Abt and Levy (1976). They claimed that high separation binaries (with orbital periods greater than 100 years) show little link between the partner masses, while low separation binaries (orbital periods less than 100 years) tend to have similar mass partners. They also found that the distribution of the companion stars (secondaries) is also different between the two types of binaries; the low separation binaries have more high mass secondaries than low mass, while in contrast the high separation binaries have more low mass secondaries than high mass (eg the slope of the IMF of low separation binary secondaries has the opposite sign to that for the IMF of field stars and high separation binary secondaries). It has been suggested that the high separation binaries may be the the result of fragmentation of the prestellar cloud core while the low separation binaries result from a partner forming within the disk of a protostar (SAL 1987) - See figure 1.1. These results have been critically assessed since Abt and Levy (1975). Duquennoy and Mayor (1991) found that in their sample of binaries no distinction between secondary distributions conclusively existed between high and low period binaries, and reviewed the work on selection effects carried out since the original Abt and Levy paper. However later work still, (Mazeh, Goldberg,Duquennoy and Mayor 1992), found more compelling evidence that Abt and Levys conclusions about two distinct populations are correct.

Galactic star formation is observed to occur in molecular clouds (SAL 1987) and individual stars form from either small, low mass clouds or from clumps which are located within a larger cloud (Beichman et al 1986). The masses of a molecular cloud may be as large as $10^{7}M_{\odot}$ and the radius 10^{17}m. A star can be as small as $10^{-1}M_{\odot}$ and radius 10^{8}m (SAL). Star formation therefore involves fragmentation and collapse of the ISM and increases in density over many orders of magnitude. Gravity drives collapse and various support mechanisms oppose it, including thermal pressure, turbulence, angular momentum and perhaps most importantly magnetic support which requires partial ionization of the gas (see Mestel and

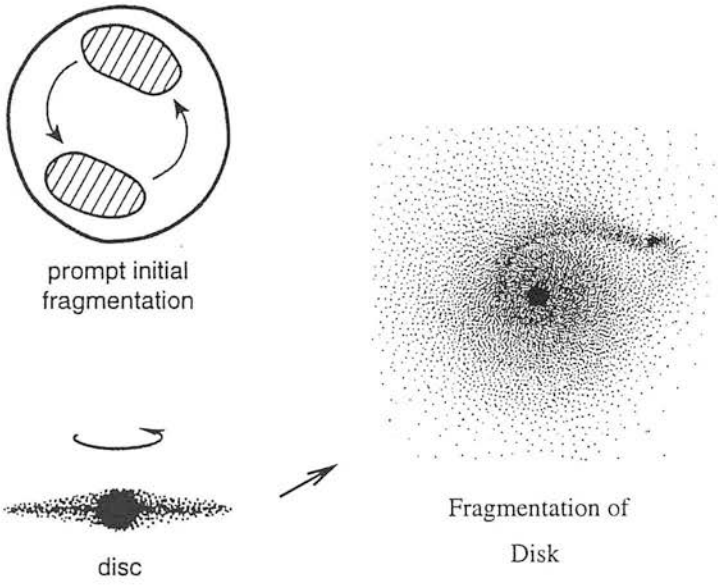

Figure 1.1: Figure showing Fragmentation of the prestellar core leading to two wide binaries, and fragmentation within a protostellar disk leading to close formation binaries, images from from Clark (1995) and Adams & Benz (1992).

Spitzer 1956 for an early discussion). The different support mechanisms may be more or less important at different evolutionary stages and may interact with each other. There are several apparent problems which can only be explained once the support mechanisms are understood.

Magnetic fields offer considerable support (depending on the degree of ionization - McKee 1989) because the field is 'frozen in' ie the magnetic field lines move with the gas, and the magnetic flux per surface density of gas therefore stays constant. This can only be overcome by ambipolar diffusion which is believed to be the main way in which a cloud contracts (Mouschovias 1991). The gas is free to collapse along the field lines unless there is a significant amount of MHD turbulence - in which case Alfvén waves support the cloud parallel to the magnetic field lines (Gammie and Ostriker 1996). The star formation time scale in a magnetically supported cloud is therefore likely to be considerably longer than the free fall time scale of most clouds,which is estimated to be 10^4 to 10^6 years (Zuckerman and Palmer 1974). This helps to explain why molecular clouds are observed so widely, and have derived lifespans longer than the free fall timescales.

One major problem is why typical velocities observed in molecular clouds tend to be highly supersonic. If due to turbulence these motions would lead to collisions between supersonic flows, and the associated shocks would convert kinetic into thermal energy (Scalo 1987). The existence of magnetic fields can help

explain the large velocities without the need for large inputs of energy to maintain them over sustained periods, because the velocities of Alfvén waves are generally larger than the thermal velocities and are perhaps large enough to explain the observed linewidths (Mouschovias 1991).

Cloud cores tend to be modeled as having initially aligned magnetic field lines running through them, and connecting to interstellar material exterior to the cloud (Lublow & Pringle 1996, Boss 1997). This scenario then allows an explanation of how the cloud cores loose excess angular momentum as they contract: The rotation of the core produces a torque in the magnetic field, and a 'kink' in the field lines. This 'kink' is propagated outwards from the core to the exterior interstellar medium in the form of Alfvén waves (Mestel and Spitzer 1956, Mouschovias and Paleologue 1980). The core feels a drag opposing its spin, the exterior a torque due to the magnetic field lines, and a net transfer of angular momentum occurs from the core to the interstellar medium.

One expects considerable feed back of kinetic energy into the cloud once star formation occurs due to bipolar outflows (observed in almost every young stellar object) and high velocity winds. In the case of high mass star formation considerable UV emission and even supernovae will also feed energy into the clouds. These events can feed energy into the supporting turbulence and Alfvén waves, and an overall equilibrium may be reached. McKee (1989) also suggests that ionizing radiation from Cosmic Rays may have a strong regulatory effect and suggests possible steady state situations were a constant rate of star formation within a cloud part supports it and prevents total collapse.

The overall star formation efficiency appears to be very variable within the galaxy. One can define the star formation efficiency (SFE) in a cloud as,

$$\mathrm{SFE} = \frac{\mathrm{M}_*}{\mathrm{M}_* + \mathrm{M}_{\mathrm{cloud}}} \tag{1.2}$$

where M_* is the total mass of stars in a cloud and $\mathrm{M}_{\mathrm{cloud}}$ is the mass of gas in the cloud. The star formation efficiency is estimated to be about 2 percent in the first galactic quadrant (Myers et al 1986) but must have been 20 to 50 percent for the observed bound clusters and appears to be that high in Ophiuchus (Lada and Wilking 1984). In the galaxy as a whole it is thought that gas turns to stars in a period of about 10^9 years (SAL 1987) (a small fraction of the Hubble time), implying that either the present time is particularly active in the forming stars or that extra material is being fed into the ISM, possibly from a galactic halo or high latitude clouds.

Clearly a process of such complexity, and with such well defined constraints as those discussed above (ie IMF, binary fractions, and efficiency), will prove very difficult to describe fully. Therefore this thesis aims to study the simple case of prestellar evolution in isolation, and in particular the initial state

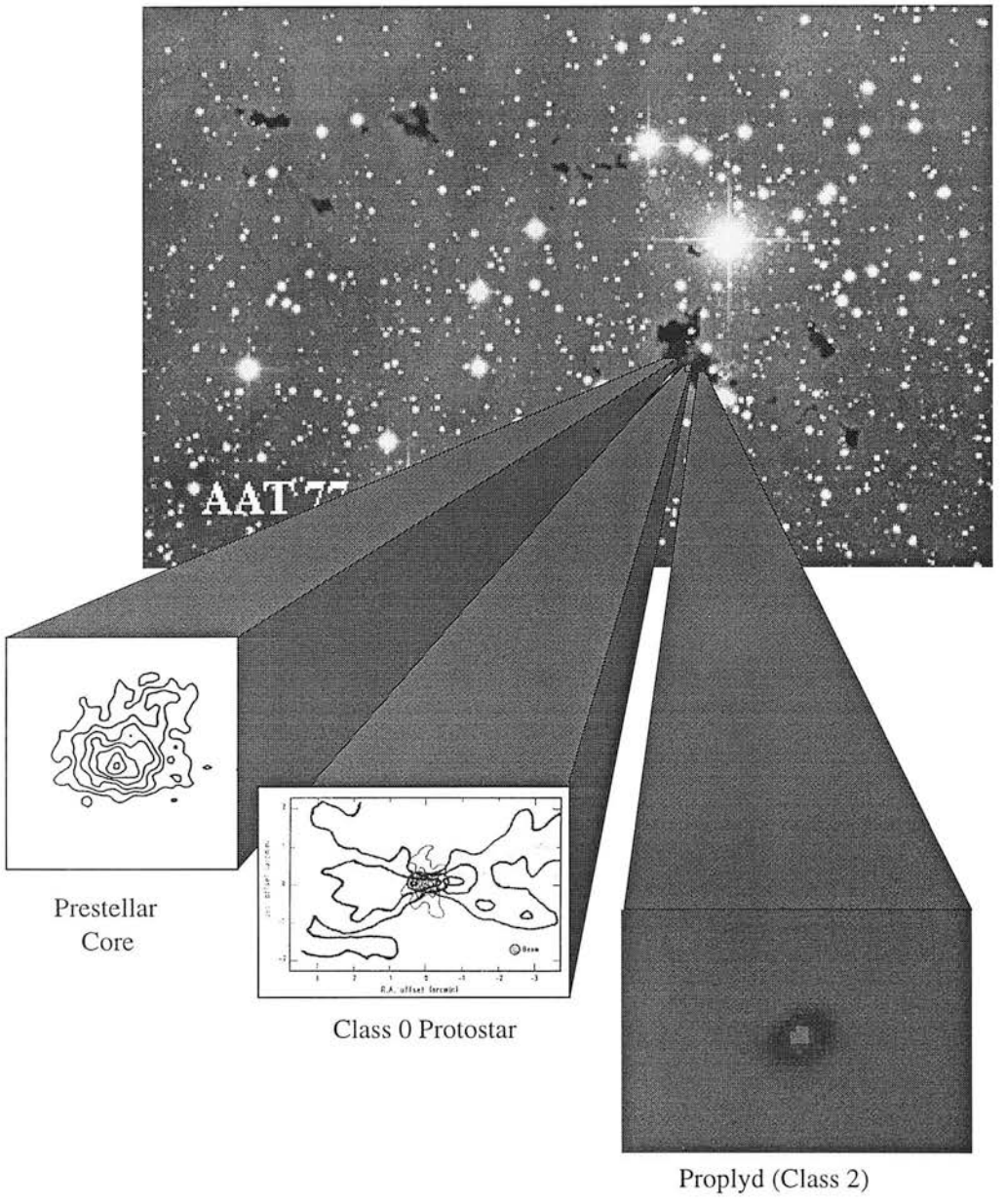

Figure 1.2: Schematic illustrating the postulated evolution of a star forming Bok Globule, first it forms a prestellar core which on collapse creates a protostar with bipolar outflow, this then evolves towards a main sequence star with an obscuring disk (in the near infrared and optical). Bok globule image taken from the Astronomy Picture of the Day www page, credit and copyright of image David Malin, Anglo Australian Observatory, image of prestellar core L1689B from Andre et al 1996, image of B335 protostar from Chandler et at 1990, image of proplyd from the Astronomy Picture of the Day www page , imaged with the HST. The Astronomy Picture of the Day www page can be found at http://antwrp.gsfc.nasa.gov/apod.

for such evolution, the prestellar core. A prestellar core can be defined as the phase in in which a gravitationally bound fragment has formed in a molecular cloud and is evolving to progressively higher degrees of central condensation eventually leading to the protostellar collapse and evolution illustrated in Figure 1.2 (Ward-Thompson et al 1994; Andre, Ward Thompson and Motte 1996), and described in section 1.7. First however I discuss the global and macroscopic processes observed in the ISM.

1.2 Components of the Interstellar Medium.

The interstellar medium is mainly hydrogen and helium, the main products of the big bang. Helium constitutes about 10 percent of the total number of atoms in the universe and 25 percent of the total mass. The hydrogen is either in ionized, atomic or molecular form. In addition approximately 2 percent by mass of the local ISM is made up of elements more massive than He and 2 percent by mass is made up of interstellar dust.

The atomic hydrogen can be probed by its 21cm line emitted when an electron switches its spin from anti-parallel to the proton's spin to parallel to it. This transition has a low excitation energy. There are two major advantages inherent in using this line to study the galaxy and its contents; the galaxy is transparent in the transition in almost all directions, and much of the galaxy is cold and therefore can only be probed with lines with low excitation temperatures (see Combes 1991). HI probes all of the cold atomic hydrogen in the galaxy.

In molecular hydrogen an electron cannot 'flip' its spin due to the Pauli exclusion principle. In addition it belongs to the set of symmetric molecules which as discussed by Penzias and Burrus (1973), does not have a dipole moment. The lowest energy transitions are due to quadrapole transitions between rotational levels, and because of the molecule's low moment of inertia, occur at wavelengths shorter than 28μm. In order to excite the molecule into the upper rotational levels the temperature of the gas must be greater than 510K (see McCartney 1997). Because the vibrational transitions have an even larger energy (they are typically in the infrared) and need high excitation temperatures they also do not trace the cold ISM. The molecular material in the ISM is generally very cold and most molecular hydrogen cannot therefore be seen in emission. Only the warmer or more excited regions such as shocks and photodissociation regions are directly observable with molecular hydrogen transitions in emission.

The cold hydrogen in a region can however be directly observed by looking for H_2 absorption features in the UV continuum of background stars (eg Savage et al 1977) - however this approach is limited to suitable lines of sight. Similar work exists studying atomic hydrogen in emission but is limited generally

to studies of the local ISM (ie the nearest 30-200pc) because of the high abundance and opacity of the lines, (see Cox and Reynolds 1987, Paresce 1984, Diamond et al 1995 and Dring et al 1997). The main benefit in both these types of study to the more general surveys of the ISM is the correlations revealed between hydrogen column density and the optical extinction due to dust.

Generally 'tracers' of the hydrogen must be used to observe the cold components of the ISM. The two tracers most commonly used are carbon monoxide (which has low energy millimeter rotational transitions) and dust which absorbs light in the optical regime and produces continuum emission throughout the infrared and sub-millimetre (Hildebrand 1983, Lynds 1962, Beichman 1987). Both have many limitations inherent in the fact that they are tracers of the molecular hydrogen, the principle amongst them are that the abundance of molecular species is dependent on cloud chemistry; and the abundance and form of the dust is dependent on the formation process and environmental history. In addition molecular transitions have a low range of optical depths in which the lines can be detected (in a reasonable time) and before the lines become optically thick. Further problems like selective photodissociation - where the less abundant isotopomers of a species are depleted with respect to the more abundant ones, due to greater exposure to dissociating radiation - also have to be considered (eg Greaves, Ohishi, White and Sunada 1995).

Figures 1.3, 1.4 and 1.5 show examples of the extensive studies made of the ISM: early work studying optically opaque dark dust clouds (Lynds 1962); a survey of the CO emission in the galactic plane (Dame et al 1987); the far infrared all sky survey produced by the IRAS satellite; and the recent Leiden/Dwingeloo HI survey (Hartmann and Burton 1997). The large scale fields which play an important role in the behaviour of the ISM are the radiation, magnetic and gravitational fields.

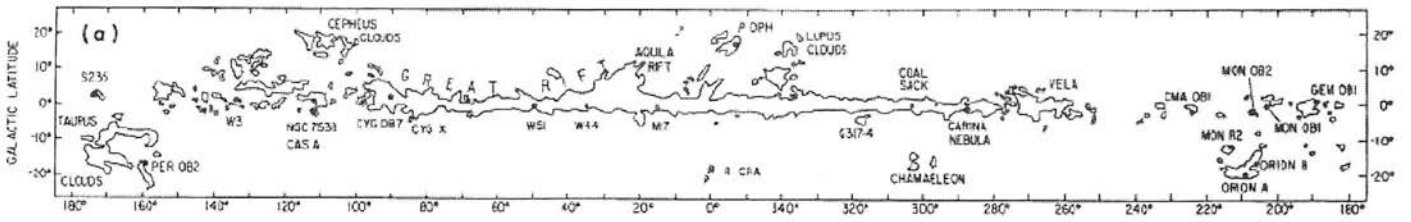

Figure 1.3: CO Survey of the Galactic Plane (Dame et al 1987) and Lynds Dark Nebulae atlas (Lynds 1962). The CO survey is a composite of several smaller individual surveys. CO has velocity information which in many ways is more informative than this projected intensity map - the spiral arms and galactic centre both stand out very clearly in velocity position diagrams. The survey only covers regions within 20 degrees of the galactic plane at most. The Lynds work only covers the galactic plane from galactic longitude -10 degrees to 250 degrees. The different shades of grey correspond to different levels of opacity. Both maps show similar structures, notably considerably more structure and a larger scale height towards the galactic centre.

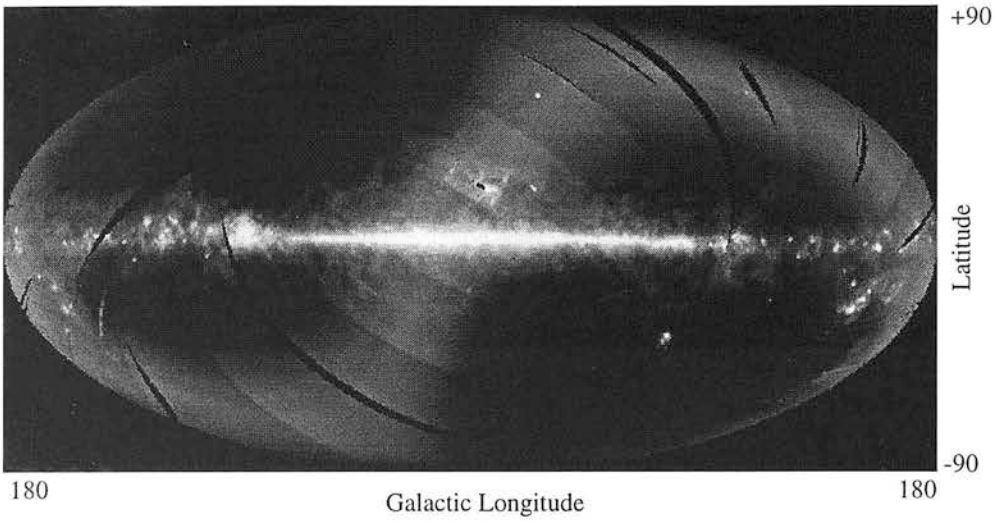

Figure 1.4: IRAS all sky survey. The survey traces similar structures to both the CO and Lynds surveys, it does however cover the whole sky (apart from limited zones of avoidance) and is made up of 4 different wavelengths. The fainter 's-like' structure is from zodiacal emission. Image from the IPAC World Wide Web page http://www.ipac.caltech.edu/

1.3 Structure of the Interstellar Medium.

The exact delineation between components is difficult, due largely to the self similarity of the ISM on all scales from spiral arm complexes down to 0.01 pc scales (Elmegreen and Falgarone 1996, Turner 1996). There are several reviews in the literature on the structure of the ISM and the molecular clouds (eg: Scalo 1985, Turner 1996).

The ISM can be broken down into several different components, which in order of increasing density are: the Hot Inter Cloud Medium; the Warm Inter Cloud Medium; Warm HI; HI clouds; H_2 diffuse clouds; and H_2 dense clouds. HII regions and Supernova remnants are additional components of the ISM which have been significantly altered. HII regions are ionized by UV radiation from high mass stars. Supernovae emit energy in many different forms including radiation and high energy particles which shock the ISM. HII regions and supernova remnants therefore constitute the components of the ISM most obviously affected by high mass star formation. The H_2 diffuse clouds and H_2 dense clouds can be subdivided into Cirrus, Diffuse clouds, Translucent clouds, Cold dark clouds (with a structure ranging from complexes to individual clouds to cores and clumps) and Giant Molecular Clouds (again with a structure of complexes, major fragments, warm clumps and hot cores). Typical values for each component are listed in Table 1.1.

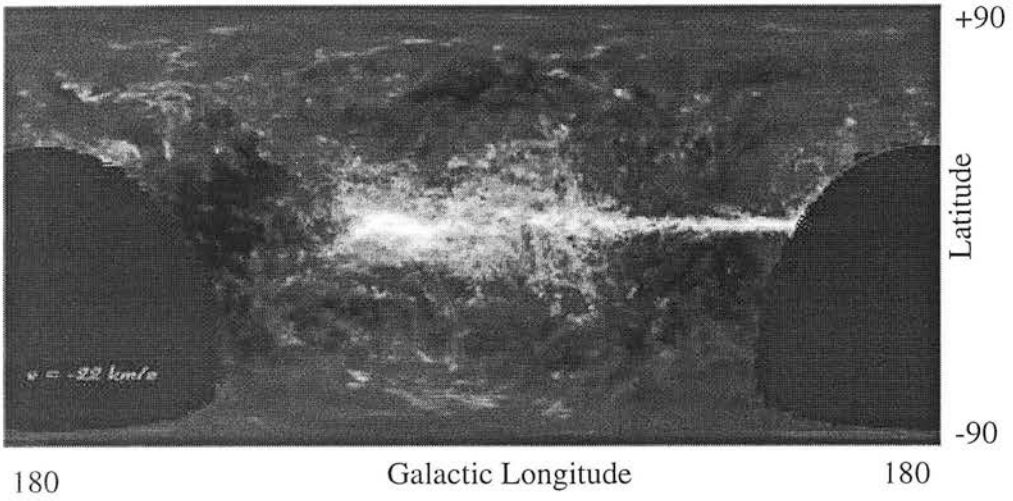

Figure 1.5: Leiden/Dwingeloo HI survey. The survey is limited in sky coverage. The HI scale height is considerably larger than the scale height of the dust and molecules. HI also has velocity information: this image is centred round -22 km/s where the emission peaks toward the galactic centre; in contrast at 22 km/s the emission peaks away from the galactic centre. Image from the NFRA World Wide Web page http://www.nfra.nl/nfra/projects/leidenHI.htm

Table 1.1: Summary of cloud properties (from Turner 1996).

Component	Size(pc)	Density(cm^{-3})	Temperature(K)	A_V(mag)
Cirrus	10-30	10-50	30-150	0.3
Diffuse Clouds	1-5	100-800	30-80	< 1
Translucent Clouds	0.15-1	500-4000	13-35	1-5
Cold Dark Clouds				
Complex	6-20	100-1000	> 10	1-2
Cloud	0.2-4	100-10000	> 10	2-5
Cores	0.05-0.4	$10^4 - 10^5$	10	5-25

Scalo (1985) suggests a hierarchy for cloud structure. On 1kpc scales Superclouds exist, which are apparently in virial equilibrium and extend up to 200pc above the galactic plane. These can be broken down into several distinct Extinction Complexes of 20-100pc, which can be separated into two types, Cold Dark Complexes or Giant Molecular Clouds. Although both types are seen to form stars, only in the Giant Molecular Clouds are OB stars formed. Individual clouds have typical sizes of 1-10pc and make up the Extinction Complexes. These clouds themselves can be resolved into separate clumps or cores as small as 0.1pc on scale.

The observed distribution of atomic material (Koo, Heiles and Reach 1992) is less confined to the galactic disk than the molecular material (Thaddeus 1991) and supported away from the plane by supernovae and OB associations. The interstellar clouds grow through coalescence and accretion of intercloud material (Elmegreen 1990) before beginning to contract under self gravity. As it accretes and contracts (increasing its mass and density respectively) a cloud's opacity increases. When its extinction of ultra violet photons from the inter stellar radiation field (which dissociates molecular hydrogen) becomes great enough then molecular H_2 and CO are no longer destroyed. The formation of molecular hydrogen is thought to be difficult (due to the lack of low energy transitions which might carry excess energy away) and a third body (like a dust grain surface) might be needed (Duley and Williams 1984).

With the onset of molecule formation and a significant amount of self gravitation, the pressure must increase if overall equilibrium is to be maintained. Several other support mechanisms also oppose or slow the collapse of interstellar clouds (rotation, turbulence and magnetic fields).

Cold Dark Clouds can cool to temperatures by cooling through molecular lines and the dust continuum (Whitworth et al 1998). They are observed to occur equally within and between spiral arms. They occur close to the galactic plane ($z < 80$pc) and are therefore seen only locally (at distances less than 300pc). Giant molecular clouds in contrast are in general warmer, more massive and situated near spiral arms (Turner 1996).

1.4 Dynamics of Interstellar Clouds and Interstellar Clouds

Larson (1981) studied the relations between line widths, cloud size and cloud masses for molecular clouds over 6 orders of magnitude in scale. He found a correlation between the cloud radius (R) and the mass (M) which is now believed to be of the form $M \propto R^2$. This relation implies that all clouds tend to have a constant column density strongly supporting the argument by McKee (1989) that there is an equilibrium point for clouds where the tendency to collapse, which increases with optical depth because ionization

levels decrease (producing a proportional decrease in the ambipolar diffusion timescale), as does external heating, is balanced by newly formed stars supplying energy to the cloud on large scales sizes.

Larson also found a correlation between line width (σ) of CO and cloud radius, of the form $\sigma \propto R^{0.38}$. Larson used the line-width relation to argue that the support is turbulent (for simple Kolmogoroff turbulence $\sigma \propto R^{0.33}$). Solomon et al (1987) carried out a similar work and found after subtracting the thermal component that $\sigma \propto R^{0.5}$, which can be used to argue that the clouds are near virial equilibrium (Combes 1991) and leads to the mass radius relation discussed above. Combes strongly argued against any simple explanation; he showed that the observed relationships might simply be due to selection effects and the natural result of a large number of random clouds being detected in each line of sight. Scalo (1987) also argues strongly against any simple explanation: the whole system is extremely complex, with a large amount of energy being supplied to the clouds at all scales due to various feedback mechanisms like outflows, Supernovae, and expanding HII regions. The simple Kolmogorov derivation assumes incompressible flows and energy input only at the largest scale, and is clearly not able to represent the complex observed behaviour of the ISM.

Ordered magnetic fields can support partially ionised material in two ways. It can support the gas in the direction parallel to the field lines through MHD turbulence in the form of Alfvén waves (Gammie and Ostriker 1996). Support of the gas perpendicular to the field lines due to ion/neutral collisions can also occur and is only overcome by ambipolar diffusion (Mouschovias 1990). In both of these support mechanisms the ionization level in the gas is the critical physical parameter which controls the efficiency of the support. Both the damping timescale of the Alfvén waves and the ambipolar diffusion timescale are inversely proportional to the ionization level (Mouschovias 1990, Ruffle et al 1998). It is generally thought that support parallel to the field lines is lost at an earlier stage in the evolution of a cloud than the support perpendicular to the field lines (Ruffle et al 1998).

The ionization level falls as the ionizing ultraviolet radiation penetrating into the cloud drops, and only once the ionization level drops far enough can MHD turbulence decay, and ambipolar diffusion allow a cloud to condense and collapse (McKee 1989). The magnetic and UV fields, and their key supporting role, add further complication to any description of the dynamics of the ISM and further prevent simple explanation.

Of the divisions suggested between components of the ISM, one of the strongest is that between warm Giant Molecular Clouds and Cold Complexes (Lada 1995). There are two modes of star formation, a high mass mode which always forms clusters and a low mass mode which might produce isolated or distributed stars, or low mass clusters. Why such a difference is observed is controversial although one long standing

suggestion is that the star formation process lasts for several 10^7 years and the low mass distributed mode occurs first (Herbig 1962). Cold Complexes may be massive enough to form bound clusters of low mass stars (eg Ophiuchus), but the GMCs form and then commence high mass star formation only after encountering the spiral arms. Stars of spectral type O and B have short lifetimes. Virtually all known OB associations are spatially associated with GMCs and they often show a sequential progression in age with the youngest often interacting with the cloud in the form of a shock wave which propagates further bursts of star formation (Lada 1995).

1.5 Isolated Star Formation in Cores.

Low mass star formation is observed to occur in dense cores observed in isolation (as Bok Globules), in small molecular clouds and in GMCs. If the subsequent evolution is largely determined by the core's properties and relatively independent of external influences one might expect a generic evolutionary history leading to the formation of protostars. Determining this evolutionary track, even given that it might describe only how a minority of stars form, would be a major step forward in the study of star formation: it would offer a comparison for further studies of star formation as a whole. This is one of the goals to which this thesis is aimed.

The starting point of an observational study of isolated star forming cores is to look for extremely dense, gravitationally bound regions in cold molecular clouds. The most successful study of such objects so far was carried out by Myers, Linke, and Benson (1983), in which they selected 149 regions of high opacity on the Palomar sky survey plates. They studied these regions in molecular transitions with a resolution of 1-2 arcmins.

Beichman et al (1986) then identified associations of these cores with IRAS sources and found approximately one-half of them had IRAS sources - of which one-third were T-Tauri stars and the remainder were undetected in the optical. This was used to argue that the associated stars were very young, and that in at least half of the cores star formation is taking place. Beichman et al (1986) went on to find that the only statistically significant difference between the cores with stellar sources and without was that the line width of the cores with stellar sources was larger; presumably because they had energy fed in by stellar winds or bipolar outflows from their embedded stars. The fact that the two types of core are so similar begs the question; do cores without sources go on to form stars? The timescale from protostellar collapse, to optically visible T-Tauri star is $\sim 10^6$ years (Beichman 1987), and to main sequence star is $\sim 10^7$ years (D'Antona and Mazzitelli 1997); so do the other cores represent the evolution which takes

place on a similar timescale before dynamical collapse?

Similar work has been carried out in order to identify gravitationally bound Bok Globules (isolated small molecular clouds) visible from the northern hemisphere (Clemens and Barvainis 1988) and from the Southern Hemisphere (Bourke, Hyland and Robinson 1995). Clemens and Barvainis (1988) found that 30 percent of the globules had IRAS Point Source Catalogue (PSC) sources in the cores; of these 10 percent were thought to be field stars and 10 percent were thought to be other chance associations. The percentage of their catalogue of low mass isolated clouds (Bok globules) with embedded YSOs, roughly 25 percent, seems therefore to be less by a factor of 2 than the number of Myers' cloud cores with embedded YSOs. This difference may be due to the different selection procedures (there was a two step approach in the Myers sample, regions of high optical obscuration were first picked out for a follow up $C^{18}O$ and NH_3 survey). However if the above assumption is correct, that the globules without YSOs represent evolution before dynamic collapse and the globules with YSOs represent evolution after collapse, then the Bok globules in Clemens and Barvainis' sample may be taking three times longer to form stars. This is perhaps because of higher ionization rates holding up ambipolar diffusion as a result of greater exposure to the interstellar UV field. Only a detailed comparison of the physical characteristics of the different catalogues would be able to show that the Bok globules are less dense, and therefore more ionized, and presumably less evolved cores, than those in the Myers sample. Attempts to answer these questions will help to shed light on the McKee (1989) model of star formation where, ionization levels and column densities influence the timescale on which dynamic collapse sets in.

Mouschovias (1991 and references therein) has modeled how a core with a supporting magnetic field will evolve. The core develops a characteristic density profile: $\rho \propto r^{-2}$ at the outside due to the isothermal equation of state, and a flatter density profile towards the centre - a residual of the uniform initial conditions. It evolves to progressively more condensed states through ambipolar diffusion. It will shed angular momentum on at most a timescale

$$t = \frac{\rho_{cl}}{\rho_{ext}} \frac{Z}{v_{A,ext}} \tag{1.3}$$

by dissipating Alfvén waves (Mouschovias and Paleologou 1980). Z is the half thickness of the cloud and $v_{A,ext}$ is the Alfvén velocity in the external medium, ρ_{ext} and ρ_{cl} are the densities of the external medium and cloud respectively. For typical physical parameters t is a few 10^6 years.

The observed density profiles of cloud cores are in general very similar to the predicted profiles, Myers showed that they had an r^{-2} profile at large radii. Ward-Thompson et al (1994) followed this up with higher resolution observations which showed flattened inner profiles. Andre et al (1996) showed that at outer radii the density profile fell to an r^{-3} profile ensuring that cloud cores have an outer radius and a

finite mass. Further observational work has shown that the cores undergo chemical evolution consistent with slow contraction (Kuiper et al 1996, Bergin and Langer 1997), and they also have spectral signatures consistent with ambipolar diffusion (Myers et al 1996).

High resolution observational work therefore supports the belief that the cloud cores in the various catalogues of Myers et al (1983), Clemens & Barvainis (1988), and Bourke, Hyland & Robinson ((1995) are magnetically supported and condensing through ambipolar diffusion. Although charged particles like the ions, electron and dust particles are effectively tied to the magnetic field lines, the neutrals are not. These are free to move with respect to the field lines, under the influence of gravity, but when doing so experience a drag mainly due to collisions with the ions. A mathematical description of the process is given in chapter 2 which follows the treatment of Spitzer (1978). Mouschovias' model of core evolution shows that the magnetic flux reduces in the centre of the core so one can think of the process as one in which magnetic flux diffuses out of the gas. This means that the cores will evolve to a point where magnetic support is no longer capable of supporting the core against dynamic collapse. This occurs when the core loses enough magnetic flux (due to ambipolar diffusion) to satisfy the following inequality for gravitational instability of a magnetically supported core:

$$M_{cr} > 0.13\Phi G^{1/2} \sim 10^3 M_\odot \left(\frac{B}{10_{\mu G}}\right)\left(\frac{R}{2pc}\right) \tag{1.4}$$

as discussed in SAL (1987). Here Φ is the magnetic flux per unit surface area density and B is the magnetic field strength. R is the radius of the cloud.

Although it is generally assumed that the cores are isothermal it is worth noting that they may well be governed by a more complex equation of state. If the heating rate is lower towards the centre, possibly due to a low radiation field penetrating into the interior of the core, or the cooling is more efficient in the centre (cooling is thought to be mainly a result of CO and dust radiation), then the core may well be cooler in the centre (see Krugel & Chini 1994, and Tohline, Bodenheimer & Christodendau 1987).

This thesis is a study of cloud cores and the initial conditions prior to star formation. However before setting out the questions which are to be tackled in the rest of this work, a discussion of protostellar evolution and the various uncertainties in our knowledge of protostellar evolution will help illustrate why a study of the initial conditions prior to dynamical collapse in cloud cores affects the evolution of protostars and is of importance.

1.6 Protostellar Evolution

At some point the magnetic field is no longer able to support the core and it will collapse. There has been significant theoretical work on dynamical collapse (Larson 1969, Shu 1977). However most of it neglects the magnetic fields. Mouschovias' work only goes to a number density $n \sim 10^{12}cm^{-3}$ and though there seems to be ongoing progress aimed at understanding the later evolution (eg Li and Mckee 1996), no work has fully incorporated magnetic fields into a model of protostellar evolution. When collapse does occur it is expected that a disk will form at the radius where the infalling material's angular momentum provides enough support against gravity. This disk then feeds a hydrostatic protostar. Work ignoring magnetic fields clearly illustrates just how the initial conditions for collapse are important and may well be qualitatively similar to the evolution of a magnetically super critical core.

Larson analysed the evolution of a constant density, isothermal core of initial mass $2.5M_{\odot}$ and density $10^{-19}gcm^{-3}$ (Larson 1969). In such a core, the constant temperature and density mean that there are no pressure gradients. Therefore the whole cloud collapses in free fall (ie there are no retarding forces). As the material falls inwards a pressure gradient arises in the outer region which retards the flow, but in the inner region free fall is maintained. This means that the density at the centre increases more quickly than at the outside. The outer core develops a density profile of the form $\rho \propto r^{-2}$ while the inner region maintains a homologous density distribution. Collapse throughout the core continues until the central density, $\rho_c \sim 10^{-14}gcm^{-3}$ when a small central region becomes sufficiently optically thick to trap the heat generated by the infall. This leads to a temperature increase which increases the pressure and deceleration occurs. A hydrostatic opaque core forms at the centre, and a shock is formed at the boundary between this core and the unretarded free falling material. This first core does not last long. On a timescale of $\sim$ 1 year the temperature increases to $\sim$ 2000K and the H_2 begins to dissociate into atomic hydrogen. This leads to a dynamically unstable situation and free-fall collapse of the core ensues. A second hydrostatically supported core is created when all the hydrogen is finally dissociated, and again at the surface of this core a shock front exists, due to free falling material accreting onto it. As the density of the infalling material onto this core decreases the opacity of the infalling material will decrease also, and begin to allow a significant amount of energy to be radiated away from the shock front, this allows the core to cool, condense and contract. All this evolution occurs within 10-100 years (a typical profile is given in Figure 1.6) and the first core will have disappeared by the end of this time. Because this timescale is very short this evolution is unlikely to ever be observed.

Following this short but eventful period the main accretion of a protostar is thought to occur. Because this process occurs on a much longer timescale (hundreds of thousands of years) it is more likely to be

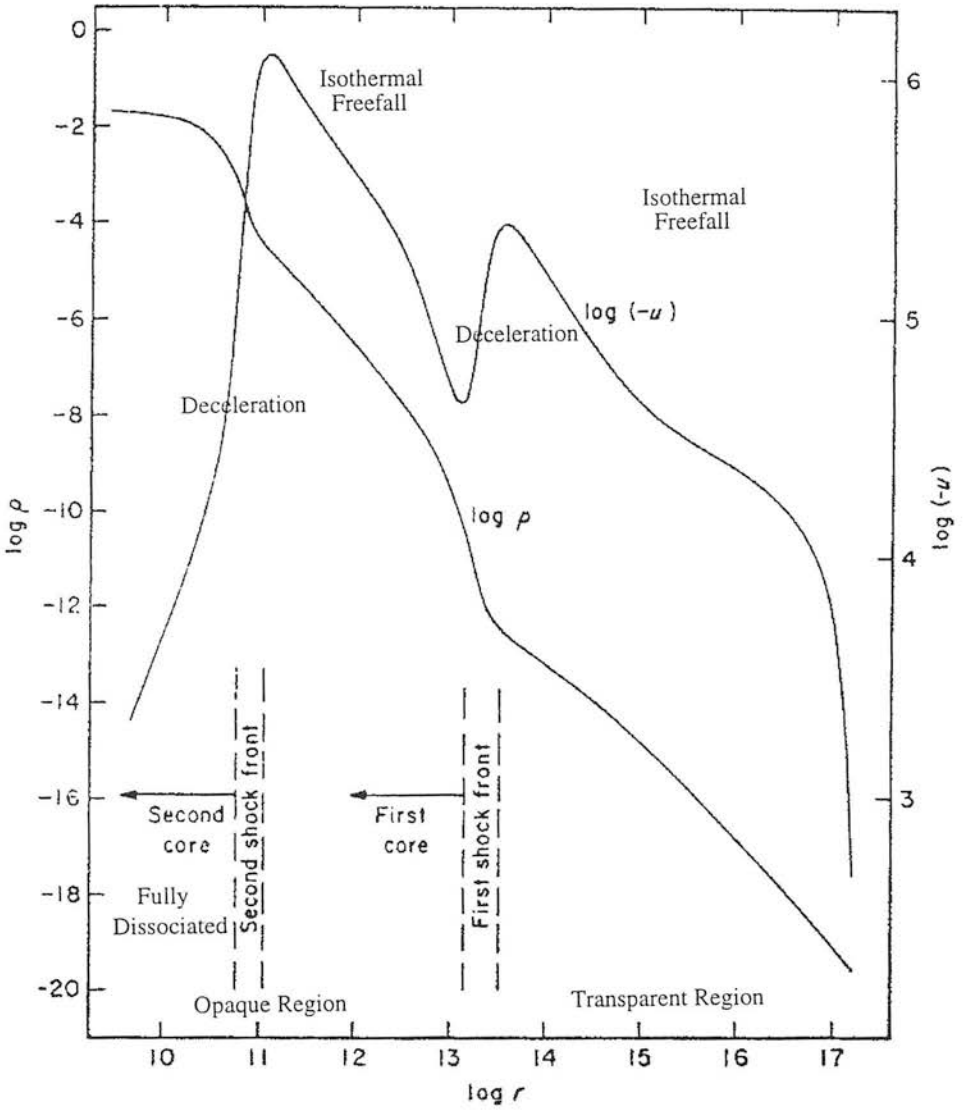

Figure 1.6: Figure from Larson (1969) showing the density profile, ρ, , and velocity profile, u, of a collapsing core as a function of radius, r.

observed. Most theoretical work in the past 30 years has concentrated on this stage. Larson believed that during the main accretion phase the luminosity of a protostar would increase during the period where the first half of its mass was accreted and reduce as the second half of its mass accretion proceeds. Shu argued that the collapse of a singular isothermal sphere ($\rho \propto r^{-2}$) was much more likely and physically realistic. He argued that this profile can be produced from a wide number of different initial conditions and is due to the natural tendency of an isothermal self-gravitating gas to approach detailed mechanical balance. The critical assumption leading to $\rho \propto r^{-2}$ profile is of isothermality. He then showed that collapse occurs first at the centre and a collapse expansion wave propagates out from the centre at the sound speed. Two other key features of his model are that accretion occurs at a constant rate (the mass of the central object is predicted to be a^3t/G where a is the isothermal sound speed, t the time and G the gravitational constant) and the gas flows are subsonic (Shu 1977). Foster and Chevalier (1993) showed that the accretion from a critical, isothermal Bonner Ebert sphere has a fast initial rate, which slows with time. McLaughlin and Pudritz (1997), showed that in the case of a non isothermal sphere the accretion rate is dependent on the equation of state, but is slow at first and increases with time, if the central region is cooler than the outside.

Clearly therefore even in the absence of an accurate model for infall, which successfully incorporates magnetic fields, a study of the evolution of cloud cores towards the onset of dynamical collapse will prove very important, and necessary to define the appropriate initial conditions influencing the way in which the formation of a star occurs. In particular it appears that the density and temperature profiles will strongly influence the manner in which accretion onto a protostar proceeds.

Observations of protostars have shown that the central accretion source becomes visible early on in the far infrared, at a time when the overall luminosity of the protostars is still dominated by its gaseous envelope. The subsequent evolution can be broken down into four different stages, or 4 different classes of YSO. Class 0 sources are believed to be at the earliest stage of protostellar evolution (Andre et al 1993). These Class 0 sources are characterized by very strong submillimetre continuum emission from a massive envelope, while only having weak or even no detectable emission shortwards of 10 microns. They are thought to be approximately 10^4 years old and their high ratio of submillimetre to bolometric luminosities suggest there is more mass in their envelopes than in the central stellar objects (Andre et al 1997). These Class 0 protostars already have bipolar outflows, often have strong radio emission (presumably linked to the accretion shock or the outflow) and develop in a relatively short timescale to protostars which have less than half their mass yet to accumulate (Class I sources) and significantly longer lifetimes (Ward-Thompson 1996). These Class I sources originally identified by Lada (1987) emit in the near-infrared, having rising spectral energy distributions from 2μm to 60 μm. They have moderate

submillimetre emission - the original demarcation between Class 0s and Class Is is that the ratio of bolometric luminosity to submillimetre luminosity should be less than 200 for a Class 0 (Andre et al 1993). The Class Is protostars generally also have weaker outflows than the class Os (Andre et al 1997). On completion of the accretion of the envelope these protostars develop into T-Tauri stars which accrete from a disk only and cool down the Hayashi tracks: Class IIs represent T-Tauri stars with a disk (Classical T-Tauri stars) and are observationally associated with YSOs which show a flat or falling spectral energy index in the 2μm to 60 μm range (Lada 1987); Class IIIs represent T-Tauri stars without a disk and can be modeled as reddened black bodies (weak line T-Tauri stars).

1.7 The aims of this thesis.

Before describing the aims of this thesis it is worth reiterating for clarity two points already discussed. Firstly catalogues of cloud cores are usually made up of a reasonably tightly distributed and similar set of objects, and each catalogue tends to have an associated column density, number density, size and mass which is typical of the cores catalogued. Secondly a core can be thought of as prestellar if it satisfies the following definition: a prestellar core is defined as the phase in which a gravitationally bound fragment has formed in a molecular cloud and is evolving to progressively higher degrees of central condensation eventually leading to the protostellar collapse. The aims of this thesis are twofold.

First given the already known differences in star formation rates in different environments, and with a wide variety of properties, cloud cores should be selected in order to investigate amongst other things how the star formation timescale is dependent on physical conditions, especially column density of material. With the availability of submillimetre continuum and spectral line arrays the area of the sky mappable and size of survey possible will increase significantly so that detailed follow up work is possible.

Therefore in the first half I present a method of finding star forming cores using a far infrared data base, the IRAS Sky Survey Atlas. Most surveys to date have started from optical plates which in general are limited by coverage (obscuration is only clear near the galactic plane), and dynamical range (the optical depth for $A_v > 4$ regions cannot be derived). Hence the first half of this thesis asks: are the cloud cores I catalogue forming stars, and if so how many? What are the typical physical conditions of the catalogued cores? Then I compare how the fraction of cores forming stars and the physical conditions compare with other surveys.

The second half of this thesis aims to study a small selection of cores in submillimetre spectral lines in order to investigate the following: Are the density profiles consistent with the ambipolar diffusion models

and the assumption that they are indeed the pre dynamic collapse stage of star formation? If so what are the physical characteristics? What are the density profiles? Are the cores isothermal? Is there any evidence of chemical reactions or molecule/dust interactions? And finally what are the implications on the existing theories of star formation if these cores represent the initial conditions of dynamical collapse and protostar formation?

This introduction has been brief. It is an attempt to review the current understanding of star formation, to present critical assumptions which will be held throughout the thesis, and to offer justification for the work presented. Several issues raised will be discussed more fully at appropriate areas in the remainder of this thesis.

Chapter 2

Physics of Star Formation

2.1 Introduction

In the introduction chapter of this thesis a general review of star formation was presented, with particular emphasis on the aspects which are particularly relevant to, and motivate, the work presented in this thesis. Several physical processes were discussed, and here I present a more detailed discussion of the physics which will be used later in the thesis.

First I discuss the physics describing the production and transfer of radiation within the molecular clouds observed. This has to be understood in order to interpret the appearance of the clouds, and derive their physical properties.

Secondly I discuss several of the key support mechanisms. Generally in describing the interstellar medium, the real density, velocity and temperature structures cannot be modelled in a comprehensive way. However certain robust properties of a cloud, like physical time scales, length scales and masses can be derived which enable one to predict the physical state (whether it is in stable equilibrium, or gravitationally unstable) of the cloud and hence predict its future evolution. In particular I will discuss pressure support, the Jean's Criteria for gravitational stability, magnetic support, and the ambipolar diffusion velocities and time scales.

2.2 Observing the ISM: Radiative Transfer

2.2.1 The Equation of Radiative Transfer

Consider a beam of radiation at frequency ν, with intensity I_ν, incident on a slab of gas of thickness dx. If one defines, the fractional absorption per unit mass in the slab as κ_ν, the emission coefficient per unit length ϵ_ν, and the emission coefficient per unit mass in the slab as j_ν,

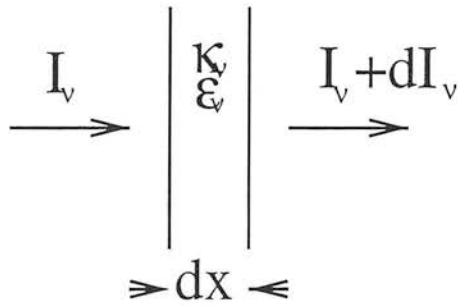

then $dI_\nu = dx\rho[j_\nu - I_\nu\kappa_\nu]$. By defining the source function in the slab as $S_\nu = j_\nu/\kappa_\nu$ and the optical depth of the slab $d\tau_\nu = -dx\rho\kappa_\nu$ then one derives the standard equation of radiative transfer (eg Emerson 1996):

$$\frac{dI_\nu}{d\tau_\nu} = I_\nu + S_\nu, \tag{2.1}$$

which on solving gives:

$$I_\nu = \int_0^\tau S_\nu \exp(-\tau_\nu)\, d\tau_\nu \tag{2.2}$$

for the emergent intensity from a cloud with no incident radiation upon it.

Thus if one knows S_ν and τ_ν along a line of sight one can calculate the intensity emergent along that line of sight - ignoring scattering into a line of sight, which is valid if I_ν is isotropic when scattering in equals scattering out.

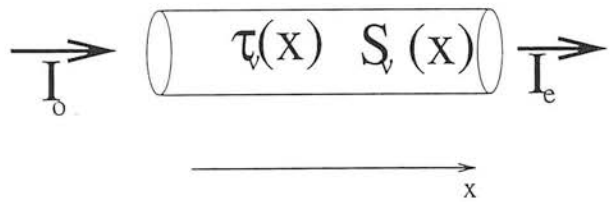

2.3 Molecular line Radiative Transfer

2.3.1 Brightness and Radiation Temperatures

At submillimetre and radio wavelengths it is often standard to measure the intensity in different units - either the Brightness Temperature T_B or the Radiation Temperature T_R such that,

$$T_r = \frac{c^2}{2k}\frac{I_\nu}{\nu^2} \tag{2.3}$$

$$I_\nu = B_\nu\,(T_B) \tag{2.4}$$

where c is the speed of light, k is Boltzmann's constant and $B_\nu\,(T)$ is the blackbody function. For $\frac{h\nu}{kT_B} \ll 1$ (the Rayleigh Jeans assumption) then $T_B = T_R$.

2.3.2 Frequencies of Rotational Transitions.

Rotational transitions of molecules more massive than H_2 are important in studies of dense and cool regions of the ISM because of the low excitation energies needed to excite the molecules out of the rotational ground state. These energies are typically less than the kinetic energy of individual H_2 molecules, even in the coolest regions of the ISM. Rotational transitions in comparison tend to only be observed in hotter gas or regions exposed to a strong ultraviolet radiation field (McCartney 1997).

For linear rigid rotators quantum mechanics states that

$$E_{rot} = J(J+1)\left(\frac{h}{2\pi}\right)^2\frac{1}{2I} = hBJ(J+1) \tag{2.5}$$

where I is the moment of inertia of the rotator, J is the rotational excitation level, and B is the rotational constant. For non rigid rotators I is not constant but increases with increasing J leading to higher order corrections.

2.3.3 Dipolar Transitions.

If the rotator has an electric dipole (arising from a displacement of the centre of charge and therefore mass of the protons, with respect to the centre of charge, and likewise mass, of the electrons in the molecule) then it can make transitions between excitation levels by emitting or absorbing a photon but only if it obeys the selection rule $\delta J = \pm 1$. This means that one will get a photon which is emitted if a rotator

makes the radiative transition from the J + 1 level to the J level or absorbed if the rotator makes the radiative transfer from J to J + 1 which has frequency (in the rotators inertial frame)

$$\begin{aligned} \nu &= \frac{\delta E}{h} \\ &= 2B\,(J+1) \end{aligned}$$

As mentioned above, in non rigid rotators I is not constant but increases as J increases leading to higher order corrections so that

$$\nu = 2\mathrm{B}\,(\mathrm{J}+1) - 4\mathrm{D}(\mathrm{J}+1)^3 \tag{2.6}$$

. where D is a lower order rotational constant.

2.3.4 The Einstein probabilities for radiative transitions.

If the spontaneous transition rate from upper level j to lower level i is denoted $\mathrm{A_{ji}}$ and the absorption rate from a radiation field of mean intensity, J_ν, (which is obtained from averaging I_ν over all directions and should be clearly differentiated from the emission coefficient per unit mass, j_ν, introduced earlier) is $4\pi \mathrm{J}_\nu \mathrm{B_{ij}}$ then the transition rate of stimulated emission of a photon is $4\pi \mathrm{J}_\nu \mathrm{B_{ji}}$.

One finds that

$$\mathrm{A_{ji}} = \left(8\pi \mathrm{h}\nu^3/\mathrm{c}^2\right) \mathrm{B_{ij}}, \tag{2.7}$$

$$\mathrm{B_{ij}} = \left(\mathrm{g_j}/\mathrm{g_i}\right) \mathrm{B_{ji}} \tag{2.8}$$

and that the spontaneous transition rate $\mathrm{A_{ji}}$ is related to the electric dipole moment, $\mathbf{d_{ji}}$, (given by $(Z_1 + Z_2)e\mathbf{r}_{ji}$ where $\mathrm{Z_1}$ is the atomic number of the first atom, $\mathrm{Z_2}$ the atomic number of the second, and $\mathbf{r}$ is the time averaged displacement of the centre of mass of the protons with respect to the centre of mass of the electrons in the molecule)

$$\mathrm{A_{ji}} = \frac{64\pi^4}{3\mathrm{hc}^3 4\pi\epsilon_0} \nu^3 \mid d_{\mathrm{ji}}^2 \mid \tag{2.9}$$

eg Emerson, (1996).

2.3.5 $\mathrm{d}\tau_\nu$ and S_ν from the Einstein Coefficients.

One can see that if $\mathrm{N_i}$ and $\mathrm{N_j}$ are the number densities of the atom or molecule in the excitation level i or j then:

$$\kappa_\nu \rho = (N_i B_{ij} - N_j B_{ji})\, h\nu \phi_\nu \tag{2.10}$$

where the term ϕ_ν has been introduced to represent line broadening and which when integrated over all frequencies should equal 1. Likewise

$$j_\nu \rho = \frac{1}{4\pi} (N_j A_{ji} h\nu)\, \phi_\nu \tag{2.11}$$

which implies that

$$d\tau_\nu = dx(N_i B_{ij} - N_j B_{ji}) h\nu \phi_\nu \tag{2.12}$$

and

$$S_\nu = \frac{\left(\frac{2h\nu^3}{c^2}\right)}{\left(\frac{N_i g_j}{N_j g_i} - 1\right)} \equiv B_\nu\,(T_{ex}^\nu) \tag{2.13}$$

where T_{ex} is the excitation temperature, and can be calculated from the two population levels relevant to the transition from equation 2.15. The degeneracy of level i has been denoted by g_i, the degeneracy of level j by g_j. The equation of radiative transfer becomes:

$$T_B^\nu = \int_0^\tau T_{ex}^\nu e^{-\tau_\nu} d\tau_\nu. \tag{2.14}$$

2.3.6 Local Thermodynamic Equilibrium

If in a slab the level populations of the molecule or atom are described by the Boltzmann distribution of temperature T then,

$$\frac{N_j}{N_i} = \frac{g_j}{g_i} e^{\frac{-E_{ij}}{kT}} \tag{2.15}$$

and

$$S_\nu = B_\nu\,(T)\,. \tag{2.16}$$

Using the alternative form of Boltzmann's equation

$$\frac{N_i}{N} = \frac{g_n}{U} e^{\frac{-E_{ij}}{kT}} \tag{2.17}$$

which introduces the number density of the molecule N, and the partition function U where;

$$U = \sum_j g_j e^{\frac{-E_j}{kT}} \tag{2.18}$$

one gets an expression for the optical depth

$$d\tau_\nu = \frac{dx U N B_{ij} h\nu \phi_\nu}{g_n} \left(e^{\frac{h\nu}{kT}} - 1\right). \tag{2.19}$$

Hence in LTE if one knows N(x) and T(x) one can solve the equation of radiative transfer.

2.3.7 The Rate Equation

If Boltzmann's distribution does not describe the populations then one has to use the rate equation to calculate the level populations:

$$\frac{dN_j}{dt} = -N_j \sum_{k,y} R^y_{jk} + \sum_k N_k \sum_y R^y_{kj} \tag{2.20}$$

where R^y_{jk} is the rate of transition from level j to level k via the mechanism y, and R^y_{kj} is the rate of transitions into level j from the level k via the mechanism y (both these terms have units of s^{-1} and in general will include radiative and collisional transitions). The left hand side of the equation is the rate of change of the population level j. The first term on the right hand side is the number of transitions out of j and the second term on the right hand side is the number of transitions into j.

For a gas where the transitions are either dipolar radiative or due to collisions with H_2,

$$-N_j \sum_{k,y} R^y_{jk} = -N_j \left(A_{j\to j-1} + 4\pi J_{\nu_{j\to j-1}} B_{j\to j-1} + N_{H_2} \sum_k C_{jk} \right) \tag{2.21}$$

and

$$\sum_k N_k \sum_y R^y_{kj} = N_{j-1} 4\pi J_{\nu_{j\to j-1}} B_{j-1\to j} + N_{H_2} \sum_k N_k C_{kj}, \tag{2.22}$$

where C_{jk} is the average transition rate of the molecule from the the level j to the level k due to a collision with an H_2 molecule. One can see that population levels are dependent on the radiation field and an iterative procedure has to be used in order to find a consistent solution for level populations and the radiation field.

2.4 The Jeans Mass and Free Fall Timescale.

A critical factor which will influence whether the cores observed in molecular clouds will go on to form stars is whether they are gravitationally bound. The Jeans mass gives a mass at which a cloud is expected to be in equilibrium. The Jeans argument essentially compares the pressure support of a cloud with its self gravity. If a cloud or core is below the Jeans mass it is dominated by pressure forces and is probably just a manifestation of random pressure fluctuations in the ISM. If it is at the Jeans mass the core is in or close to hydrostatic equilibrium. If its mass is well above the Jeans mass the core is either free to collapse unrestrained by thermal pressure forces or being supported by some other mechanism.

Derivation of the Jeans mass starts with the basic fluid equations;

$$\frac{\partial \rho}{\partial \mathrm{t}} + \boldsymbol{\nabla} \cdot (\rho \boldsymbol{v}) = 0, \tag{2.23}$$

$$\frac{\mathrm{D}\boldsymbol{v}}{\mathrm{Dt}} + \frac{\boldsymbol{\nabla}\mathrm{p}}{\rho} = -\boldsymbol{\nabla}\Phi, \tag{2.24}$$

$$\nabla^2 \Phi = 4\pi \mathrm{G}\rho, \tag{2.25}$$

which are the continuity equation, Newton's IInd law and Poisson's equation respectively. ρ is the volume density, $\boldsymbol{v}$ is the fluid velocity, p is the pressure, and Φ_0 is the gravitational potential. Jeans (1902)started by considering a fluid with zero velocity and constant density. In order to simplify the calculation isothermality is assumed so that $\mathrm{p} = \mathrm{p}(\rho)$ and the fluid is initially described by ρ_0, p_0, Φ_0. If this fluid is then perturbed to a state, $\rho_0 + \rho_1$, $\mathrm{p}_0 + \mathrm{p}_1$, $\boldsymbol{v}_1$, $\Phi_0 + \Phi_1$, then to first order,

$$\mathrm{p}_1 = \frac{\partial \mathrm{p}_0}{\partial \rho_0}\rho_1 \tag{2.26}$$

and Newtons second law can be expressed as,

$$\frac{\partial \boldsymbol{v}_1}{\partial \mathrm{t}} + \frac{\partial \mathrm{p}_0}{\partial \rho_0}\boldsymbol{\nabla}\left(\frac{\rho_1}{\rho_0}\right) = -\boldsymbol{\nabla}\Phi_1, \tag{2.27}$$

Taking the grad of this equation and then eliminating the gravitational potential by using Poisson's equation and the $\boldsymbol{\nabla} \cdot \boldsymbol{v}_1$ term by using the continuity equation then one gets the wave equation,

$$\frac{\partial^2}{\partial \mathrm{t}^2}\frac{\rho_1}{\rho_0} - \frac{\partial \mathrm{p}_\mathrm{o}}{\partial \rho_0}\nabla^2\left(\frac{\rho_1}{\rho_0}\right) = 4\pi \mathrm{G}\rho_0 \frac{\rho_1}{\rho_0}. \tag{2.28}$$

This has a solution

$$\frac{\rho_1}{\rho_0} \propto \mathrm{e}^{-\mathrm{i}(\omega \mathrm{t} - \boldsymbol{k}\cdot\boldsymbol{r})} \tag{2.29}$$

if $\omega^2 = \left(\frac{\partial \mathrm{p}_0}{\partial \rho_0}\right)\mathrm{k}^2 - 4\pi \mathrm{G}\rho_0$. The perturbation in equation 2.29 takes the form of a sound wave if $\mathrm{k} = 2\pi/\lambda$ is large and

$$\omega^2 \sim \left(\frac{\partial \mathrm{p}_0}{\partial \rho_0}\right)\mathrm{k}^2. \tag{2.30}$$

If k is small then

$$\omega \sim \mathrm{i}\sqrt{4\pi \mathrm{G}\rho_0} \tag{2.31}$$

and the solution is similar to the exponential growth of a perturbation which occurs when the pressure is zero, on a time scale $t_{ff} = 1/\sqrt{4\pi G\rho_0}$. Because this is the time scale for collapse of an unsupported cloud it is known as the free fall time scale.

The value of λ which separates the two situations is known as the Jeans Length, λ_J, given by,

$$\lambda_\mathrm{J} = \mathrm{c}\sqrt{\frac{\pi}{2\mathrm{G}\rho_0}} \tag{2.32}$$

which using the equation for the isothermal sound speed, $c = \sqrt{kT/\mu}$ where T is the thermal temperature of the gas, k is Boltzmanns constant and μ is the average molecular mass, can be written

$$\lambda_J = \sqrt{\frac{\pi kT}{2G\rho_0\mu}} \tag{2.33}$$

The expression for the Jeans mass, can be derived by assuming a sphere of constant density, and of radius λ_J so that ignoring numerical constants one finds,

$$M_J = \left(\frac{\pi kT}{G\mu}\right)^{3/2} \frac{1}{\rho^{1/2}}. \tag{2.34}$$

It would be useful if this equation could be put into a form which expresses the Jeans mass in terms of the measured values for a core. Typically these are total mass M, distance D, solid angle Ω, and temperature T.

Assuming the core is roughly spherical and of uniform density then;

$$M \sim \frac{4\pi}{3}\rho r^3 \tag{2.35}$$

and

$$r(Au) \sim \sqrt{\frac{\Omega}{\pi}} D. \tag{2.36}$$

Equation 2.34 can therefore be reorganised in terms of the measured properties to give,

$$M_J(M_\odot) \sim \frac{0.002 \times D(pc)^{3/2}\Omega(\text{square arcmins})^{3/4}}{M(M_\odot)^{1/2}} \left(\frac{T}{25K}\right)^{3/2}. \tag{2.37}$$

The ratio of M to M_J can also be calculated

$$\frac{M}{M_J} = \frac{500 \times M(M_\odot)^{3/2}}{D(pc)^{3/2}\Omega(\text{square arcmins})^{3/4}}. \tag{2.38}$$

2.5 Magnetic Flux Freezing

In the introduction I discussed the fact that the magnetic field is frozen into the molecular clouds so that the magnetic fields comove with the ionic component in the cloud. I present here a simple derivation. A more complicated and thorough treatment is given in Mouschovias (1991)

First recall the 3 Maxwell equations,

$$\nabla \times \boldsymbol{B} = \mu_0 \left(\boldsymbol{j} + \epsilon_0 \frac{\partial \boldsymbol{E}}{\partial t}\right), \tag{2.39}$$

$$\nabla \times \boldsymbol{E} = -\frac{\partial \boldsymbol{B}}{\partial \mathrm{t}}, \tag{2.40}$$

$$\nabla \cdot \boldsymbol{B} = 0, \tag{2.41}$$

and Ohms law,

$$\boldsymbol{j} = \eta \boldsymbol{E}, \tag{2.42}$$

where $\boldsymbol{B}$ is the magnetic field, $\boldsymbol{E}$ is the electric field, $\boldsymbol{j}$ is the current flow, and η is the conductivity of the medium.

If the electrons and ions arrange themselves to set up charge neutrality $\mathrm{n_i ze} = \mathrm{n_e e}$, which suppresses high frequency plasma phenomena like the displacement current (Mouschovias 1991), then the first of the Maxwells equations quoted can be written,

$$\nabla \times \boldsymbol{B} = \mu_0 \eta \boldsymbol{E} \tag{2.43}$$

and taking the curl of this equation one can show that

$$\frac{\partial \boldsymbol{B}}{\partial \mathrm{t}} = \frac{\nabla^2 \boldsymbol{B}}{\mu_0 \eta}. \tag{2.44}$$

This is a diffusion equation for $\boldsymbol{B}$ and the typical timescale for the process can be estimated by approximating the equation to

$$\frac{\boldsymbol{B}}{\mathrm{t_{dif}}} = \frac{\boldsymbol{B}}{\mu_0 \eta \mathrm{L}^2} \tag{2.45}$$

where L is the typical length scale over which $\boldsymbol{B}$ varies so that

$$\mathrm{t_{dif}} \sim \mathrm{L}^2 \mu_0 \eta. \tag{2.46}$$

If this time scale is very much longer than other time scales of importance in the evolution of the ISM one can consider the magnetic field to be frozen into the ionic component.

2.6 Conductivity of the ISM

In order to calculate the conductivity of the ISM, one can consider the flow of electrons and ions within a partially ionised gas with an electrostatic force. In this case the electrostatic force on each electron is balanced by collisions, so that

$$\mathrm{eE} = \frac{\mathrm{m_e V}}{\tau} = \frac{\mathrm{m V_{rms} V}}{\mathrm{l}} \tag{2.47}$$

where V is the mean drift velocity of the electrons, $\mathrm{m_e}$ is the electron mass, $\mathrm{V_{rms}}$ is the root mean square velocity of the electrons and τ and l are the mean time, and length (mean free path) between collisions

respectively. One can also use Ohms law

$$j = \eta E = N_e e V \tag{2.48}$$

where N_e is the number density of electrons. On rearranging, these two equations give an expression for the conductivity,

$$\eta = \frac{N_e e^2 l}{m_e V_{rms}}. \tag{2.49}$$

The mean free path can be described in terms of the number density N and collisional cross section σ_c of the impeding particles;

$$l = \frac{1}{N\sigma_c}. \tag{2.50}$$

If most of the collisions are between electrons and neutrals then the cross section used is approximately the Bohr cross section, so that $\sigma_c \sim 10^{-16}\ cm^{-2}$. If most of the collisions are due to scattering of electrons off ionised hydrogen nuclei then Rutherford scattering gives an approximate cross section

$$\sigma_c = \frac{e^4}{(m_e V_{rms}^2 4\pi\epsilon_0)^2}. \tag{2.51}$$

Finally using the equation for the root mean square velocity of a particle,

$$V_{rms} = \left(\frac{3kT}{M}\right)^{1/2} \tag{2.52}$$

one can construct expressions for the conductivity. Mouschovias (1991) shows that for weakly ionized gases with number densities greater than $10^4 cm^{-3}$, ie dense cloud environments, the resistance is dominated by the electron-neutral collisions.

2.7 Ambipolar Diffusion

The section on flux freezing showed that the magnetic field was frozen into the ionized component of an interstellar cloud. However the neutral component is not directly supported by the magnetic field; it experiences a gravitational force which is balanced by collisions with the ionized particles supported by the magnetic field. This leads to a drift of the neutral particles with respect to the ionized particles and a loss of magnetic flux, widely referred to as ambipolar diffusion.

If one equates these two terms then

$$F = m_n g = m_n V_{AD} n_i \sigma_c V_{rms}, \tag{2.53}$$

where g is the local gravitational force, V_{AD} is the ion-neutral drift velocity and m_n is the mean neutral particle mass. It is worth remembering at this stage that the neutrals may feel more than just a gravitational force, if the cloud is not isobaric for example, it may experience a force due to pressure gradients. Therefore I write the expression for the ambipolar diffusion velocity in its most general form,

$$V_{AD} = \frac{F}{n_i \sigma_c V_{rms}}. \tag{2.54}$$

If the forcing term is purely gravitational then a typical time scale arises for ambipolar diffusion, the gravitational potential g is approximately given by

$$g \sim \frac{GM}{R^2} \sim G\rho R \tag{2.55}$$

where R is the radius of the cloud, M its mass and ρ its mass density. Using the expression $M_n n_i \sim \chi_i \rho$ which introduces the ionization fraction, χ_i then one can express the ambipolar diffusion time scale t_{AD},

$$t_{AD} = \frac{R}{V_{AD}} \sim \frac{\chi_i \sigma_c V_{rms}}{G m_n} \tag{2.56}$$

In addition to neutral-ion drifts, one can also find neutral-dust drifting, due to the dust grains themselves being charged. Cioleck and Mouschovias (1996), have studied this problem and find that the dust grains smaller than $\sim 10^{-5}$cm in radius can suffer a drop in abundance of upto a factor of 10 during ambipolar diffusion.

Chapter 3

Cloud Cores and Star Formation

3.1 Introduction

As discussed in chapter 1, stars form from the densest regions of the interstellar medium. Given the strong dependance of star formation on environment, in particular column density and number density (McKee 1989, Mouschovias 1991) and given the developments in millimetre and submillimetre instrumentation, as wide a range of cloud cores should and can be investigated for evidence of star formation. The aim of this chapter is to produce a sample of cloud cores significantly different from those studied already by others eg. Myers et al (1983) who sampled Giant Molecular Cloud cores or GMC cores, or Clemens and Barvainis (1988), and Bourke et al (1995) both of whom studied Bok Globules. I therefore present here a study of the physical properties of cloud cores within high Galactic latitude clouds, so that a detailed comparison may be made between star formation in the many different types of clouds.

The densest regions in clouds can usefully be catalogued as a set of cores. I present a sample drawn from relatively high Galactic latitude clouds, with generally lower optical depth and density than previously studied GMCs and Bok Globules. It is found that the cores contain a surplus number of IRAS point sources, with respect to what one would expect purely from chance alignments, and that these excess sources are consistent with being Young Stellar Objects- ie. some of the cores have already begun to form stars and are in the protostellar stage. The fraction of the cores in the protostellar stage, is a key constraint on star formation models because it gives an estimate of the prestellar timescale, before the formation of a hydrostatically supported stellar object. There are many observational indicators of a protostellar candidate; significant point source far infrared emission, radio continuum emission, or

outflows. However given that the only complete all sky survey available to identify protostars is the IRAS Point Source Catalogue, the fraction of cloud cores with IRAS point sources is used in a comparison of the star formation in different sets of cloud cores.

3.1.1 The Far Infrared Sky

The Infrared Astronomical Satellite (IRAS) flew in 1983 and surveyed almost the entire sky at the far infrared wavelengths of 12μm, 25μm, 60μm and 100μm. The satellite scanned across the sky and was originally designed to catalogue point sources. Subsequent work has produced 5 major astronomical data sets : the Point Source Catalog (Beichman et al 1988); the Faint Source Catalog; the Small Scale Structure Catalog; the IRAS Sky Survey Atlas (Wheelock et al 1994) and the High Resolution Galaxy Atlas (Cao et al 1997), all of which contain valuable information for studies of star formation. The survey is useful in studying star formation because it both identifies protostars, and maps the Interstellar Medium.

Young Stellar Objects, and protostars, are deeply embedded in the ISM, and can therefore be seen only at long wavelengths. In addition they have significant amounts of dust in envelopes and disks which emit a grey body spectrum peaking at these wavelengths. The Wien displacement law $\nu = 3\mathrm{kT/h}$ (k is the Boltzmann constant, h is the Planck constant and T is the temperature) gives the black body peak. This gives an expression for the wavelength (λ) at which the disks and envelopes preferentially emit

$$\lambda(\mu\mathrm{m}) \sim \frac{5000}{\mathrm{T(K)}}. \tag{3.1}$$

The Inter Stellar Medium also contains dust, and the high spatial coverage of the survey, the high dynamic range (due to it being a wideband continuum survey, but the dust being optically thin), and the resolution of the survey, means that the surface brightness images contain a wealth of information on Galactic clouds.

The ISSA is an all-sky survey of the extended infrared surface brightness, created by sampling the signal from each receiver at regular spatial intervals. The early Sky Flux Images suffered from problems of striping in the direction of the telescope scan due to different detector responsivities. The ISSA has improved the cross-scan noise to a similar level to the in-scan noise by implementing both a global and a local de-striping algorithm. There is a considerable amount of real emission at all wavelengths due to extended zodiacal dust emission which was subtracted from the ISSA images in order to produce an atlas of the sky as would be seen from outside the solar system. Residual zodiacal emission, due to errors in the subtraction model, is worst at shorter wavelengths and low ecliptic latitudes. In general the satellite

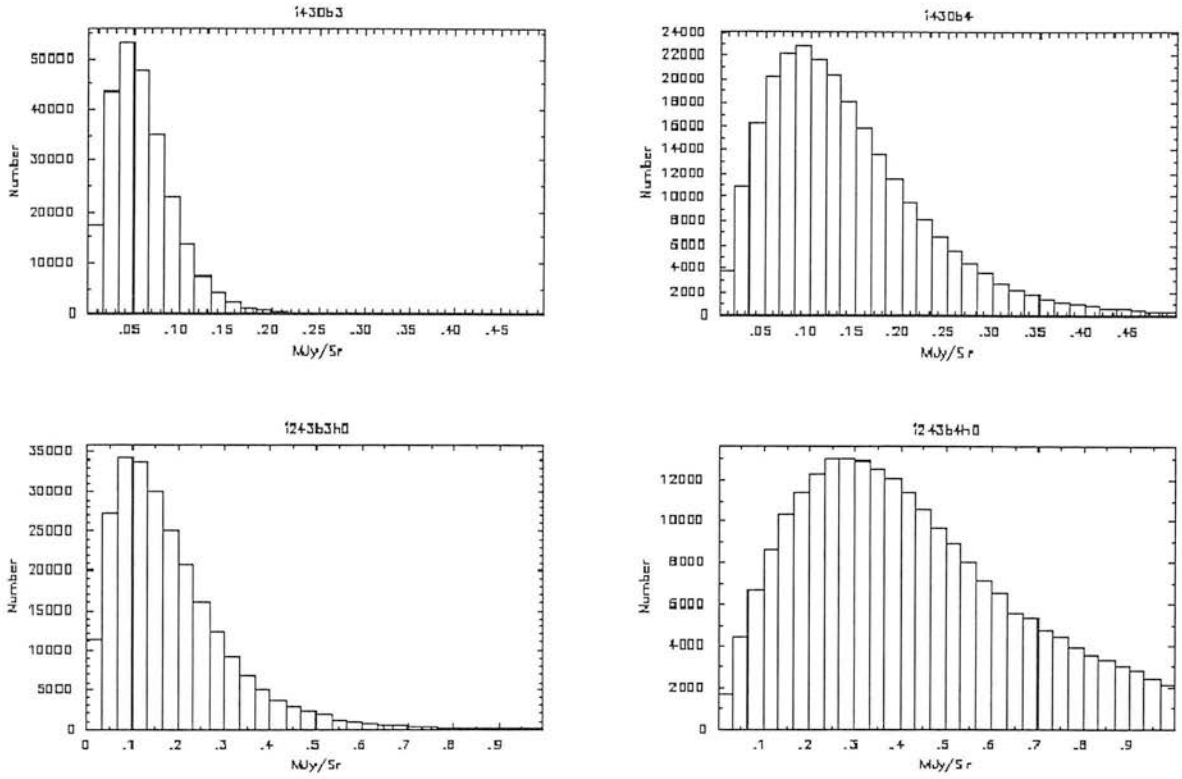

Figure 3.1: Histograms of the standard deviation of pixel values for the two sample fields.

scanned each area of sky 3 or more times at significant time intervals ie weeks and months apart, and therefore from significantly different positions in the solar system. Each such scan was known as an Hours CONfirmed (HCON) observation.

There is significant extended Galactic emission (due to the so-called cirrus clouds) which confuses emission from individual star-forming regions. An arbitrary offset in all fields is a remnant of the calibration. The accuracy of the ISSA survey can be investigated by examining the scatter in pixel values between HCONS, and the average value of the standard deviation gives an estimate of the total error associated with the calibration process. An example of the distribution of standard deviations for two fields is shown in Figure 3.1. Coadded images will be less noisy by a factor $\sim 1/\sqrt{\text{No. of HCONS}}$

The ISSA is extremely useful as an atlas of star forming regions in the Galaxy, due to the complete coverage of the sky, the dynamical range, the resolution of the survey and the number of wavelengths covered.

A single wavelength analysis which assumes that the optical depth is proportional to the intensity

is limited and so the method presented below takes images at two wavelengths in order to estimate temperature and dust optical depths.

3.2 Optical Depth Maps of Clouds

The Starlink data reduction package IRAS90 includes a routine (COLTEMP) which creates colour temperature and optical depth maps from IRAS Sky Survey maps. The method used is as follows (see IRAS90 explanatory document ID29.0 by David Berry).

The far infrared radiation emitted by a cloud of temperature T emitting a black body spectrum, $B(\nu, T)d\tau_\nu$ and absorbing $I(\nu, T)d\tau_\nu$, at an optical depth τ_ν in the cloud, leads to a flux received by an observer $f(\nu, T)$ given by:

$$f(\nu, T) = \left(1 - e^{-\tau_\nu}\right) B(\nu, T). \tag{3.2}$$

Generally τ_ν is dependent on ν in such a way that (Hildebrand 1983),

$$\tau(\nu) = \left(\frac{\nu}{\nu_c}\right)^\beta \tag{3.3}$$

where β is the emissivity index, and for wavelengths less than 300μm is taken to be less than 1 (see Hildebrand 1983). Changing the value of β does not change the structure of the optical depth maps, but will alter the final derived optical depths. However the main effect this would have in this work would be to change the derived fraction of dust observed at the IRAS wavelengths. It is almost certainly true that the value of β and the fraction of dust observed at the IRAS wavelengths varies from cloud to cloud. A detailed study of this behaviour is beyond the scope of this work, and would require additional molecular and far infrared maps of the clouds presented. Throughout this work we use the value suggested by Hildebrand (1983) of $\beta = 1$. It should be emphasised however that the values do give results consistent with studies of L1457 (see Wood et al 1994) and L1689B (see later). ν_c is the critical frequency at which the cloud becomes opaque ie. $\tau_{\nu_c} = 1$. Equations 3.2 and 3.3 lead to a 'greybody' spectrum.

Draine and Lee (1984) estimate $\tau_{100} \sim 3.6 \times 10^{-25} N_H$ where N_H is the hydrogen column density - as noted by Wood et al (1994) this means that $\tau_{100} = 1$ only for $N_H > 2.7 \times 10^{24} cm^{-2}$, a value well above even galactic plane values. Furthermore the highest value found in this study turns out to be $\tau_{100} \sim 10^{-3}$. I therefore assume that the cloud is optically thin at the wavelengths observed ($\tau_\nu \ll 1$) so

that $1 - e^{-\tau_\nu} \sim \tau_\nu$ and,

$$f(\nu, T) \sim \left(\frac{\nu}{\nu_c}\right)^{\beta} B(\nu, T). \tag{3.4}$$

The IRAS detectors were sensitive over a wide pass band and there were 4 separate wavebands (i=1,2,3,4 for 12,25,60 and 100 μm) so that the measured flux in waveband i will be

$$f_i = \int R_i(\nu) \left(\frac{\nu}{\nu_c}\right)^{\beta} B(\nu, T) d\nu \tag{3.5}$$

where $R_i(\nu)$ is the spectral response curve for the waveband i receiver (see Beichman 1988).

By taking the ratio of intensities at two wavebands i and j, and using equation 3.5, one derives

$$\frac{f_i}{f_j} = \frac{\int R_i(\nu)\nu^{\beta} B(\nu, T) d\nu}{\int R_j(\nu)\nu^{\beta} B(\nu, T) d\nu}. \tag{3.6}$$

This value is dependent on T, β and the response curves, of the receivers. Assuming a value of β and using the listed response curves in the IRAS Explanatory Supplement (Beichman et al 1988) one can tabulate f_i/f_j versus T. A function giving T as a function of f_i/f_j can be created by fitting a spline to the tabulated values. For any observations of a cloud at 2 wavelengths one can then estimate the temperature and calculate the critical frequency at which $\tau_{\nu_c} = 1$,

$$\nu_c^{\beta} = \frac{\int R_i(\nu)\nu^{\beta} B(\nu, T) d\nu}{f_i}. \tag{3.7}$$

Using this one can calculate the optical depth of the cloud at another wavelength by using equation 3.3 (for wavelengths over which the grey body spectrum exists).

The IRAS90 routine Coltemp originally deals only with temperatures above 30K (David Berry personal communication). However Wood et al (1994) found that the resulting inferred optical depths for clouds with T less than 30K correlate accurately with optically thin molecular emission and therefore with the true structure of the clouds (see their fig 1b). They further suggested that the reason why the survey traced the real structure so well, even though the clouds are very cool, is because the emission is due to a small fraction of the dust, which is at a consistently higher temperature than the rest of the dust, and constitutes a mass fraction of the ISM $\sim$ 1/2000. I therefore altered Coltemp to allow a range of temperatures from 10 to 10000K to be handled.

This method uses absolute fluxes and as discussed earlier the ISSA images have systematic offsets from the absolute fluxes. However the differential photometry is well constrained. By identifying areas

of 'background' in the images which contain little or no emission from the clouds one can estimate the surface brightness of clouds by taking the difference between the cloud's and the background's intensity. The technique used is described below

3.2.1 Finding a Suitable Background

As discussed above the absolute calibration of the ISSA survey is poorly defined. This is most readily apparent when one realises that several of the ISSA plates have large regions of negative surface brightness. The explanatory supplement to the ISSA (Wheelock et al 1994) explains that this uncertainty in the absolute zero point is dominated at 12 and 25μm by uncertainties in the zodiacal emission model, and at 60 and 100μm by imperfect knowledge of the detector offsets. All bands are affected to some extent by both of these error sources. The 60 and 100μm intensities over the whole sky have been compared to COBE's DIRBE experiment, which surveyed the sky at the same wavelengths but with lower angular resolution (Wheelock et al 1994). It was found that there was both a DC offset (a systematic discrepancy) between the two satellites' calibration and an AC discrepancy (ie a non systematic discrepancy which varied from position to position) in the calibration of the satellites' receivers. Because the DIRBE satellite's photometry was absolutely calibrated (as opposed to differentially) the discrepancy between the two is most likely to be due to errors in the IRAS calibration.

It is well known that there is extended emission throughout the sky at far-infrared wavelengths due to the Galactic cirrus. This has been well studied by Bazell and Desert (1988) and Gautier et al (1992), and the limits this emission puts on faint extra galactic work is well understood. Emission from the cirrus exists in almost every direction, diminishing with galactic latitude. The temperature of the clouds are thought to be approximately 30K, they are not gravitationally bound and probably contain both molecular and atomic material(Turner 1996). Because this emission is very diffuse and widespread, any background area will contain cirrus emission.

In general, astronomical data sets are reduced in a two step process, the images are first flat fielded and then backgrounded. An example of such a procedure for the ISSA plates is presented in Penprase and Helou (1994). The images were flat fielded by assuming that each quadrant contained a suitable background area. Although this is a reasonable assumption to make at high Galactic latitudes it is probable at low Galactic latitude that a plate quadrant can be entirely filled by a cloud complex. It is important that one does not arbitrarily assume that any particular region contains a background. No attempt here is made to flat field, it is assumed that the destriping algorithms produce a suitably flatfielded image over each plate. However the existence of a suitably close background region will put

constraints on which fields can be analysed and will also give an indication of when cloud-cloud confusion becomes significant.

For optical images Beard et al (1990) showed how histograms of pixels intensities contain valuable information about the background. In relatively empty areas the histogram takes the form of a single Gaussian peak and in regions densely populated with real sources several further peaks appear in the histogram at higher intensities. A similar method is used here for the ISSA plates.

I developed an algorithm to identify the large-scale low intensity structure of the ISSA. Pixel histograms of all the ISSA fields were constructed by binning the pixels in each ISSA field into histograms of surface intensity. The histograms contained either all the pixels in the field, or only the lowest 5 or 10MJy/Sr regions of surface brightness if the image showed a large range in surface brightness. Examples of these are given in Figure 3.2. On examination it was found that some field's pixel histograms contained a single peak, some contained double or multiple peaks and some had much more complicated structures. By using the Figaro EMLT routine (which is designed to pick out Gaussian emission lines in astronomical spectra) all the fields were searched to identify whether its histogram had a peak with a width of less than 2MJy/Sr (ie $< 10 \times$ the calibration noise) and at low enough intensity to be consistent with an area of background. Any such peak was taken as evidence of an area of low level emission in the field which can be described as an area of background containing only low level emission. A number of fields were inspected visually to determine which regions contribute to the low intensity peak. It was found that the pixels come from a contiguous discrete area of the sky, and are not randomly isolated pixels.

The position of the peak was recorded and used as a measure of the background surface brightness in the field.

3.2.2 Results: Cirrus Distribution and Cloud Confusion.

272 ISSA fields were identified by this technique at 100μm and 368 at 60μm (from a total of 430 for each wavelength) as containing significant background regions. The average widths of the low intensity peaks in the pixel histograms, were generally at least a factor of two or three larger than the average calibration errors indicating the existence of real cirrus structure within the background regions.

To investigate the overall nature of the background, maps which interpolated from region to region of background were constructed. This was done by first recording the values of the pixel histogram low intensity peaks (in MJy/Sr) and recording the central position of the field in which it was found.

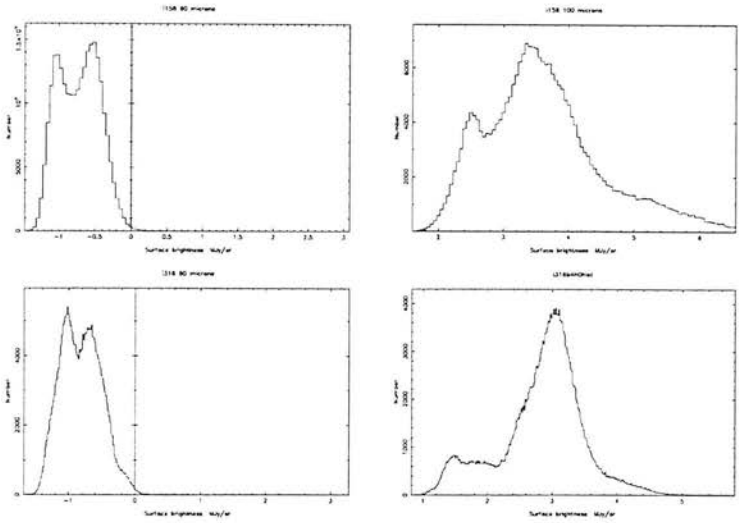

Figure 3.2: Pixel histograms of the 60 & 100μm emission from two representative ISSA fields.

Interpolation on a sphere is not simple. One could for example try to fit a set of normalised independent functions to the values. In all-sky work the obvious set of functions to use is the set of spherical harmonics. However, both the fitting and interpretation of these results would be extremely complicated. Instead a simpler interpolation technique was devised, somewhat akin to box-car averaging. For every square degree on the celestial sphere the distance to the centre of the nearest few ISSA fields containing a region of background was calculated, to allow averaging. This gives a series of angular displacements to the background regions $(\theta_1, \theta_2, \theta_3, \theta_4, ...\theta_n)$ where

$$\cos(\theta_i) = \cos(\mathrm{dec_i})\cos(\mathrm{dec})\cos(\mathrm{ra} - \mathrm{ra_i}) - \sin(\mathrm{dec_i})\sin(\mathrm{dec}). \tag{3.8}$$

Here the right ascension and declination of the position I wished to interpolate to is denoted ra and dec respectively and the position of the background regions is denoted $\mathrm{ra_i}$ and $\mathrm{dec_i}$.

I then attributed to each position the value of surface brightness,

$$\mathrm{I} = \frac{\sum^{\theta_i < \phi} \cos\left(\frac{\pi\theta_i}{\phi}\right) \mathrm{I_i}}{\sum^{\theta_i < \phi} \cos\left(\frac{\pi\theta_i}{\phi}\right)} \tag{3.9}$$

This was chosen because it interpolates between positions smoothly, does not produce discontinuities and weights more heavily the nearest background regions, even given the non uniform spatial sampling of background surface brightness. The result of this process was then projected onto a 2d surface with equal area projection to create a map of background brightness for the whole sky.

Figures 3.3 & 3.4 show maps of the background constructed by my technique at 60 & 100μm respectively. The plots are 'equal area' projections in Galactic coordinates. The intensity varies smoothly, and increases towards the Galactic Plane indicating that the cirrus intensity within background regions increases towards the plane. Both maps contain negative values showing how background subtraction used in producing the ISSA dataset over-compensated in some regions.

In both plots gaps exist in the map near the Galactic Plane because there were very few fields with background which can be used in the interpolation. This gap is larger at 100μm because the foreground clouds are cool and hence emit more strongly and are detected over a wider spatial scale at 100μm than 60μm. The background regions become less apparent as the foreground clouds become more densely distributed, at the same time the cloud overlap becomes more frequent. The gap in the background maps near the Galactic plane indicates background regions can not be easily identified, and confusion due to multiple clouds existing along the same line of sight may be common. This is a region of the sky where individual clouds cannot be easily studied using the ISSA dataset.

By using the method described for defining the background regions in fields, it is found that the background regions become less apparent at low Galactic latitude and the average surface brightness of the cirrus emission increases towards the Galactic plane.

3.3 Zodiacal Contamination

In order to investigate how well the zodiacal emission had been removed plots were constructed showing the background surface brightness plotted as a function of ecliptic latitude. As an example, the 60μm background surface brightness is shown for the first ecliptic quadrant (i.e. all positions with R.A. between 0 and 6h) in Figure 3.5. A slight dependance exists between the background surface brightness and ecliptic latitude possibly due to the zodiacal emission not being completely removed from the ISSA fields.

A number of the ISSA fields were released with the a 'reject' tag. These fields tend to be the fields closest to the ecliptic plane, and have large zodiacal 'bands', several degrees across, passing through them which could not be removed when the ISSA plates were produced. As is discussed later fields contaminated in this way were extremely difficult to analyse and were rejected later on as unsuitable regions for study.

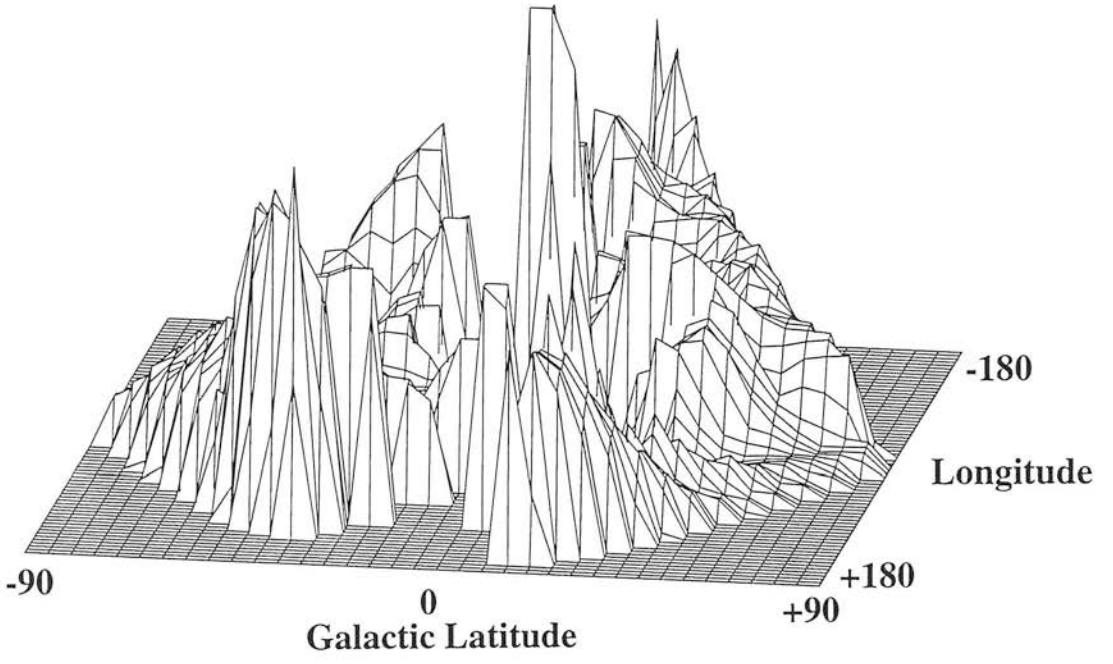

Figure 3.3: Interpolated map of 100μm background regions. Values range from -0.2 to 11 MJy/Sr. There is a gap through the map near the Galactic plane (partly obscured because of the projection), due to a larger number density of clouds near the Galactic plane. This region cannot be easily calibrated and will have frequent overlap of clouds leading to confusion.

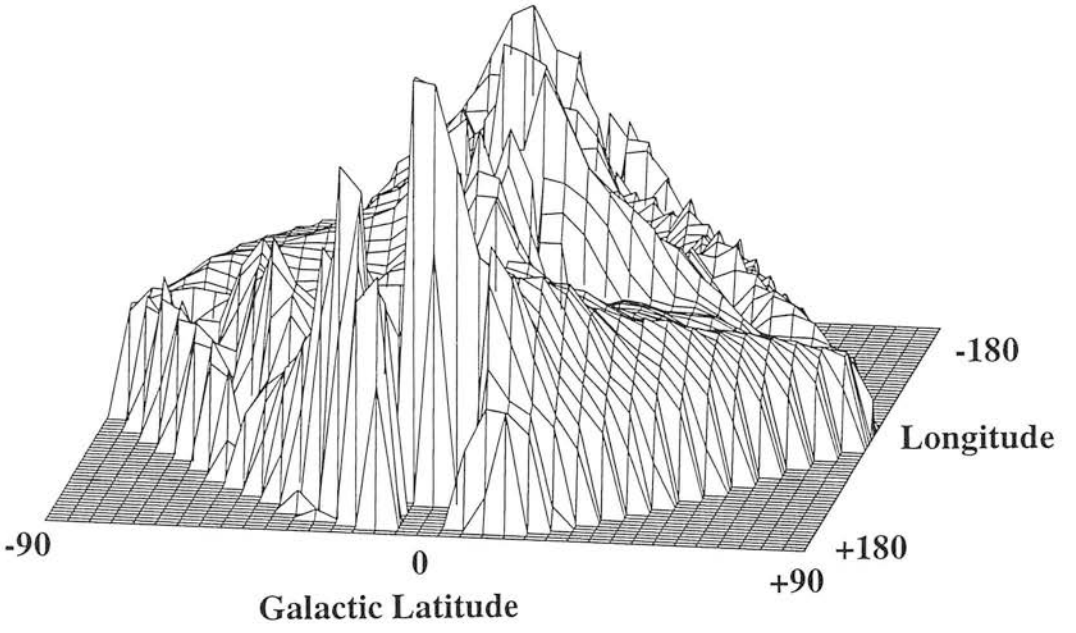

Figure 3.4: Interpolated map of 60μm background regions. Values range from -2.4 to 3.1 MJy/Sr. Because clouds emit less strongly at 60μm than 100μm the gap in the coverage of background surface brightness is smaller at this wavelength.

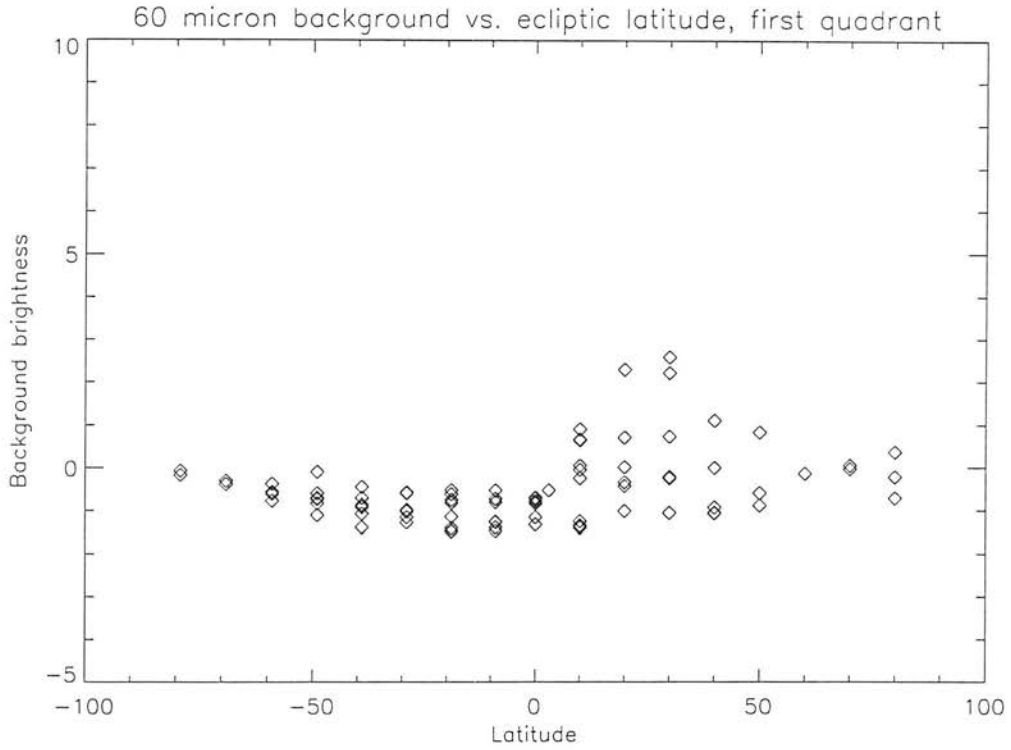

Figure 3.5: Plot of 60μm background surface brightness as a function of ecliptic latitude in the first ecliptic quadrant. A slight correlation seems to indicate that the large scale zodiacal component has not been completely removed.

3.4 Comparing Optical Depth maps with Molecular Observations

Ophiuchus is a well studied region of star formation and extensive ^{13}CO maps of the cloud are available (Loren 1989) which trace the overall structure of the region. L1689 is a distinct complex in this region which contains several previously identified and studied star forming cores. In order to check the COLTEMP method and verify Wood's (1994) results, optical depth and temperature maps for this region were constructed in the following way:

The 100 μm pixel histogram of the ISSA field which contains L1689, was examined and an estimate of the range of intensities within the background region (2σ), and the average intensity (I) of the background was made. A template containing all the pixels with intensity between $I-\sigma$ and $I+\sigma$ within the field at 100μm was constructed and on examination was found to be a discrete area in the field approximately 10 degrees away from L1689. The average values of both the 60 and 100 μm intensities within this template region were calculated in order to measure the background at the two wavelengths. These two values were subtracted from all the pixels in the two respective maps. The standard deviation of the pixel values within the template region was also calculated at each wavelength and the images were thresholded so that only pixels with $I > (3 \times \sigma)$ were used (ie only cloud regions with $I > 3$ times the typical cirrus structure were analysed). This was necessary because at low intensities the inferred temperature is very dependent on the background offset and noise level, and erroneous structures appear in the resulting optical depth maps - the most common being a limb brightening of the low optical depth clouds. Although this type of feature has been interpreted as real limb brightening (ie Langer et al 1989; Wood et al 1992), I discarded these structures.

Temperature and optical depth maps were constructed using the adapted COLTEMP routine. The resulting optical depth map of L1689 is presented alongside the ^{13}CO map (Loren 1989) in Figure 3.6. The ^{13}CO map is only integrated over a small velocity range of the line and a comparison with the overall integrated ^{13}CO emission may give a better comparison to the ISSA optical depth map (because a continuum map has no velocity structure). However it is obvious when comparing the two maps, that the ISSA optical depth map traces similar morphology to the ^{13}CO. In addition it was found when varying the background region used for subtraction that the morphology of the optical depth map is significantly less dependent on the value of background used than the absolute value of inferred optical depth. The well known star forming cores L1689N (also known as R57), and L1689S are clearly visible, as is the isolated core L1689B(also known as R65).

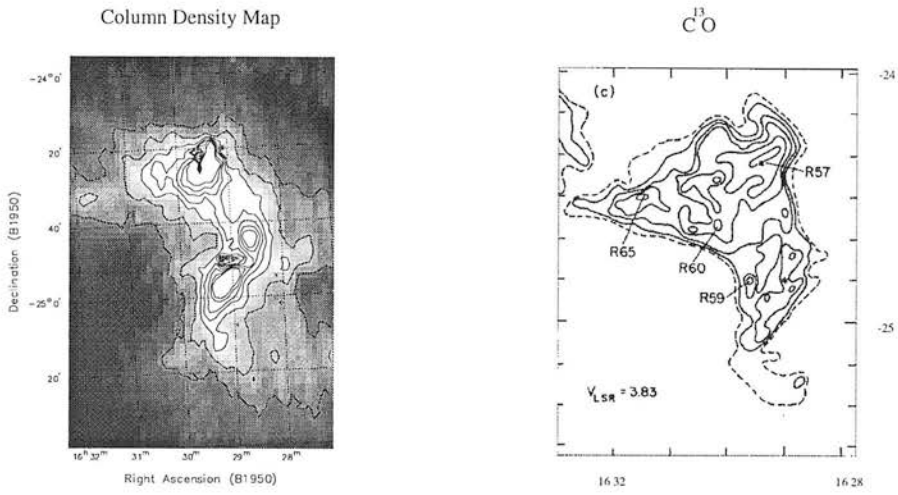

Figure 3.6: Two maps of L1689. The first is a 100 micron optical depth map with contour levels at 0.8,1.1,1.4,1.7,2.0,2.3,2.6 $\times 10^{-3}$. The second image is the ^{13}CO map of the same field taken from Loren (1989), with contours of $T_R^*(^{13}CO)J= (1\rightarrow 0)$ at levels 2,4,6,8,10 and 12K. The ^{13}CO map is centred round the V_{LSR} 3.83km/s. Both maps trace similar structure and pick out the cores L1689N and L1689B (labeled R57, R65 by Loren). L1689S contains a very young stellar object IRAS 16288 (marked with a star in ^{13}CO map) which produces an apparent 'hole' in the optical depth map. This is a phenomenon discussed by Wood et al (1992), and is due to the emission in this region being dominated by small scale structure with a small beam filling factor. It is indicative of very young stellar objects.

At the centre of the cloud there is an apparent 'hole' in the optical depth map which corresponds to IRAS 16288 a young protostar at the centre of L1689S. Wood et al (1992) noted this phenomenon and suggested it was due to a small, relatively bright source dominating the emission in the pixel. Because $\tau(\nu)$ in equation 3.3 incorporates a beam filling factor (ie, the left hand side should more correctly be written $\Omega\tau(\nu)$) a hole is probably indicative of a small bright object dominating the surface brightness. In this case it can be confirmed that it is due to a young protostar. Any similar objects found later on will be investigated.

I conclude, in agreement with Wood et al (1992), that ISSA optical depth maps trace the morphology of star forming clouds and cores.

3.5 A Catalogue of Clouds

In order to get a reasonably unbiased sample of high Galactic latitude clouds, and to study the star formation within these clouds, 96 fields which were identified in the previous section as containing background regions were randomly selected and examined, with the aim of producing colour temperature and optical depth maps. Each was treated in the following way:

The 60 and 100μm maps were each examined and notes were taken about the position of the cloud complexes, existence of zodiacal contamination and quality of the images. The temperature and optical depth maps were then produced in the same way as the map of L1689: First the 100 μm image was examined and a template of the background region was made. The background value for the two wavelengths was then estimated and subtracted from the two images. Optical depth and temperature maps were then constructed. Of the 96 fields chosen 91 were reduced to optical depth and temperature maps. Of these, approximately 60 were examined by eye with the aim of identifying clouds.

In general the resultant optical depth maps contained zero, one, two or three cloud complexes varying in size from a few pixels to half a field. Several fields were discarded either due to having very little structure, being too noisy (usually strongly affected by striping), or having major contamination from zodiacal bands. From the 17 most obvious and opaque clouds were selected for further study. The selection procedure was therefore strongly biased away from regions of low galactic latitude, low ecliptic latitude, and towards high column density clouds. Some of the clouds were found at the edges of the fields and are hence truncated. The clouds selected are listed in Table 3.1.

An extensive search in the literature was made in order to find previously known associations with the clouds. It was found that 3 of the clouds were previously identified by Lynds as dark clouds (Lynds 1962), 2 contained Lynds bright nebulae (Lynds 1965), 7 had been identified by other authors (Taylor et al 1987, Ramesh 1994) and had measured CO velocities and 3 had nearby open cluster associations. Of the 3 open clusters, two have been dated and were found to be old, NGC 7142 is thought to be 4 billion years old, Merlotte 66 is 6 billion years old, implying that they were probably not linked with the cloud in the same way as the Pleiades and Taurus. In addition comparison with the CO Galactic plane surveys (Dame et al 1987) revealed that several clouds were associated with known cloud complexes. Only two had no previously published associations.

Unlike molecular maps and surveys which give the velocity of the clouds and hence give an estimate of the distances, these ISSA selected clouds (like the optically selected clouds of Lynds) do not have easily derivable distances. Distances were estimated either from velocity and spatial association with the Orion,

Cepheus, Chamaeleon and Ophiuchus complexes, or by estimating an upper limit for distance obtained by assuming the clouds lay in the Galactic disc ie. less than 60 pc away from the Galactic plane (Clemens, Sanders and Scoville, 1988). The distance to the clouds associated with complexes was assumed to be within 10 percent of the complex distance.

Clouds found in Cepheus present a particular problem when one attempts to assign a distance. There are two different complexes along the line of sight: one at approximately 300 pc with a velocity $\sim$ 0km/s; and one in the local spiral arm at approximately 800 pc and with a velocity of $\sim$ -12km/s (Grenier et al 1989). Some of the clouds I selected had been sampled with CO observations (by Taylor et al 1987), and the measured velocities revealed the clouds belonged to one or other complex. The sample here contains clouds from both complexes. The three Cepheus clouds in the sample without CO associations could be at either of these two distances.

In total 11 of the 16 clouds had a single distance assigned to them, 2 had upper limits, and 3 could be at either of 2 distances.

Table 3.1 lists the clouds. Column 1 lists the name I assigned derived from the field number. Column 2 gives the approximate position of the centre of the cloud. Column 3 gives the cloud associations: in this column a superscript (1) indicates the association was a dark nebula catalogued by Lynds (1962), a superscript (2) indicates the association is a bright nebulae catalogued by Lynds (1965), a superscript (3) indicates the association is a molecular cloud identified and sampled in CO by Taylor et al (1987), a superscript (4) indicates the association is an open cluster as listed in Lang (1992), the superscript (5) is used once and refers to the star-burst galaxy NGC 1569 (see figure 3.12 for more discussion), and the superscript (6) indicates the association is a molecular cloud identified and sampled in CO by Ramesh (1994). Column 4 gives the velocity of the cloud (if previously measured), and column 5 gives the estimated distance.

The optical depth maps of the clouds are presented in figures 3.6 to 3.22. As can be seen by examining the figures, the clouds do not have optical depths as large as those found in L1689. The peak 100μm optical depths in the complexes seemed to vary from $\sim$0.1-1 $\times 10^{-3}$. The clouds show a large variation in structure, some are very filamentary, some have a single component. None of the clouds show any sort of limb brightening as has been suggested by previous authors. Overlaid on every map are the IRAS Point Sources lying in the fields (each marked as an asterix). It is also clear from the maps that some striping still exists in the images, despite the IPAC data reduction procedures. This striping is largely due to the IRAS satellite having scanned across the sky, and the associated difficulty of receiver calibration. It was not possible for example to take flatfield exposures. The striping often occurs in more than one direction,

Table 3.1: Table of clouds, positions and associations.

Cloud	Position(1950) RA,Dec	Associations	Velocity(LSR)	Distance
422A	1h 35m, 76d 30s	Cepheus		300-800pc
423A	2h 10m, 75d 30m	Cepheus, L133[1], LBN[2] T486[3], T486[4], Berkeley8[4]	3.1-3.5km/s	800± 80pc
002B	2h 30m, -85d 00m	Chamaeleon		200±20pc
423B	3h 00m, 81d 20m	Cepheus		300-800pc
205A	4h 28m, 4d 00m	Orion		450±45pc
411A	4h 15m, 64d 20m	Cepheus, NGC 1569[5]		300-800pc
050A	7h 26m, -48d 00m	R42[6], Merlotte 66[4]	4.8km/s	<250pc
221A	15h 44m, -4d 00m	ρ Ophiuchus, L134N[1]	2.6km/s	125±12pc
021A	0h 00m, -76d 00m	Chamaeleon		200±20pc
420C	20h 40m, 67d 20m	Cepheus, L1148[1], T379[3]	3.5km/s	300±30pc
420B	21h 30m, 66d 00m	Cepheus, L1176[1], T309[3], NGC 7142[4], NGC 7129[4]	-10.8km/s	800±80pc
002A	21h 30m, -83d 00m	Chamaeleon		200±20pc
334A	21h 48m, 35d 30m			<270pc
422C	22h 00m, 77d 30m	Cepheus, LBN T420[3],T428[3],T431[3]	-1.7km/s-5.1km/s	300±30pc
422B	22h 45m 73d 45m	Cepheus, T426[3], T431[3]	-3.7km/s	300±30pc
270A	0h 2m, 13d 50m			<80pc

due to the satellite having scanned the region more than once (generally three times but often more), and each time in different directions.

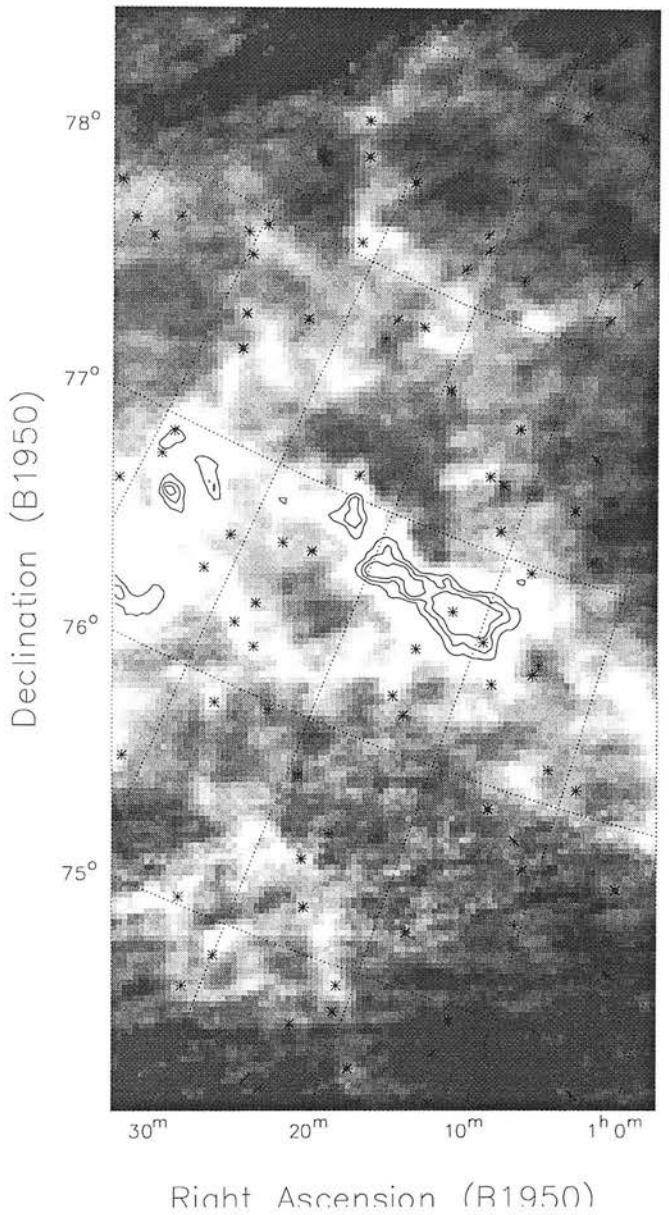

Figure 3.7: 100 μm optical depth map of 422A. Greyscale is from 0.072 to 0.194 $\times 10^{-3}$. Contours are at 0.28, 0.32 and 0.357 $\times 10^{-3}$.

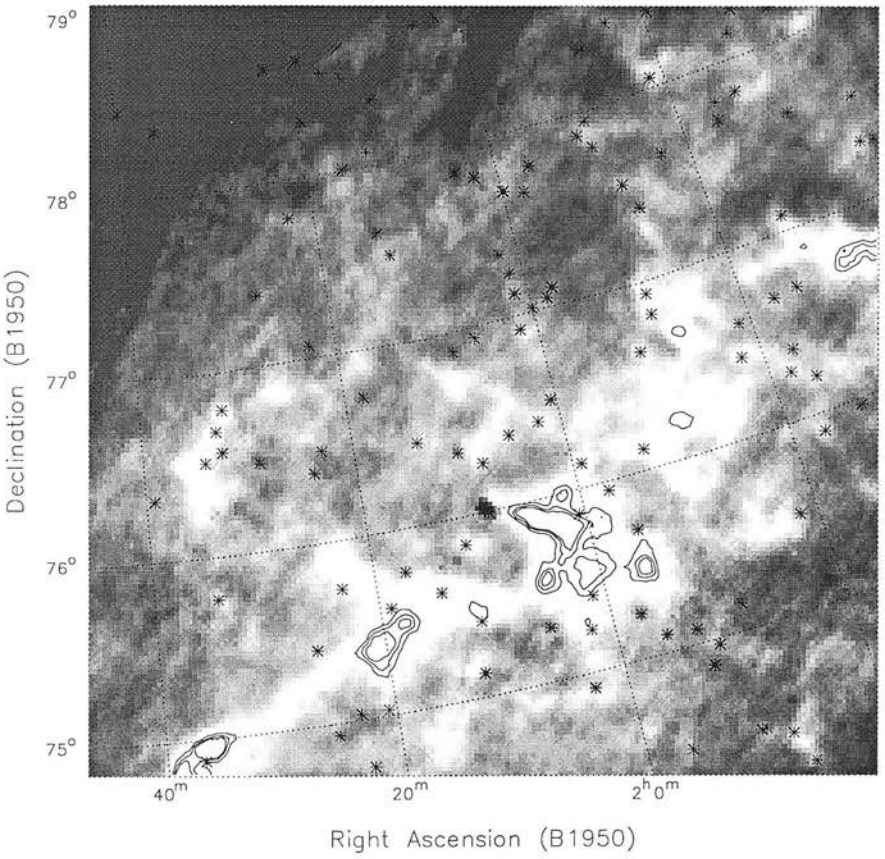

Figure 3.8: 100 μm optical depth map of i423a. Greyscale is from 0.095 to 0.25 $\times 10^{-3}$. Contours are at 0.34, 0.42 and 0.48 $\times 10^{-3}$.

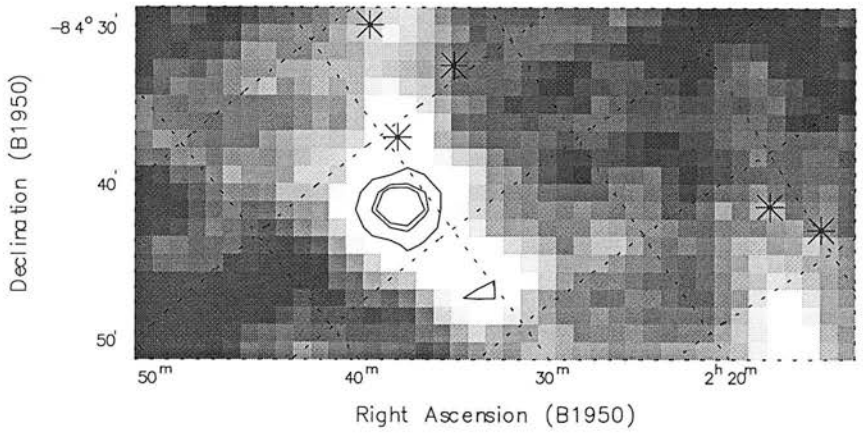

Figure 3.9: 100 μm optical depth map of i002b. Greyscale is from 0.036 to 0.074 $\times 10^{-3}$. Contours are at 0.095, 0.116 and 0.12 $\times 10^{-3}$.

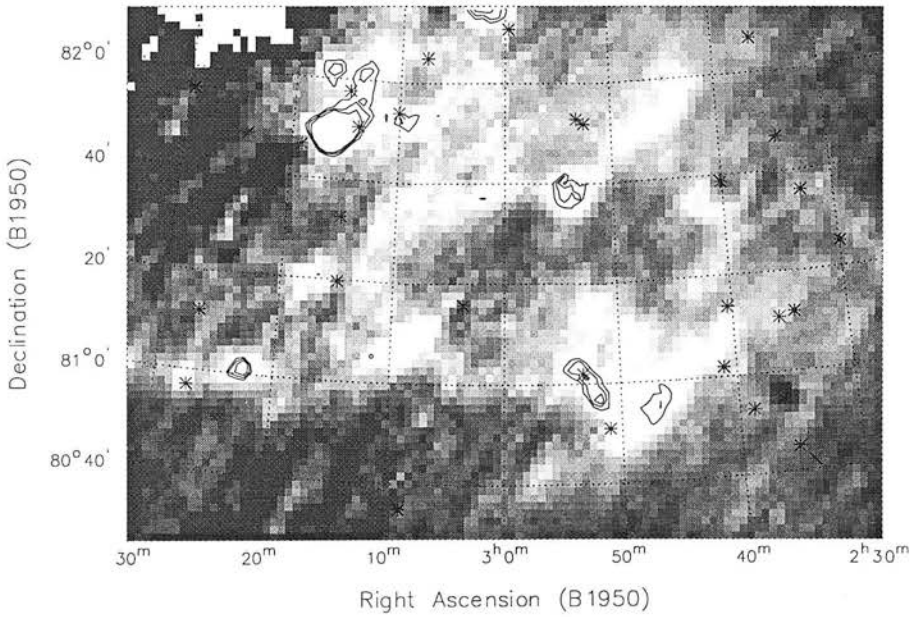

Figure 3.10: 100 μm optical depth map of i423b. Greyscale is from 0.0565 to 0.136. Contours are at 0.16, 0.175 and 0.19 $\times 10^{-3}$.

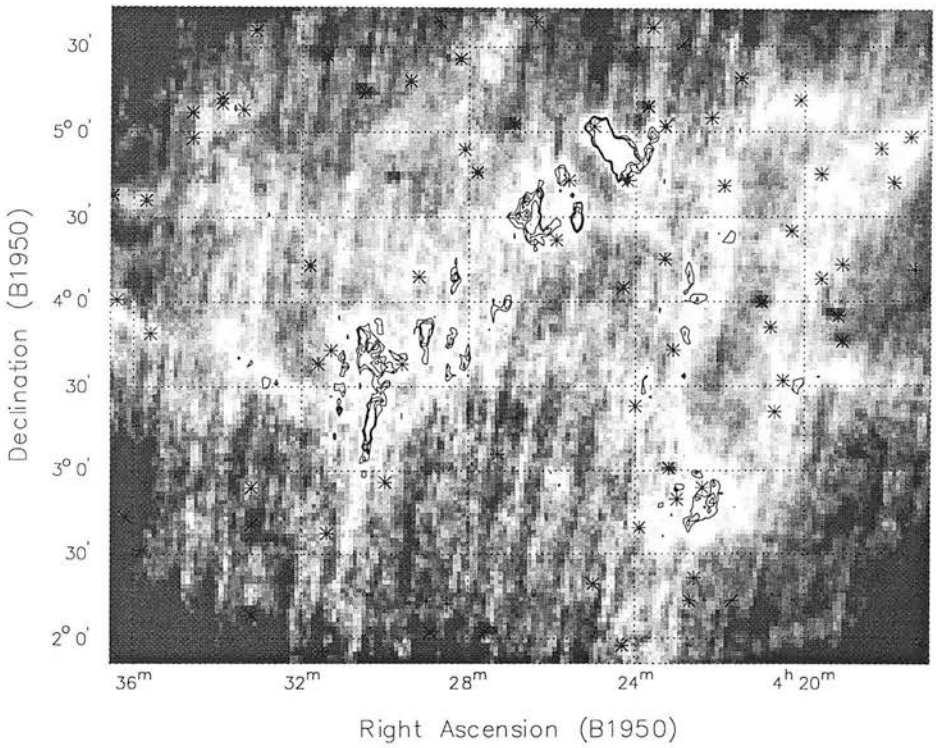

Figure 3.11: 100 μm optical depth map of i205a. Greyscale is from 0.064 to 0.105 $\times 10^{-3}$. Contours are at 0.115, 0.119 and 0.123 $\times 10^{-3}$.

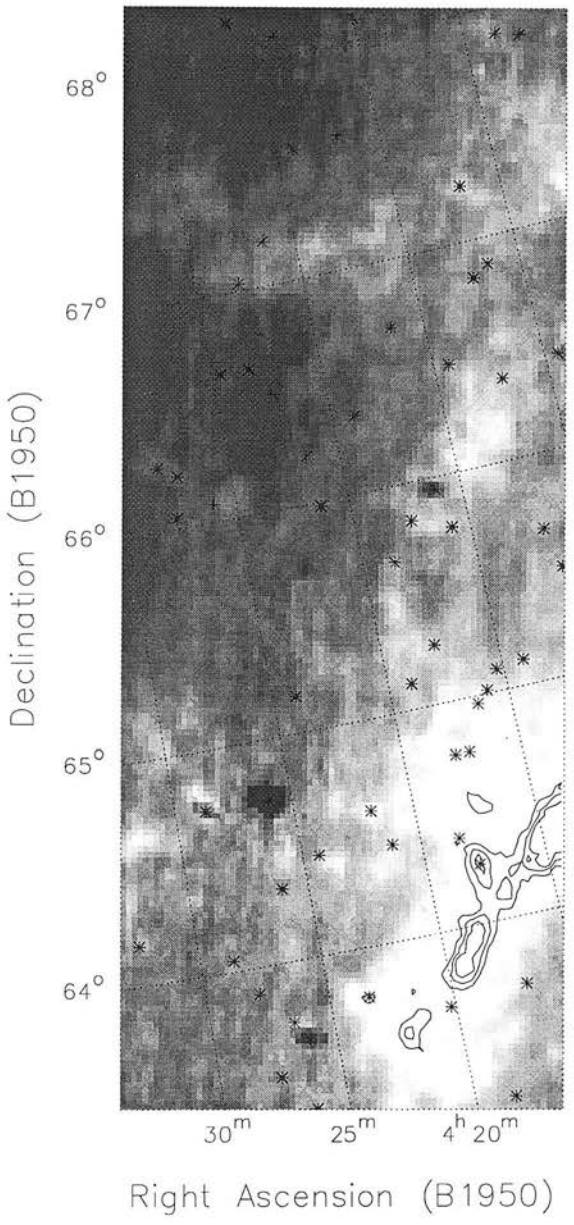

Figure 3.12: 100 μm optical depth map of i411a. Greyscale is from 0.074 to 0.25 $\times 10^{-3}$. Contours are at 0.32, 0.34 and 0.36 $\times 10^{-3}$. In this field two star bust galaxies correspond to the two 'holes' in the image at declination 4h 26m. The larger is the star burst galaxy NGC 1569.

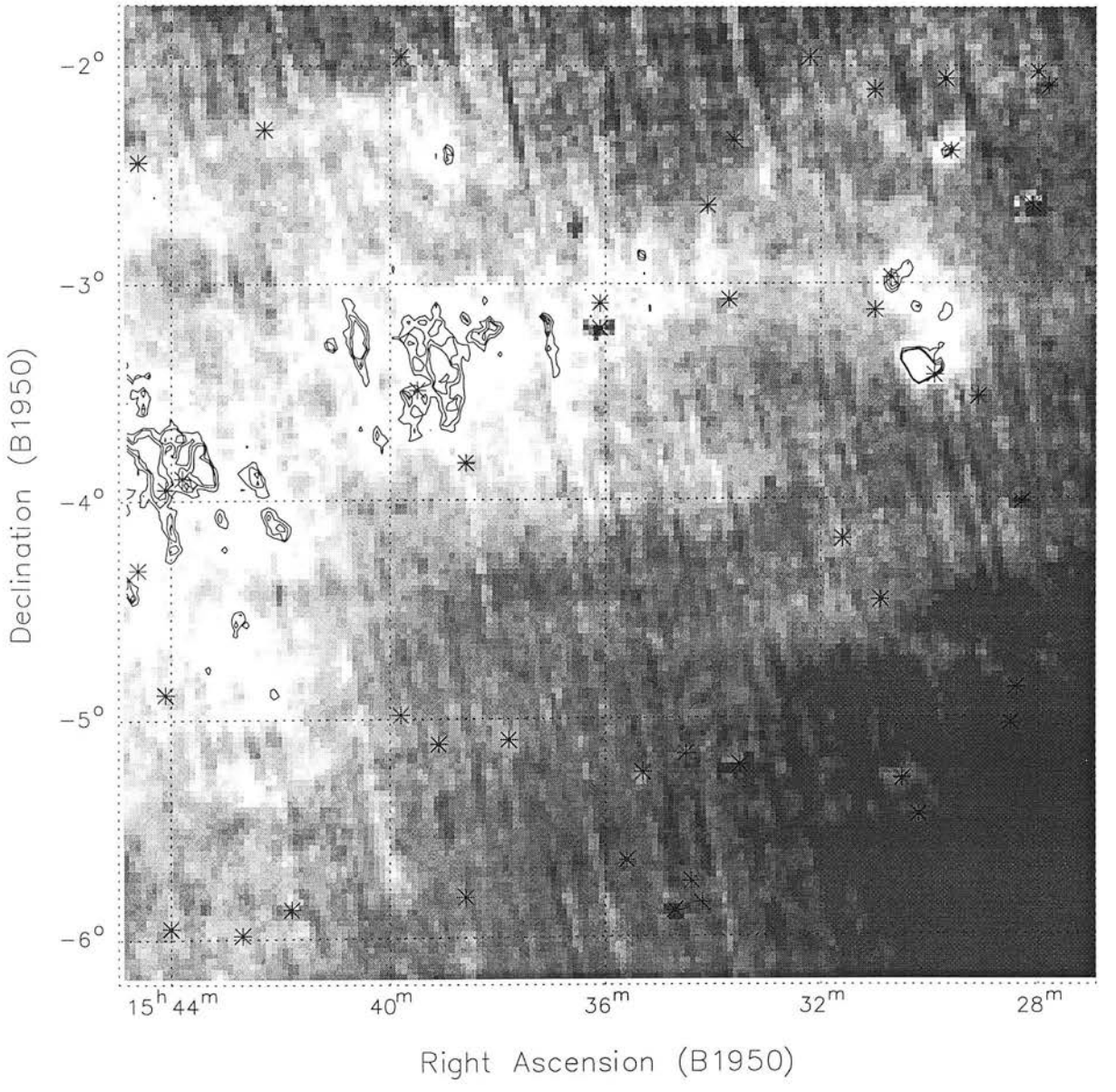

Figure 3.13: 100 μm optical depth map of i221a. Greyscale is from 0.027 to 0.057 $\times 10^{-3}$. Contours are at 0.066, 0.069 and 0.072 $\times 10^{-3}$.

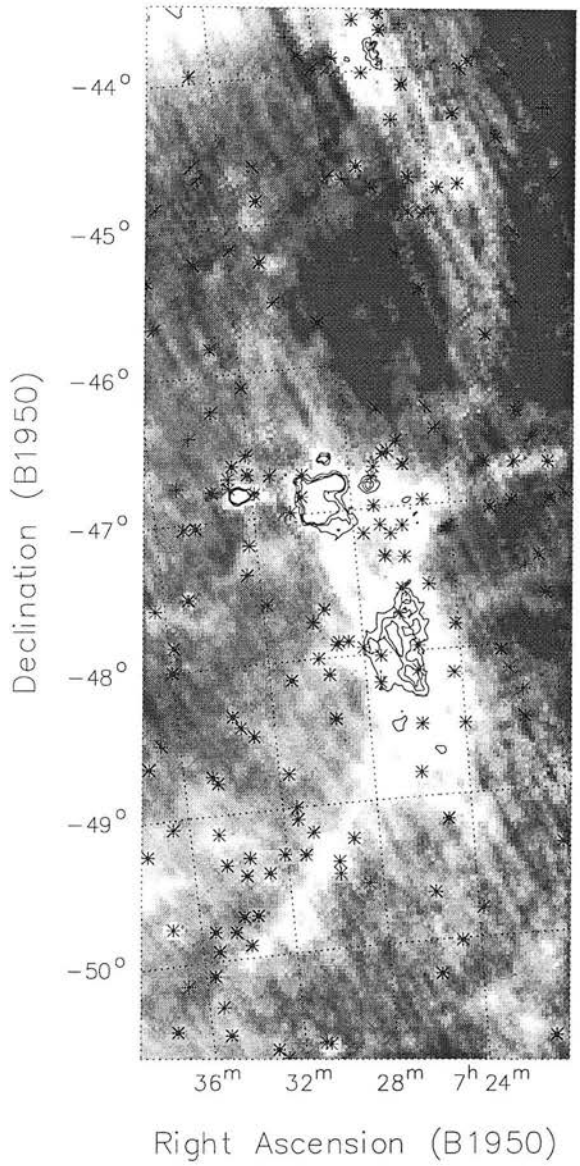

Figure 3.14: 100 μm optical depth map of i050a. Greyscale is from 0.066 to 0.117 $\times 10^{-3}$. Contours are at 0.148, 0.1625 and 0.1750 $\times 10^{-3}$

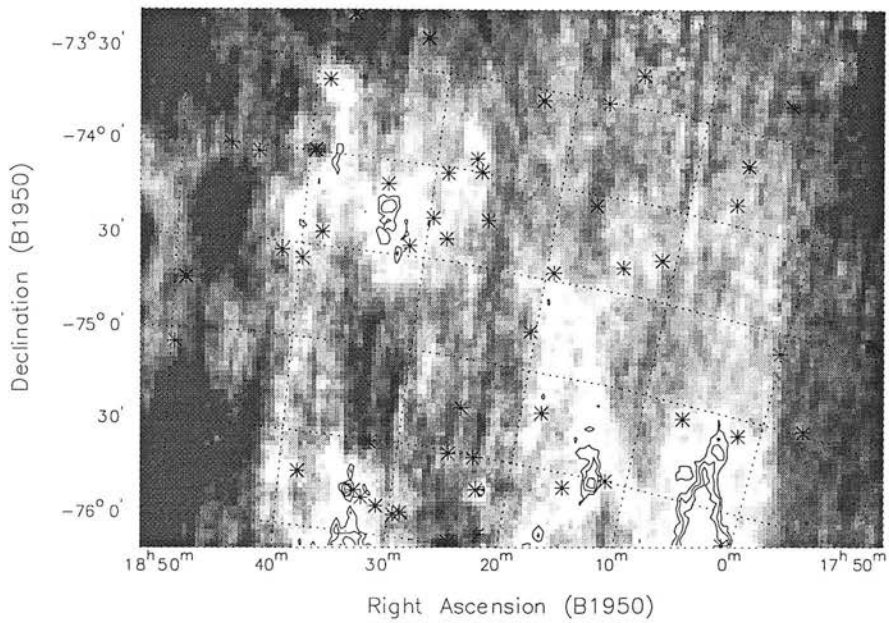

Figure 3.15: 100 μm optical depth map of i021a. Greyscale is from 0.019 to 0.0450. Contours are at 0.054, 0.0575 and 0.061 $\times 10^{-3}$.

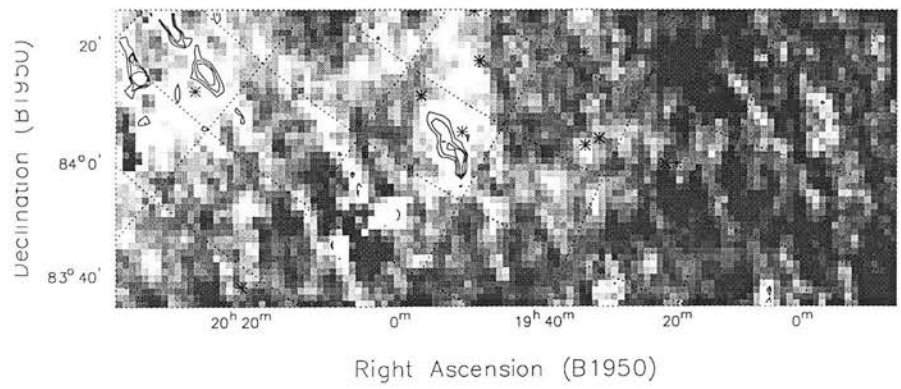

Figure 3.16: 100 μm optical depth map of i428a. Greyscale is from 0.045 to 0.085 $\times 10^{-3}$. Contours are at 0.13, 0.1465 and 0.16 $\times 10^{-3}$.

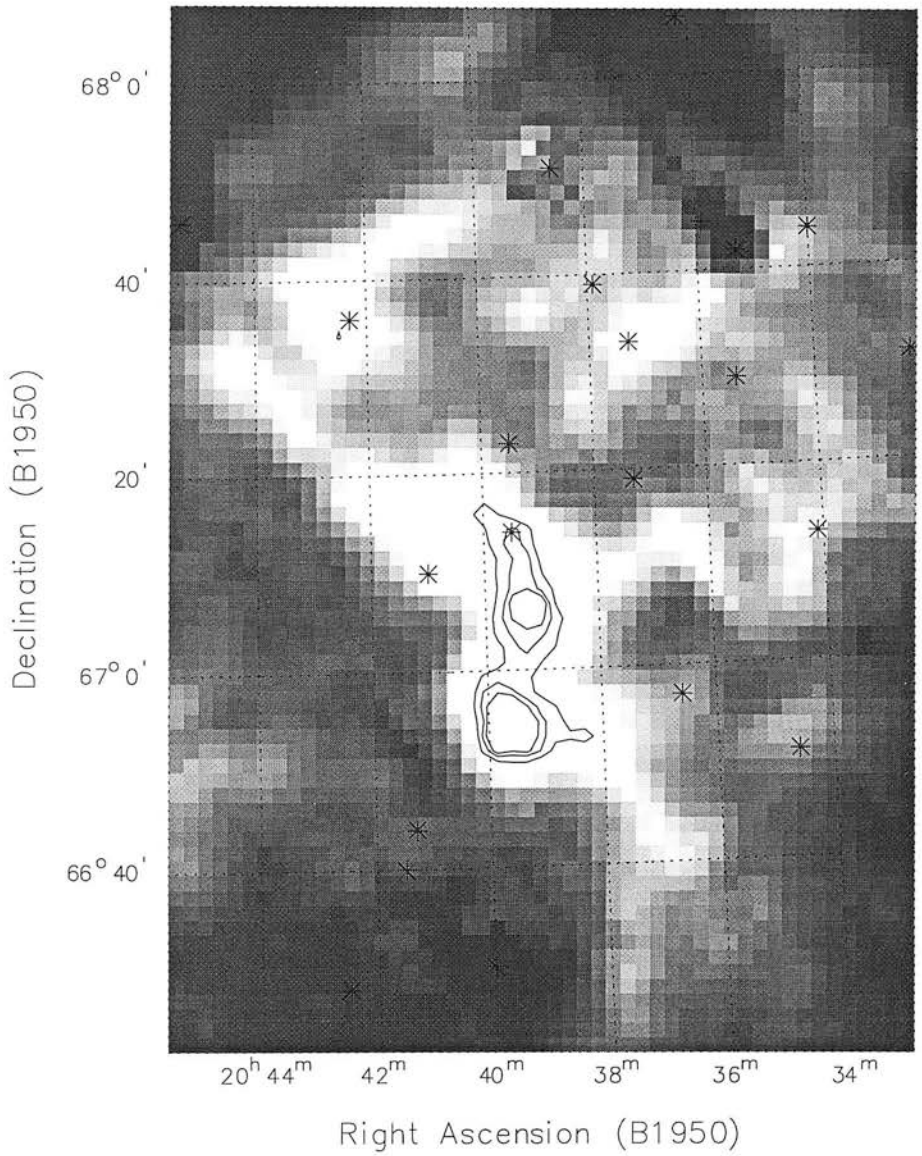

Figure 3.17: 100 μm optical depth map of i420c. Greyscale is from 0.075 to 0.3 $\times 10^{-3}$. Contours are at 0.5, 0.55 and 0.62$\times 10^{-3}$.

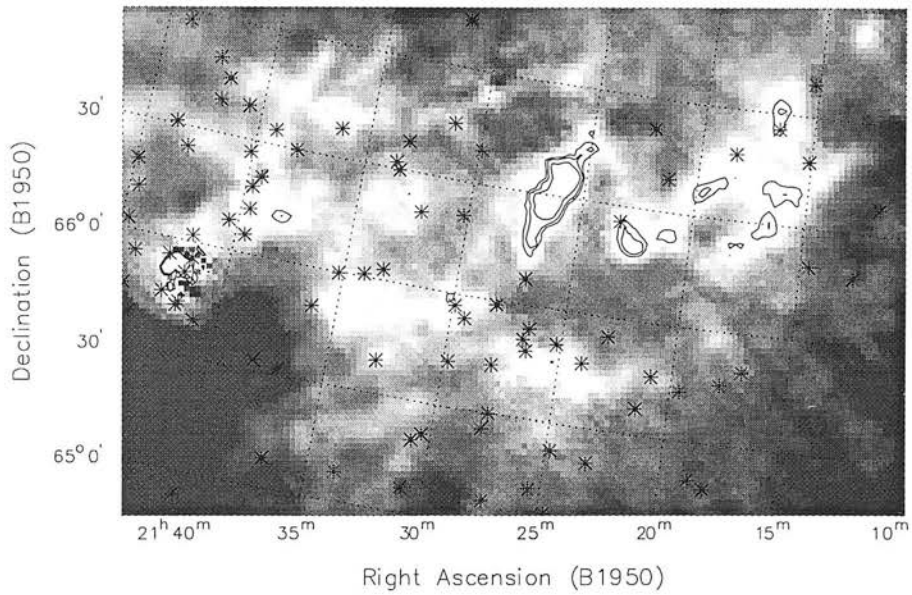

Figure 3.18: 100 μm optical depth map of i420b. Greyscale is from 0.16 to 0.29×10^{-3}. Contours are at 0.338, 0.358 and 0.397 $\times 10^{-3}$.

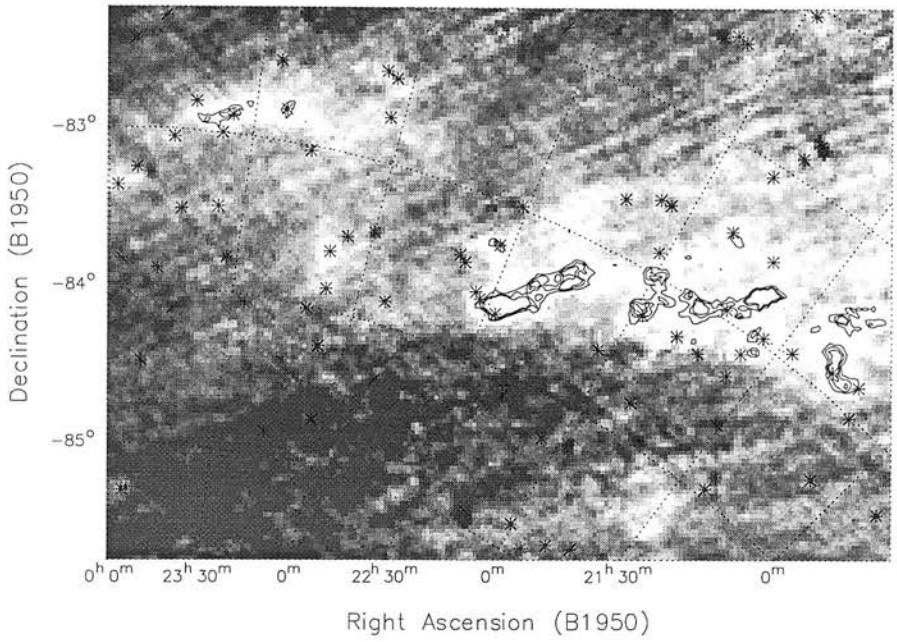

Figure 3.19: 100 μm optical depth map of i002a. Greyscale is from 0.058 to 0.112 $\times 10^{-3}$. Contours are at 0.138, 0.147 and 0.153×10^{-3}.

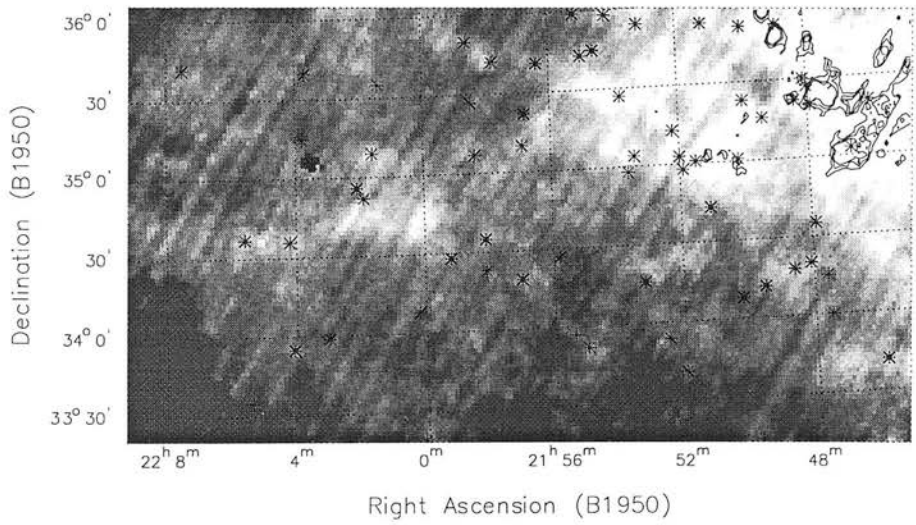

Figure 3.20: 100 μm optical depth map of i334a. Greyscale is from 0.018 to 0.045×10^{-3}. Contours are at 0.054, 0.0565 and 0.0590×10^{-3}.

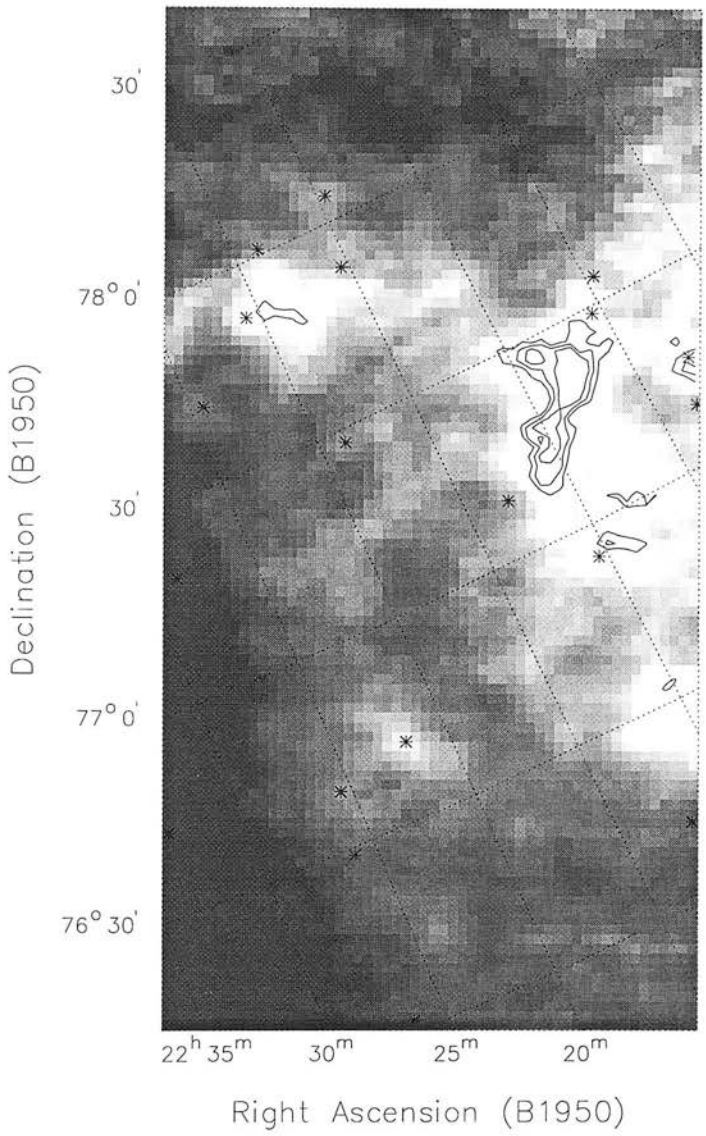

Figure 3.21: 100 μm optical depth map of i422c. Greyscale is from 0.05 to 0.2×10^{-3}. Contours are at 0.25, 0.27 and 0.29×10^{-3}.

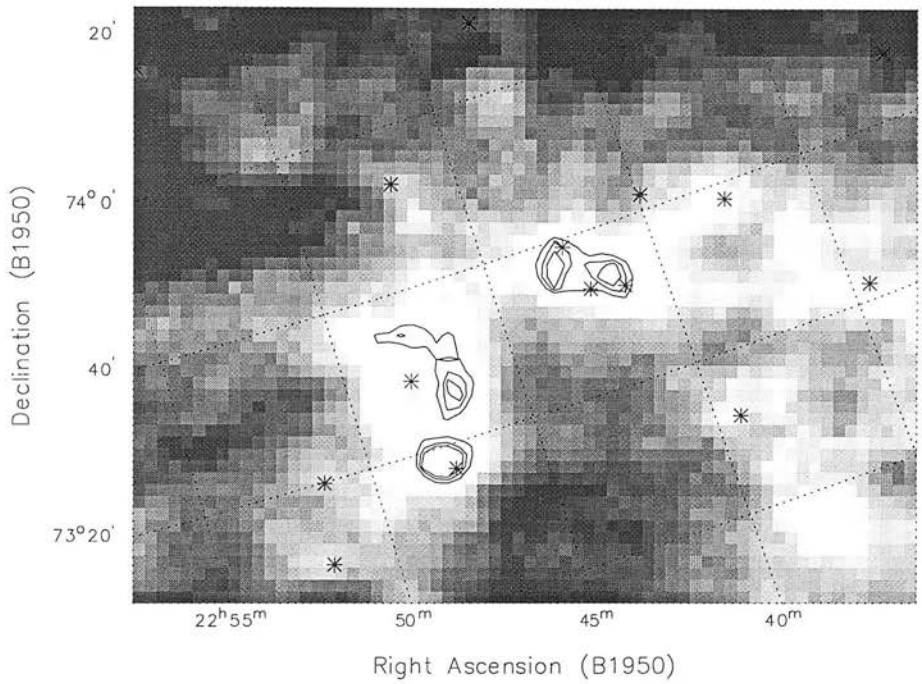

Figure 3.22: 100 μm optical depth map of i422b. Greyscale is from 0.1 to 0.16×10^{-3}. Contours are at 0.189, 0.196 and 0.2×10^{-3}.

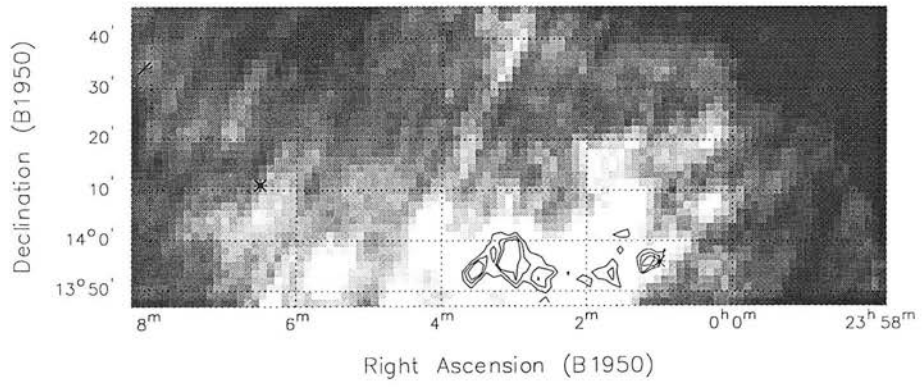

Figure 3.23: 100 μm optical depth map of i270a. Greyscale is from 0.0015×10^{-3} to 0.01×10^{-3}. Contours are at 0.0135, 0.0145 and 0.0155×10^{-3}.

3.6 A Catalogue of Cores, and Core Properties.

A catalogue of the most opaque regions in each cloud was made. The maps were examined by eye, and cores were defined as the regions with optical depth above either 98, 99 or 99.5 percent of the pixels in the rest of the field. In general the level was chosen to ensure that the area defined as a core was reasonably small. Hence for clouds with only one peak in optical depth the higher cut off was used, for clouds with 3 or 4 separate peaks the lower cut off level was used. This ensured that each core was defined as approximately 0.5 percent of the overall cloud size. Hence the effective definition of a core is the most opaque 0.5 percent of a cloud. The temperature, ellipticity, and position of each core was then recorded, and the mass of the cores was also estimated.

The optical depth at 100μm due to dust along the line of sight is expressible (Hildebrand 1983, Woods et al 1992) as

$$\tau_{100} = \pi\langle a\rangle^2 Q_{100} N_g \tag{3.10}$$

where N_g is the column density of grains, $\langle a\rangle$ is the average radius of the grains and Q_{100} is the emission efficiency of the dust grains at 100μm. The mass column density of the grains (in gcm^{-2}) is then given by,

$$\sigma_d = \frac{4}{3}\left(\frac{a\rho}{Q_{100}}\right)\tau_{100} \tag{3.11}$$

where ρ is the grain density. The total mass of the dust (in grams) in the core (with projected area A) is therefore given by

$$M_{dust} = A\langle\sigma_d\rangle. \tag{3.12}$$

Normally the dust to gas ratio in the ISM is assumed to be approximately 1:100 by mass (consistent with the value presented by Hildebrand 1983). However it is well known that when this ratio is used for IRAS 100 micron optical depth images it underestimates the total mass of gas by a substantial amount. The reason for this is uncertain, but sometimes is attributed to preferential heating of the dust within selected regions of a cloud by UV radiation (eg Clemens et al 1991) or due to a separate population of dust existing, possibly PAHs or small graphite grains, with a higher equilibrium temperature than the majority of the dust in the ISM (eg Wood et al 1992). In either situation a small fraction of the total dust in the ISM dominates the emission at IRAS wavelengths.

By using two relations, firstly that $A_v \sim 2 \times 10^4 \tau_{100}$ and secondly that $N_{H_2}(cm^{-2}) \sim 10^{21} A_V$, Wood et al (1992) argue that only one 50th of the total dust is detected at IRAS wavelengths, and use a IRAS dust to gas ratio of 1:2000 in their analysis. For consistency this value is also used here - although it should be noted that this value is likely to change from cloud to cloud due to differences

in physical conditions. Processes like ambipolar diffusion, aggregation, and optical processing could all vary the ratio. With a value for $(a\rho/Q_{100}) \sim 32 gcm^{-2}$ derived using Hildebrand's (1983) relationship $a\rho/Q_\lambda = 3.2 \times (1000/\lambda(\mu m))$ for a mixture of graphite and silicon grains, then one obtains the equation

$$M(M_\odot) \sim 1.25 \times 10^{-2} \times D^2(pc) \sum_{pixels} \tau_{100} \tag{3.13}$$

where D is the distance to the core. The core masses were estimated using equation 3.13. It should be stressed that the uncertainty in derived mass is almost certainly dominated by our lack of knowledge about what fraction of the the dust in the ISM contributes to the IRAS emission, the dust composition (both of these will almost certainly vary from cloud to cloud), and the uncertainties in the distances of the cores. However the mass of L1689, derived from equation 3.13 (assuming the distance to Ophiuchus is 160 pc) and the optical depth map presented in Figure 3.6, is $448 M_\odot$ which is similar to the value derived by Loren (1989) of $566 M_\odot$ from the ^{13}CO map. In addition Wood et al (1994) find that the assumptions outline here also predict the mass of L1457.

The list of cores are tabulated in Table 3.2 along with their properties. Column 1 lists the RA ordered number, column 2 lists the cloud in which it was found and column 3 lists the position of the centre of the core. Column 4 lists the derived temperature of the core, column 5 lists the solid angle of the core in square arcminutes (as measured by the Starlink PISAFind routine), column 6 lists the mean optical depth of the core, column 7 lists the peak optical depth of the core, column 8 measures the ellipticity of the core, column 9 lists its average radius, column 10 lists the position angle of the core major axis. Column 11 lists the derived mass of the core and column 12 lists the derived Jeans mass (see equation 2.37).

In addition, if the core contained an IRAS point source association this source is listed along with the measured flux of the source, the superscripts on the name indicates the catalogue from which the associated source is taken. A superscript (1) indicates the source appears in Smithsonian Astrophysical Observatory Star Catalogue, a superscript (2) indicates the source appears in the catalogue of Ohio State University Radio Sources, a superscript (3) indicates the source appears in the IRAS Serendipitous Survey Catalogue, a superscript (4) indicates that the source appears in the Dearborn Observatory Catalog of Faint Red Stars, and a superscript (5) indicates the source appears in the IRAS Small Scale Structure Catalog (for references see Table H.1 in Beichman 1988.)

In short a selection of 60 cloud cores drawn from relatively high Galactic latitude clouds is presented, with estimates of size, mass, column density and point source associations.

Table 3.2: Table of cloud cores, positions, IRAS point source associations and masses.

No.	Field	Position(1950) RA,Dec	Temp.	Size	$\overline{\tau}$	τ_{max}	Ellipt.	r	θ	Mass	M_J
			K	min^2	$(\times 10^{-3})$	$(\times 10^{-3})$		pc	°E of N	$M_\odot$	$M_\odot$
		IRAS(other names)	12μm	25μm	60μm	100 μm					
			Jy	Jy	Jy	Jy					
1	270A	0h 3m 3s, 13d 56m 30s	29.2	23.4	0.016	0.018	0.43	<0.22	11	2.2±0.4	<64
2	422A	1h 21m 38s, 76d 41m 37s	21.7	104.7	0.40	0.439	0.43	0.5-1.2	67	300-2130	20-32
		01226+7641	< 0.58	< 0.25	< 0.40	2.50					
3	422A	1h 27m 54s, 76d 44m 27s	21.5	45.3	0.38	0.404	0.71	0.34-0.85	68	124-880	<16-26
4	423A	2h 3m 18s, 75d 51m 50s	20.8	54.7	0.52	0.580	0.68	0.38	71	200±40	64
5	423A	2h 20m 46s, 75d 22m 54s	21.4	12.5	0.49	0.505	0.18	0.18	134	44±9	45
6	002B	2h 31m 55s, -84d 56m 3s	23.8	21.9	0.12	0.142	0.01	0.16	123	8.3±1.6	20
7	423A	2h 36m 20s, 74d 57m 3s	20.2	26.6	0.55	0.651	0.41	0.26	116	105±20	52
		02368+7453	0.44	0.89	0.89	3.21					
8	423B	2h 52m 42s, 81d 0m 20s	22.0	17.2	0.19	0.206	0.69	0.21-0.52	35	23.1-164	18-30
		02532+8102	<0.25	< 0.64	< 0.40	3.57					
9	423B	3h 15m 55s, 81d 50m 15s	19.8	54.7	0.24	0.4112	0.36	0.38-0.95	120	97-689	21-35
		03139+8151	0.33	<0.25	< 0.40	<4.99					
		03191+8147(545K0)[1]	0.29	< 0.25	<0.40	< 5.23					
10	411A	4h 14m 59s, 64d 19m 2s	23.0	92.2	0.37	0.403	0.55	0.49-1.21	167	245-1745	20-32
11	411A	4h 17m 1s, 64d 7m 9s	23.3	12.5	0.34	0.352	0.32	0.18-0.45	169	31-221	12-20
12	411A	4h 17m 45s, 64d 14m 51s	23.1	29.7	0.35	0.369	0.55	0.28-0.7	22	75-534	15-25
		04178+6416(13118M0[1])	0.67	<0.25	<0.40	<8.18					
13	411A	4h 18m 55s, 63d 53m 58s	22.6	79.7	0.36	0.380	0.66	0.45-1.12	161	206-1464	19-32

Table 3.2: Table of cloud cores, positions, IRAS point source associations and masses (continued).

No.	Field	Position(1950) RA,Dec	Temp.	Size	$\overline{\tau}$	τ_{max}	Ellipt.	r	θ	Mass	M_J
			K	min^2	$(\times 10^{-3})$	$(\times 10^{-3})$		pc	°E of N	$M_\odot$	$M_\odot$
		IRAS(other names)	12μm	25μm	60μm	100 μm					
			Jy	Jy	Jy	Jy					
14	205A	4h 24m 32s, 4d 54m 24s	24.1	136	0.13	0.154	0.58	0.89	38	290±60	44
		04250+0502	<0.29	< 0.26	<0.40	2.37					
15	205A	4h 25m 23s, 4d 30m 14s	24.6	21.9	0.12	0.132	0.57	0.35	173	44±9	29
16	205A	4h 26m 26s, 4d 30m 28s	24.4	57.8	0.12	0.139	0.51	0.58	3	120±20	37
17	205A	4h 29m 2s, 3d 48m 54s	24.1	21.9	0.13	0.130	0.52	0.35	168	44±9	29
18	205A	4h 30m 18s, 3d 37m 46s	24.2	26.6	0.12	0.128	0.51	0.39	71	53±20	31
19	205A	4h 30m 21s, 3d 18m 12s	22.6	31.3	0.13	0.137	0.79	0.43	168	65±13	28
20	205A	4h 30m 32s, 3d 46m 53s	24.3	18.8	0.12	0.130	0.51	0.32	178	38±8	28
21	050A	7h 26m 5s, -48d 10m 15s	26.3	20.3	0.18	0.188	0.55	<0.63	39	<203	<32
22	050A	7h 26m 39s, -47d 54m 27s	26.0	34.4	0.18	0.192	0.74	<0.82	20	<344	<37
23	050A	7h 29m 16s, -46d 54m 22s	25.9	170.3	0.20	0.278	0.28	<1.85	148	<1905	<50
		07299-4644(MSH 07408[2])	<0.25	<0.25	1.05*	10.34					
		07300-4653	0.25	<0.25	<1.37	<10.53					
		07305-4659(07305_4659[3])	<0.41	<0.25	0.99	<10.25					
24	050A	7h 32m 30s, -46d 50m 12s	25.5	26.6	0.20	0.240	0.30	< 0.72	97	<299	<33
25	221A	15h 30m 12s, -3d 23m 34s	25.0	40.6	0.085	0.101	0.31	1.35	50	4.3±0.8	22
26	221A	15h 39m 3s, -3d 24m 15s	25.1	43.8	0.074	0.0786	0.46	0.14	19	4.0±0.8	24
		15395-0330	<0.33	<0.85	< 0.40	1.02					
27	221A	15h 40m 36s, -3d 16m 5s	25.0	18.8	0.075	0.077	0.70	0.092	4	1.8±0.4	19

Table 3.2: Table of cloud cores, positions, IRAS point source associations and masses (continued).

No.	Field	Position(1950) RA,Dec	Temp.	Size	$\overline{\tau}$	τ_{max}	Ellipt.	r	θ	Mass	M_J
			K	min^2	$(\times 10^{-3})$	$(\times 10^{-3})$		pc	°E of N	$M_\odot$	$M_\odot$
		IRAS(other names)	12μm	25μm	60μm	100 μm					
			Jy	Jy	Jy	Jy					
28	221A	15h 43m 25s, -3d 50m 38s	25.4	28.1	0.076	0.081	0.60	0.11	14	2.6±0.5	21
29	221A	15h 44m 21s, -3d 49m 22s	5.6	50.0	0.076	0.086	0.69	0.15	19	4.8±1.0	24
30	021A	18h 3m 10s, -75d 28m 48s	25.6	259.4	0.061	0.070	0.60	0.55	169	50±10	52
31	021A	18h 13m 5s, -75d 28m 21s	25.9	46.9	0.058	0.063	0.63	0.23	174	8.7±1.7	34
32	021A	18h 33m 20s, -76d 0m 14s	25.6	46.9	0.058	0.063	0.11	0.23	141	8.7±1.7	34
33	021A	18h 33m 22s, -74d 16m 4s	25.5	37.5	0.057	0.061	0.36	0.21	11	6.8±1.4	33
34	021A	18h 33m 48s, -75d 45m 39s	25.5	20.3	0.058	0.063	0.61	0.15	173	3.8±0.8	27
		18333-7547	<1.33	<0.34	<0.40	1.47					
35	021A	18h 37m 53s, -74d 0m 43s	25.0	12.5	0.055	0.056	0.66	0.12	157	2.2±0.4	25
36	420C	20h 39m 20s, 67d 7m 58s	19.1	40.6	0.60	0.680	0.62	0.32	175	160±30	13
37	420C	20h 39m 37s, 66d 54m 51s	19.0	35.9	0.64	0.761	0.25	0.31	39	166±30	11
38	420B	21h 16m 11s, 66d 39m 3s	23.6	29.7	0.35	0.359	0.44	0.35	74	530±110	25
39	420B	21h 16m 42s, 66d 29m 40s	23.9	20.3	0.35	0.359	0.20	0.62	130	36±70	23
40	420B	21h 16m 43s, 66d 59m 26s	23.25	25.0	0.35	0.369	0.59	0.67	172	445±90	23
41	002A	21h 18m 29s, -82d 49m 34s	22.7	59.4	0.15	0.164	0.66	0.26	16	29±6	22
		21185-8252	<0.25	<0.25	<0.40	2.49					
42	420B	21h 19m 34s, 66d 37m 23s	23.3	18.8	0.35	0.371	0.62	0.58	120	340±70	22
43	420B	21h 22m 38s, 66d 21m 22s	24.5	37.5	0.36	0.393	0.38	0.84	34	690±140	26
		21232+6626	<2.12	<0.25	<0.55	9.58					

Table 3.2: Table of cloud cores, positions, IRAS point source associations and masses (continued).

No.	Field	Position(1950) RA,Dec	Temp.	Size	$\overline{\tau}$	τ_{max}	Ellipt.	r	θ	Mass	M_J
			K	min^2	$(\times 10^{-3})$	$(\times 10^{-3})$		pc	°E of N	$M_\odot$	$M_\odot$
		IRAS(other names)	12μm	25μm	60μm	100 μm					
			Jy	Jy	Jy	Jy					
44	420A	21h 26m 21s, 66d 30m 46s	24.0	176.6	0.39	0.514	0.65	1.8	149	3600±700	37
45	002A	21h 38m 55s, -82d 45m 12s	22.4	54.7	0.16	0.186	0.47	0.25	100	28±6	22
46	420B	21h 42m 6s, 65d 53m 12s	43.6	34.4	0.50	1.03	0.34	0.79	62	880±180	22
		21426+6556	<0.39	<0.27	2.15	<21.19					
47	334A	21h 46m 35s, 35d 20m 1s	27.5	15.6	0.06	0.063	0.39	<0.60	145	<60	<54
48	334A	21h 46m 51s, 35d 0m 58s	27.2	48.4	0.064	0.071	0.22	<1.0 118	<197	<70	
49	002A	21h 47m 0s, -83d 0m 13s	22.5	42.2	0.154	0.172	0.62	0.22 95	21±4	20	
50	334A	21h 47m 31s, 35d 23m 19s	27.3	50.0	0.064	0.065	0.37	1.1	75	200±40	71
		21479+3520(DO 20925[4])	1.75	0.51	<0.40	<1.82					
		21484+3522	<0.25	<0.25	<0.52	2.87					
51	334A	21h 48m 55s, 35d 46m 40s	27.5	15.6	0.063	0.067	0.35	0.59	153	<63	<52
52	002a	21h 58m 57s, -83d 14m 17s	23.0	28.1	0.15	0.160	0.23	0.18	83	14±3	19
		21580-8316	<0.73	<0.85	<0.40	1.78					
53	002A	21h 59m 28s, -83d 0m 2s	22.4	21.9	0.15	0.156	0.41	0.16	72	11±2	18
54	422C	22h 7m 50s, 77d 22m 11s	21.4	25.0	0.30	0.320	0.48	0.25	180	55±11	16
55	422C	22h 9m 58s, 77d 15m 3s	21.8	12.5	0.30	0.321	0.61	0.18	170	27±5	22
56	002A	22h 15m 50s, -83d 16m 45s	23.2	54.7	0.15	0.170	0.48	0.25	125	27±5	17
57	002A	22h 21m 53s, -83d 23m 50s	23.5	21.9	0.15	0.163	0.57	0.16	128	11±2	24

Table 3.2: Table of cloud cores, positions, IRAS point source associations and masses (continued).

No.	Field	Position(1950) RA,Dec	Temp.	Size	$\overline{\tau}$	τ_{max}	Ellipt.	r	θ	Mass	M_J
			K	min^2	$(\times 10^{-3})$	$(\times 10^{-3})$		pc	°E of N	$M_\odot$	$M_\odot$
		IRAS(other names)	12μm	25μm	60μm	100 μm					
			Jy	Jy	Jy	Jy					
58	002A	22h 26m 20s, -83d 35m 58s	23.0	90.6	0.16	0.188	0.59	0.32	98	48±9	17
		22278-8341	<0.36	<0.25	<0.40	2.56					
59	422B	22h 41m 33s, 73d 33m 48s	24.1	12.5	0.20	0.207	0.48	0.18	55	18±4	16
		22412+7332(X2241+735[5])	<0.25	<0.25	<0.40	2.98					
		22422+7333(RAFGL 2949[6])	0.25	<0.33	<0.40	<2.05					
60	422B	22h 47m 58s, 73d 18m 2s	23.8	15.6	0.20	0.216	0.25	0.20	90	23±5	13

3.6.1 Uncertainties and Errors

Given the similarity between the methods used here to create column density maps of cloud cores and those used by Woods et al 1992, it is worth re-iterating the discussion they gave on errors and assumptions.

In making the maps, 5 assumptions are made; that the dust is optically thin at 60 and 100μm, that the emissivity is proportional to a power law (equation 3.3) with index $\beta = 1$ (from Hildebrand (1983) who uses the Kramers-Kronig relation for emissivity valid when $\lambda >$ a the typical size of the grains), that the 60 and 100μm emission subtends the same solid angle, that the dust in the IRAS beam is at a single temperature, and that the absolute surface brightness of the cloud has been correctly estimated.

The resulting maps produced all had low optical depths, validating the first assumption. Hildebrand (1983) argued that at the wavelengths covered by IRAS, $\tau \propto \lambda^{-1}$. Wood et al 1992 found that their results were not significantly affected by assuming $\tau \propto \lambda^{-2}$. By using surface brightness instead of intensity/ beam and because clouds structures clearly exist on a scale much larger than the beam size the third assumption, that the 60 and 100μm emission subtends the same solid angle, seems valid.

For these reasons Wood et al 1992 concluded that the major source of errors would arise from the last two assumptions. They further argued that the assumption that the dust in the IRAS beam is at a single temperature is generally accurate except in the vicinity of an embedded star, where 'holes' appear in the structures. This phenomenon is however readily apparent and I have discussed it earlier.

Therefore I conclude that the largest error is due to the estimate of surface brightness. I have discussed at length the technique used, but it is worth noting that Woods et al 1992 concluded that an error of 10-15 percent in the derived ratio of 60 to 100μm surface brightness would lead to a 40 percent error in the derivation of optical depths and that this error reduces to a few percent away from the ecliptic. Given that the work here improves on Woods et al 1992, by both using a dataset which has Zodiacal emission largely removed and concentrating on areas of the sky where background intensity is readily apparent, I conclude that our work is likely to be at least as accurate. The fact that the masses derived here from optical depth maps of L1689 and in Loren et al (1989) from ^{13}CO agree to within $\sim$ 20 percent supports this argument.

Systematic errors in the derived masses are probably larger. The dust column density to H_2 ratio is likely to be uncertain to at least a factor of 2. However given that this factor is derived from a correlation with A_v, comparison with results of other catalogues, which have properties derived in a similar way from molecular observations may well be more accurate than this. The assumed distances of the cores

are thought to be the major error source in deriving masses.

3.7 Discussion

3.7.1 Are the Cores Gravitationally Bound?

The Jeans mass for each core was calculated, as was the ratio of actual mass to Jeans mass. The vast majority of the cores (44 out 60) have a total mass greater than the Jeans mass, indicating that they are gravitationally bound, and stable against disruption from small pressure fluctuations. In fact if they have no support other than pressure gradients, they are likely to collapse.

As discussed above, the fractional abundance of the dust emitting at the IRAS wavelengths must be thought of as uncertain. Using equation 2.38 one can see that the ratio of M to M_J is proportional to $M^{3/2}$, so that if the correct dust abundance is 2 times higher than assumed for a particular core, the mass of the core is 2 times higher than the derived value, and the ratio of M to M_J is ~ 3 times higher than derived. Therefore the ratio of M to M_J is more dependent on the uncertainties in the dust abundance than is the M, and this uncertainty has a strong bearing on my conclusion that the majority of the cores presented in this work are gravitationally bound.

3.7.2 Are the Cores Forming Stars?

Examples of the far infrared spectra of young stellar sources are given in Adams et al (1987), and Andre, Ward-Thompson and Barsony (1993). Class Is can peak at the IRAS wavelengths or longer, Class 0s peak well longward of 100μm in the submillimetre. The archetypal Class 0 is VLA 1623 was not even detected by IRAS and at least one known exsample of a Class 0 is known to be detected at only 100μm (Ward-Thompson et al 1995) . The sample of cores presented here has a number of associated IRAS point sources which could well be indicative of prestellar sources peaking first longwards of 100μm. However only with follow up observations extending the submillimetre and infrared coverage and searches for radio emission and molecular outflows can the individual cores unambiguously be identified as being sites of star formation.

In order to investigate whether the cores contained a surplus of astronomical objects, all the IRAS point sources within a core radius were recorded. These point sources are listed in Table 3.2 under the

entry for each core. The flux densities of each IRAS point source are also listed.

Some cores will have associated sources due purely to chance alignments. In order to estimate what part of the observed sample of point source associations were random alignments two 'control samples' were produced by offsetting the core positions by first 2 degrees and then 5 degrees in declination, and otherwise selecting the IRAS point sources in the same way. In effect we produced 2 false populations of cores made up of the same number of cores, each with the same size and ellipticity, one of which was located (the 2 degree offset population) in the clouds, and one of which was located outside the clouds, but neither of which was located near real cores.

In the sample produced at 2 degree displacement I found 10 sources. 4 were detected only at 100μm, which are probably cirrus sources. 5 sources were detected at 12 and 25μm all of which were brighter at 12μm than 25μm and are therefore thought to be main sequence field stars (1 had been positively identified as a B star). One source, which was detected at all wavelengths and had a steadily increasing flux with wavelength, had been catalogued as a galaxy in the Upsala general catalogue of galaxies.

In the sample produced at a displacement of 5 degrees there were 10 sources, 4 of which were 100μm only sources, and 6 of which were detected at both 12 and 25μm and were brighter at 12μm and again were attributed to field stars.

There does not seem to be any evidence for a significant difference between the control sample either due to the increased displacement, or the location inside and outside the clouds. It can be concluded that the genuine set of cores will contain roughly 10 random associations of which about half will be 100μm only cirrus sources and half will have spectra indicative of main sequence field stars.

The real sample actually contained 21 sources which consisted of: 11 100μm only sources; 5 sources detected at 12 and 25μm and brighter at 12μm than 25 (and therefore consistent with main sequence field stars); 2 sources clearly peaking at a wavelength greater that 100μm (and detected at 2 or more wavelengths); 2 clearly peaking longword of 12μm; and 2 clearly peaking longword of 25μm.

By subtracting the control sample from the core sample we find that the cores seem to contain a surplus of approximately 6 100μm only sources, 2 sources peaking at a wavelength longer than 100μm, 2 at wavelength longer than 25μm, and 1 peaking at a wavelength longer than 12μm. All of these sources have an intensity increasing with wavelength throughout the IRAS wavebands.

The results are summarised in Table 3.3. It is possible that some of the sources may be galaxies, as is indicated by the presence of the galaxy in one of the control samples. The 3 strongest candidate

Table 3.3: Table summarising the population of associated point sources, the two control populations, and the inferred population of sources contained in the cores.

Associated with cores	Control sample 1	Control sample 2	Contained in Core
11 100μm only	4 100μm only	4 100μm only	7 100μm only
5 field stars	5 field stars	6field stars	
2 sources peak >100μm	galaxy (peak >100μm)		1-2 sources peak > 100μm
2 sources peak >25μm			2 sources peak >25μm
1 source peak >12 μm			1 source peak >12

protostars; IRAS 02368+7453, IRAS 07299-4644, and IRAS 21426+6556 were not selected as galaxies for the PSCz redshift survey (W. Saunders personal communication). However the major problem with using the same dataset to identify cloud cores and protostellar candidates, is that an IRAS point source might be the cloud core itself, (Reach et al 1993). Therefore the number of point sources should be interpreted with caution, and is likely to include a number of 'false point sources'.

3.7.3 Comparison with Other Work

In order to investigate fully the differences between the catalogue of cloud cores presented here, and previously studied samples, I now discuss in detail previous work by Myers et al (1983), Beichman et al (1986), Bourke et al (1995), Clemens and Barvainis (1988), and Wood et al (1992). In particular I discuss the typical optical depth, number density, and protostellar content of each survey.

Myers et al (1983) surveyed 90 cores in $C^{18}O$ and ^{13}CO. Using these observations they showed that the cores' $C^{18}O$ optical depth estimated from the ratio of $C^{18}O$ brightness to ^{13}CO brightness was reasonably tightly distributed around a mean of 0.35-0.45. The $C^{18}O$ column density, N_{18}, had a mean of $\sim$ 1.6 $\times 10^{15} cm^{-2}$ with a standard deviation $\sim$ 1.2 $\times 10^{15} cm^{-2}$. This led them to estimate a typical $N(H_2)$ column density of $\sim$ 1.0 $\times 10^{22} cm^{-2}$. Bourke et al (1995) split his sample into a set of Bok globules, and a set of cloud cores, and found that both sets where tightly distributed around mean NH_3 column densities of $10^{14.4\pm0.1}$ and $10^{14.8\pm0.1}$ cm^{-2} respectively. These can be converted into $N(H_2)$ column densities of 5×10^{21} and 1.6×10^{22} cm^{-2} using a typical value for $n(H_2)$ to $n(NH_3)$ of 2.2×10^7 as seems reasonable on examination of the values derived for each core individually from the multitransition NH_3 observations presented in Bourke et al (1995). All though it is true that NH_3 abundances are dependent on chemistry and evolution of the clouds (e.g. Ruffle et al. 1998) it should be emphasised that in this case the value

used for the NH_3 abundance is a directly measured one. Clemens and Barvainis (1988) were not able to derive column densities for their cores, but in a later study, IRAS images of the catalogue's cores were studied (Clemens et al 1991) and a typical 100 micron optical depth of 2.5 $\times 10^{-4}$ was derived. From this we can estimate a column density of 5.0 $\times 10^{21}$ cm^{-2} using the arguments presented in Section 3.6. Wood et al (1992) found that their catalogue had a mean column density $\sim 4.5 \times 10^{21}$ cm^{-2}.

The mean number density of the cores in each survey has also been estimated. Myers et al (1983) estimated that the typical number density in their set of cores is $n(H_2) \sim 8 \times 10^3 cm^{-3}$. Bourke et al (1995) found that their set of cloud cores and Bok globules had typical $n(H_2)$ number densities of $3 \times 10^4 cm^{-3}$ and $10^4 cm^{-3}$ respectively. Wood et al (1992) did not quote a typical number density but a value can be estimated from their column density if a typical radius for the cores is known. What value to use is complicated by the fact that they defined cores to be areas with visual extinction, $A_v > 4$. This leads to the inclusion of several very large cores (their largest was 329 pc^2) which skews the mean to a value much larger than the median. I therefore prefer to use the the second quartile boundary of radius, which is $\sim$ 0.5pc, leading to an estimate for the typical number density of 3×10^3 cm^{-3}. By using the median one uses a value more representative of the majority of cores and isolates the physical conditions of the cloud cores rather than larger cloud complexes. The typical number densities of the Clemens and Barvainis (1988) cores, can also be estimated if the typical size of the cores is known. Clemens et al (1991) claim that the typical radius of the cores is 0.35pc. This was calculated from the mean solid angle of the cores and an assumed distance of 600 pc. This distance estimate is highly uncertain. It was derived originally in Clemens and Barvainis (1988) from two facts: firstly that the cores were generally within 12 degrees of the Galactic plane, and secondly that the cores had LSR velocities of between 0 and 10 kilometres per second. Bourke et al (1995) argues that because the cores are seen in extinction against the background stars of the Galactic plane the survey is biased towards detecting cores near the plane and a better estimate of the typical distance is 300 pc. Using this value a typical radius of 0.175pc is derived, and a $N(H_2)$ column density of 4.8 $\times 10^3 cm^{-3}$ is calculated. This is significantly higher than the value quoted by Clemens et al (1991), mainly due to the different distance assumed, but also partly because I have used the same relationship as Wood et al (1992) used for calculating column density from 100 micron optical depth. Lemme et al (1996) in a study of a subset of the Clemens and Barvainis cores seem to confirm the conclusion made here that Clemens et al (1991) may have significantly underestimated the typical density of the cores in the Clemens and Barvainis (1988) sample.

Beichman et al (1986) studied the embedded stars within the set of cores studied by Myers et al (1983). They used the IRAS point source catalogue, and used a priori selection criteria to define embedded sources. They selected all sources detected at 25μm, or at both 60μm and 100μm, and found 35 of the cores had

IRAS sources meeting the selection criteria while 43 had no IRAS sources meeting their selection criteria. Bourke found that 27 of 76 Bok globules had IRAS point sources satisfying the same selection criteria as Beichman et al (1986), and 36 out of 59 of the cloud cores had suitable sources. Wood et al (1992) used a slightly different selection criteria. They first discarded all sources with a 12μm flux larger than the 25μm flux because they were probably main sequence stars. They then included all sources detected at either 25μm or 60μm, as long as they were also detected at one other wavelength. They found that 59 out of 255 cores had at least one embedded source. I studied all the IRAS sources associated with cores in Clemens and Baravainis (1988). 65 cores (out of 248) have IRAS sources associated with them which would have passed the Beichman et al (1986) selection criteria. It is worth noting however that a further 21 had sources similar to the 60 micron only detections seen in the sample presented here, and that they found a definite excess of 100 micron sources. This confirms the conclusions discussed above that there are a clear excess of IRAS sources associated with cloud cores which are not picked out by the Beichman et al (1986) selection criteria. These are typically low luminosity, and seen often at only one wavelength. It is worth noting that they may well constitute a population of low luminosity or low mass YSOs.

Similar properties have been derived for the sample of cloud cores presented here. The histogram of mean column density for the 60 cores is plotted in Figure 3.24. The sample is a reasonably tight distribution around a median 100 micron optical depth of 0.19 $\times 10^{-3}$ and therefore a column density of $3.8 \times 10^{21}\mathrm{cm}^{-2}$, using the two assumptions outlined in section 3.6 (specifically that $A_v \sim 2 \times 10^4 \tau_{100}$ and that $N_{H_2}(cm^{-2}) \sim 10^{21} A_V$). The mean is skewed high due to a small number of cores with significantly higher optical depths. The median radius of the cores with definite distances is 0.31pc (derived assuming the cores are roughly spherical), and again this mean value is skewed to the higher value of 0.41pc. The number density typical of the cores in my sample is $\sim 2 \times 10^3\mathrm{cm}^{-3}$, when derived by dividing the typical column density by the typical diameters of the core (when 'typical' is both taken as either the median or the mean set of values).

There is a clear excess of IRAS sources in the cloud cores presented here. If one discards the 100μm only sources, as being an uncertain indicator of embedded sources it appears that 4 of the cores have at least one embedded source. The study presented here clearly supports the assumptions made in previous studies to discard sources with a larger flux at 12μm than 25μm.

3.7.4 The Star Formation Timescale

In trying to determine the nature of the IRAS point sources located in the Myers et al (1983) set of cores, Beichman et al (1986) estimate the lifetime of a core with an embedded Young Stellar Object. In

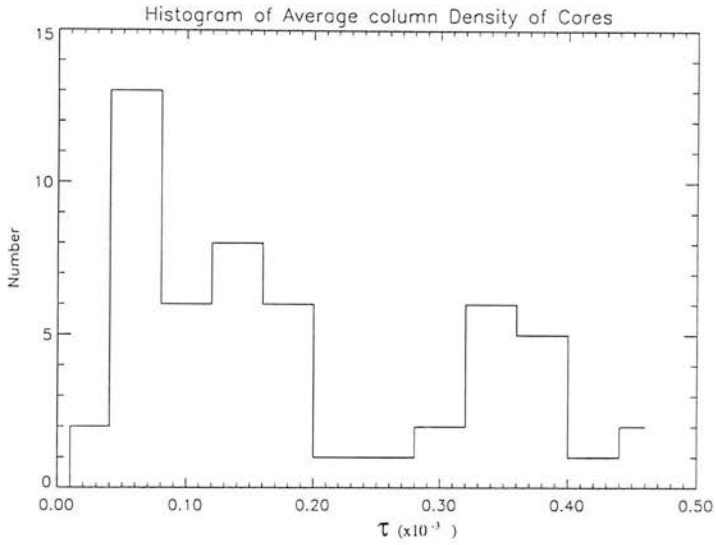

Figure 3.24: Histogram of the column density of cores in the catalogue presented here.

particular two timescales are important, the first being the time that a pre-main sequence star is visible to IRAS, given its sensitivity limits, and the time in which such a star, born with a velocity component, will move out of the core. Both these timescales can be estimated by looking at models of T-Tauri star evolution or assuming typical velocities that a star will be born with and are likely to be a few 10^6 years (Beichman et al 1986, Ward-Thompson et al 1994). Ward-Thompson et al (1994) make the implicit assumption that the cores without protostellar sources or YSOs are predecessors of the cores with protostars, ie prestellar, and draw statistical conclusions about the prestellar evolution of the cloud cores; in particular the timescale for the formation of a central core detectable in the submillimetre continuum.

Following this line of argument, I here try to infer a statistical estimate of the prestellar lifetime of the cores studied in each sample discussed above. I make the assumptions that in each survey the cores without embedded sources will go on to form protostars. The cores with embedded sources are assumed to have an average lifetime which is the same in each catalogue and equal to the timescale for a YSO to be visible to IRAS as a source with increasing flux towards longer wavelengths (Beichman et al 1986) ie $\sim 10^6$ years. This is presumably true if each core forms stars in a single burst, and each set of cores forms stars with the same IMF. One can then estimate the prestellar timescale, ie the time that a core without an embedded source will take to form a protostar. This is simply expressible as,

$$\tau = \frac{\text{No. of cores without embedded sources}}{\text{No. of cores with embedded sources}} \times 10^6 \text{years}, \tag{3.14}$$

where I have taken the lifetime of cores with embedded sources to be 10^6 years. This is calculated for

Table 3.4: Table Summarising results of surveys of cloud cores.

Survey	$N(H_2)$ cm^{-2}	$n(H_2)$ cm^{-3}	Percentage protostellar	Prestellar $\tau(\times 10^6)$ years
Bourke et al	1.6×10^{22}	3×10^4	61±10	0.6±0.1
Myers et al	1.2×10^{22}	8×10^3	44±7	1.3±0.2
Bourke et al	5×10^{21}	10^4	36±7	1.7±0.3
Clemens et al	5.0×10^{21}	4.8×10^3	27±4	2.82±0.4
Wood et al	4.5×10^{21}	3×10^3	23±3	3.3±0.4
Jessop	3.8×10^{21}	2.0×10^3	$9\pm^6_5$	$10\pm^7_4$

all sets of cores and is listed in Table 3.4. For the cores presented in this work, only the cores which are Jeans unstable have been included.

3.7.5 Errors in Catalogues' Properties

The column densities and the number densities will have errors associated with them due to the assumed fractional abundance of the tracer used in the observations. The values quoted are probably accurate with respect to each other within 20 percent (the error quoted earlier for the work presented here), although a larger systematic error may well exist, and due to the uncertainty, discussed above, about the typical distance to the Clemens and Barvainis (1998) cores, a larger error of 40 percent is assigned to the typical number density derived for this set of cores.

The fraction of cores with embedded sources is likely to be affected by shot noise, and in the catalogues where the number of cores with embedded sources, N, is large the 1σ error can be estimated as $\sqrt{\mathrm{N}}$. The presented in this thesis have a low probability of containing an embedded source (i.e. only four out of 60 contain an embedded source), and therefore the error analysis and uncertainty in derived properties is more complicated. If one considers a random sampling from a normal distribution with average value 16 one finds that a sample value of 4 would be a 3σ fluctuation. Therefore an upper limit of 16 cores having embedded sources, is the 3σ upper limit from my sample.

The errors quoted in Table 3.4, are therefore at least 20 percent on column density and number densities, and $\propto \sqrt{N}$ for the fractional abundance of protostellar cores, and the prestellar timescale, with the exception of the cores presented for the first time in this thesis. For this set the error in column density and number density is also thought to be 20 percent but the quoted error in the protostellar fraction is skewed, as is the error in the derived prestellar timescale. The errors in the derived timescales

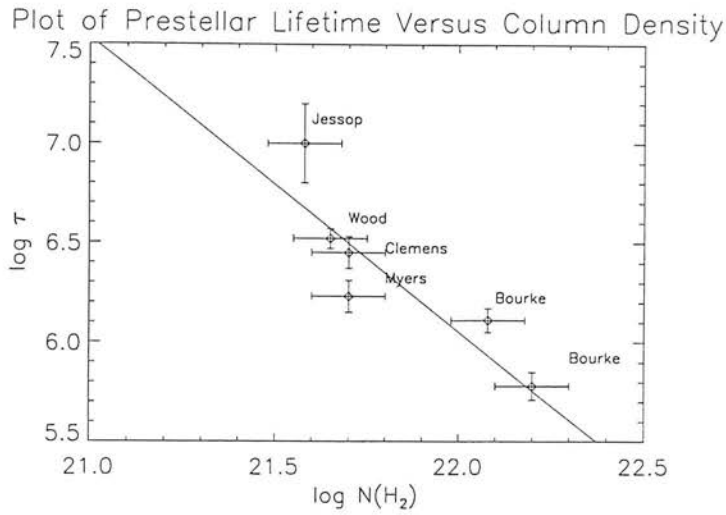

Figure 3.25: Plot of the column density against inferred prestellar lifespan, for various catalogues, a best fit power law of $\tau \propto N(H_2)^{-1.5}$ is also plotted. The reduced Chi squared error on this is 1.5.

has an additional contribution due to the uncertainty in the number of cores without sources, but will not be more than a factor of $\sqrt{2}$ larger than the error in fractional abundance of cores with embedded sources. This has not been included.

An error in the derived timescale may arise because of the assumption made that all sets of cores are forming a similar set of stars with the same IMF. If one set of cores were forming lower mass stars than the others, then both the main accretion phase (ie the protostellar stage) and the T-Tauri lifetime may be significantly different in this set of cores than in the others. Likewise if one set of cores forms stars, not in a single burst, but over a timescale similar to or greater than the lifetime of the YSOs, its derived lifetime will have been significantly underestimated. Given the lack of understanding surrounding the prestellar evolution in cloud cores, and in particular the unknown way in which luminosity depends on mass, age and initial conditions, these assumptions are the simplest scenario one can propose and test.

3.7.6 Discussion

It is apparent from the Table 3.4 that the percentage of cores with embedded sources decreases with both column density and the volume density of the cores. The results are plotted in Figure 3.25 and Figure 3.26.

Power law fits to the data points were also carried out, and the best fits found were; $\tau \propto \rho^{-0.86 \pm 0.15}$

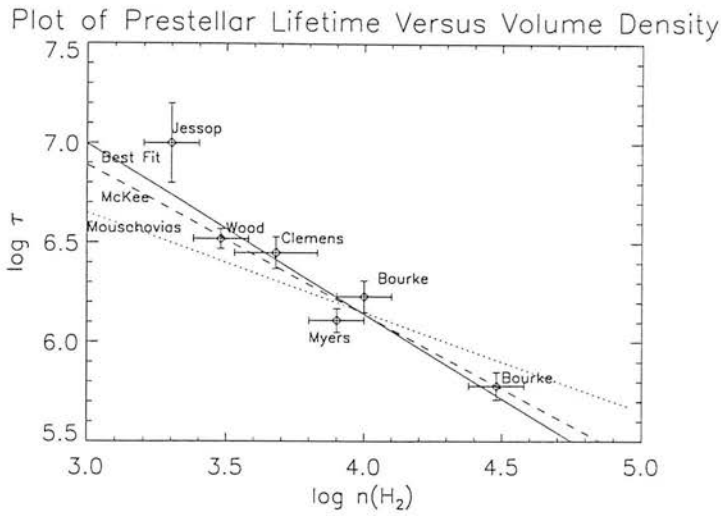

Figure 3.26: Plot of the number density against inferred prestellar lifespan, for various catalogues. A best fit power law of $\tau \propto n(H_2)^{-0.86}$ is plotted as a solid line. The reduced Chi squared error on this is 1.0. A fit showing $\tau \propto n(H_2)^{-0.5}$, is also presented, and is clearly unable to explain the data.

with a reduced chi squared error of 1.0, $\tau \propto N^{-1.5\pm0.4}$ with a reduced chi squared error of 1.5. The fit to the number density plot is clearly better than that to the column density as can been seen by both looking at the plots and the lower reduced chi squared error on the number density fit.

It is interesting to compare the dependance of prestellar timescale here with the ambipolar diffusion timescale. Equation 2.56 shows that the ambipolar diffusion timescale is $\propto \chi_i$, the ionization fraction. In general ionization is caused both by ultra violet radiation and cosmic ray ionization. Mouschovias (1991), for the sake of simplicity, uses the canonical value of ionization level which is assumed by balancing ionizations from Cosmic Rays with recombinations between electrons and ions. Per unit volume the ionizations are proportional to the number of H_2 molecules, $n(H_2)$. The recombinations per unit volume are proportional to the number density of electrons times the number density of ions, or $n(H_2)^2\chi_i^2$ so that for steady state;

$$\chi_i \propto n^{-0.5}, \tag{3.15}$$

which leads to his derivation of ambipolar diffusion timescale being $\propto n^{-0.5}$. This timescale is plotted as a dotted line in Figure 3.26.

McKee (1989) however treats the ionization and recombination in much fuller detail, and incorporates the role of metals, and Ultra Violet penetration. He derives an expression for the star formation timescale which is dependent on both number density and column density (see his equation 4.7, and his Figure

1 which is reproduced here as Figure 3.27). He concludes that for $A_v > 4$ the cosmic ray ionization becomes dominant, and that in this region the star formation timescale decreases roughly as $\propto n^{-0.75}$, only becoming close to the canonical value $\propto n^{-0.5}$ at very high densities. The reason for this stronger dependance of ionization level on number density is due to more than one effect. At very low densities, ie. below McKees 'critical' density of 500, the ionization level is proportional to n^{-1} due to H_3^+ ions dominating the ionization fraction. As the density increases this strong dependance falls towards the canonical $n^{-0.5}$. In the regime between cosmic ray dominated and ultra violet dominated ionization, the star formation timescale is also affected by the amount of UV light penetrating into the core, attenuating the star formation by a factor $\propto n^{(-1.25/A_v)}e^{(16/A_v)}$ - (see appendix B and equations equation 4.6 and 4.7 of McKee (1989) for a derivation). This UV penetration, which is not considered by Mouschovias (1991), can explain why the trend seen in the data for star formation timescale is steeper than would be predicted by $\tau \propto n^{-0.5}$.

Figure 3.26, shows the best fit $\tau \propto \rho^{-0.86}$ as a solid line. It is clear that the data are more consistent with the star formation timescale suggested by McKee (1989), $\tau \propto \rho^{-0.75}$ (plotted as a dashed line), than Mouschovias (1991) $\tau \propto \rho^{-0.5}$ plotted as a dotted line. Although the measured timescale decreases with density slightly more quickly than McKee's prediction it is consistent within the errors. It should also be noted that the increase in opacity between the sets of cores will decrease the star formation timescale and can only steepen the line from $\rho^{-0.75}$. The fact that the correlation presented here between star formation timescale and density is so close to that suggested by McKee strongly implies that the cores studied are situated in the transition regime where cosmic rays and UV radiation are both important. A simultaneous fit of McKee's star formation timescale to both figures 3.24 and 3.25 seems to confirm this view.

3.8 Summary and Conclusions

I have produced a catalogue of opaque regions in nearby molecular clouds, and derived physical characteristics for them. About three quarters of the cores are bound against pressure perturbations, and therefore likely to contract under their own self gravity. At least 4 out of 60 of the cores have evidence of protostellar content, as evidenced by a detection of an IRAS point source. A further 5 cores may have evidence of star formation but this is ambiguous due to cirrus confusion. Comparison with other catalogues of opaque regions shows that the percentage of protostellar regions within a catalogue increases with both the typical column density and number density of the regions studied in the catalogue. Fits to this trend show that if the cores are governed by simple ambipolar diffusion, then they are not simply supported

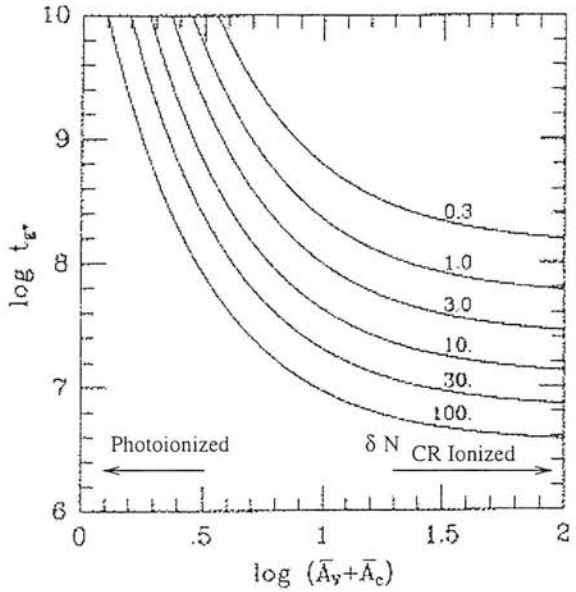

FIG. 1.—The star formation time scale t_{g*} (the time for the molecular gas to be converted completely into stars) is plotted as a function of the total extinction $\bar{A}_v + \bar{A}_c \equiv \bar{A}$, for the "standard" ionization case (see discussion of eq. [4.7]). The time scale is shown for different ratios of the density in a clump n_H to the characteristic ionization density n_{ch}; for the standard case, $n_{ch} = 500\delta_{tr}^{-2}$ cm^{-3}.

Figure 3.27: Figure 1 of McKee 1989 showing how the star formation timescale is dependent on column density and number density. At low column densities the star formation rate is attenuated by U.V. ionization. As the column density increases the U.V ionization becomes less important and the star formation rate becomes regulated by the number density of the gas, with $\tau \propto n^{-0.75}$.

by cosmic ray ionization, and the canonical ionization level assumed by (amongst others) Mouschovias (1991). This result is however consistent with McKee's (1989) molecular cloud model, in that the cores studied are in the regime were UV and CR ionization mechanisms are both important.

Chapter 4

Prestellar Cloud Cores

4.1 Introduction

In the previous chapter I produced a catalogue of cloud cores and found that a proportion of the cores were gravitationally bound and that some of the cores showed evidence of a YSO content. Any core which has formed a young stellar object can be said to have entered the protostellar stage. By using higher resolution observations one can hope to probe the internal structure of cloud cores, and put constraints on the physical processes which lead to the formation of cores, and the processes which will influence their ongoing evolution. A high resolution continuum study by Ward-Thompson et al (1994) showed that a sample of Molecular Cloud Cores had structures indicative of the ambipolar diffusion models of Mouschovias (1991) and very different from the singular conditions predicted by Shu et al (1987). Further work has shown velocity structure in one of the cores consistent with ambipolar diffusion (Myers et al 1996), and in a study of another of the cores Kuiper et al (1996) found evidence that accretion onto the cores may well play a significant role in the build up of their mass, while ambipolar diffusion is leading to increased central density. In this chapter I present a $C^{18}O$ study of a set of these cores, and measure brightness temperatures for several cores in order to probe further into the physical processes which dominate the evolution of molecular cloud cores. In the penultimate chapter I will present a detailed model of one of these cores.

4.2 Observations

The observations were carried out at the James Clerk Maxwell Telescope (JCMT), located on Mauna Kea, Hawaii, on 1995 July 18th, 22nd and 25th 17:30–01:30 HST (UT = 03:30–11:30), on 1996 August 31st and September the 1st 17:30–01:30 HST (UT = 03:30–11:30) and on 1996 September 8th and 9th 01.30–09.30 HST (UT = 11.30–19.30). Some observations were also taken during flexible UK service observing time in January and February of 1997.

The $C^{18}O(J=3\rightarrow2)$ transition (rest frequency of 329.33 GHz), the $C^{18}O(J=2\rightarrow1)$ transition (rest frequency of 219.56 GHz) and the $C^{17}O(J=2\rightarrow1)$ (rest frequency of 224.71 GHz) were all observed using the common user heterodyne receivers RxB3i (Cunningham et al 1992) and RxA2 (Davies et al 1992). The JCMT HPBW is 19 arcsec at 220GHz and 14 arcsec at 330Ghz. Double-sideband system temperatures were 2000-12000 K for the receiver B and 480K for receiver A observations. The backend used was a digital auto-correlation spectrometer, with a resolution of 378kHz and 95 kHz per channel, for the $J=(3\rightarrow2)$ and $J=(2\rightarrow1)$ transitions respectively, corresponding to 0.34 kms^{-1} at $J=(3\rightarrow2)$ and 0.13 kms^{-1} at $J=(2\rightarrow1)$. Data reduction was carried out using the SPECX package (Padman 1990).

Two types of observations were carried out throughout the observing run in order to check the performance of the telescope. The first type of observations were regular pointing checks. These are of bright sources observed using the continuum backend. Five observations are made, one at the expected position of the bright source, and 4 offsets. This is known as a 'five point' or 'pointing observation'. If the telescope is pointed correctly the central position should be brighter than the offsets, which should all have the same brightness. An automatic fitting routine gives the offset of the telescope from the source which is recorded in the observing log. In order to try and calculate the accuracy to which the telescope was pointing the absolute offset value for all the pointing observations are plotted against time in Figure 4.1. We can see that at worst the pointing was accurate to within 5-6 arcseconds.

The second type of observations carried out were used to check the overall performance of the telescope when observing a particular spectral line. Once the receiver has been tuned to the correct frequency a visible standard source was observed. This is known as 'sampling a standard'. This spectrum could then be compared to an available predicted spectrum for the standard source. For a perfectly performing telescope the two should be the same. The ratio T_{pk}(measured)/T_{pk}(standard) can be used as a measure of the performance of the receiver systems (eg: for a perfectly performing telescope this value should be 1). In Figure 4.2 the measured values of T_{pk}(measured)/T_{pk}(standard) for all the $C^{18}O(J=2\rightarrow1)$ and $C^{18}O(J=3\rightarrow2)$ observations taken throughout the run are plotted. For $C^{18}O(J=2\rightarrow1)$ the measured value of T_{pk}(measured)/T_{pk}(standard) varied between 0.85 and 1.0 and for $C^{18}O(J=3\rightarrow2)$ the measured

value T_{pk}(measured)/T_{pk}(standard) varied between 0.6 and 0.8 in the first run and 0.5 and 1.0 in the second run.

As noted in the JCMT Astronomers Manual (Mathews 1994) there are several reasons why the observed spectra may be less bright than expected. The most relevant to these observations were probably variations in the sky opacity, pointing errors, focusing errors and internal problems within the receiver. Inaccurately pointing the telescope towards a compact source leads to a fall in the observed brightness (16% at 0.25 beam of the source.) Similarly, a focusing error will lead to the observed brightness falling (0.5mm error in z position leads to a 10% fall at 345GHz.) Both of these errors could lead to a fall in the observed brightness of compact standard sources, but would not significantly reduce the observed brightness of extended sources.

'Sky variations' are due to the atmospheric opacity changing with time between calibration measurements. For calibration of sources this can lead to a 6% variation in the observed brightness of sources in good conditions and up to a factor of 2 variation in poor conditions. Internal problems with the receivers can also occur and it is believed that in the first observing run there were such problems with receiver B3i. Both of these errors may boost as well as reduce the observed brightness of spectra of compact and extended sources.

If the the dominant errors are pointing and focusing one would expect the variations observed in the standard compact source spectra to not affect the spectra obtained for the extended cores. If the dominant errors are internal receiver problems and sky variations then a correction has to be applied to correctly calibrate the spectra observed. If the variations in Figure 4.2 are due to these errors then the $C^{18}O(J=2\rightarrow1)$ spectra observed would have been systematically reduced by $\sim 0.95 \pm 0.05$ and the $C^{18}O(J=3\rightarrow2)$ spectra would have been systematically reduced by $\sim 0.7 \pm 0.1$ in the first run and a factor of 0.7 ± 0.43 in the second run.

4.3 Data Reduction

The data obtained were either in the form of a single pointed spectrum, or a series of spectra at different positions which could be built up into a data cube- essentially a map with velocity information. In both cases the basic data format obtained is a spectrum whose intensity is given in terms of the antenna temperature T_a^*. These spectra were calibrated regularly using the the standard chopper wheel method (Kutner and Ulick 1981).

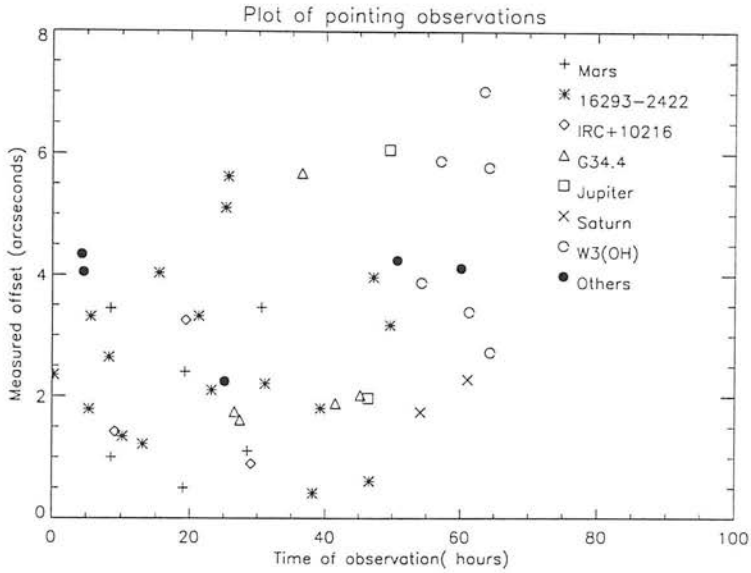

Figure 4.1: Plot of all the pointing observations throughout the entire 69 hours of Observations. In run 1 (1-24 hrs) the pointing was accurate to $\sim$ 4 arcseconds, in run 2 it was accurate to $\sim$ 6 arcseconds.

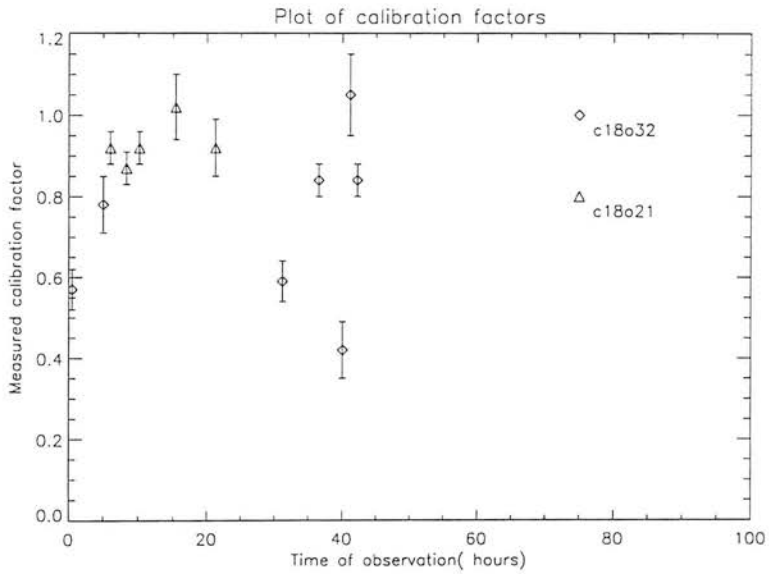

Figure 4.2: Plot of calibration values for the $C^{18}O$ (J=2$\rightarrow$1)and $C^{18}O$(J=3$\rightarrow$2) transitions throughout the observing. In run 1 (1-24hrs) the measured $C^{18}O$(J=3$\rightarrow$2) intensities of standard sources was 0.7 $\pm$ 0.1 times the predicted value and the $C^{18}O$(J=2$\rightarrow$2) was 0.95 $\pm$ 0.05 times the predicted value. In run 2 the $C^{18}O$(J=3$\rightarrow$2) was 0.7 $\pm$ 0.3 times what was predicted.

The JCMT telescope has a response to sky surface brightness which is directional, this directionality can be characterised in terms of the power pattern of the antenna (Rohlfs 1986). This means that the telescope is not perfectly coupled to the source (i.e. the received intensity at receiver input is a spatial convolution of the power pattern, and the brightness pattern in the sky - eqn 5.49 of Rohlfs 1986) , and a correction factor η has to be applied in order to calculate the radiation temperature of the source T_r. This coupling constant is dependent on the spatial extent of the source.

The antenna brightness temperature T_a^* is mostly commonly converted into either the standard main beam brightness radiation temperature T_{mb} or the radiation temperature T_r (Stark et al 1996). These are related as follows:

$$T_{mb} = T_a^*/\eta_B \tag{4.1}$$

$$T_r = T_a^*/\eta_{fss} \tag{4.2}$$

where η_B is the coupling efficiency of a source filling the main beam and η_{fss} is the coupling efficiency of an extended source the size of the moon to the telescope antenna pattern (Mathews 1994). In this case the sources were expected to be considerably more extended than the main beam but significantly less extended than the moon, which is used to calculate η_{fss}.

One can further take into account the corrections discussed in the section above and using the suggested values η_B=0.69±0.01 , η_{fss}=0.8±0.05, for receiver A and η_B=0.58±0.03 , η_{fss}=0.7±0.1 for receiver B (JCMT fact sheet) we get the following equations for receiver A:

$$T_{mb} = T_a^*/0.65 \pm 5\% \tag{4.3}$$

$$T_r = T_a^*/0.76 \pm 6\% \tag{4.4}$$

and for receiver B (in the first run):

$$T_{mb} = T_a^*/0.4 \pm 10\% \tag{4.5}$$

$$T_r = T_a^*/0.5 \pm 20\% \tag{4.6}$$

In the following sections when the results are presented they are given in terms of T_a^* but the modeling presented in chapter 5 the best comparison is made by converting values to T_{mb}.

Table 4.1: Summary of spectral line observations in units of T_a^*(K)

Core	$C^{18}O$ (J=2→1)	$C^{18}O$ (J=3→2)	$C^{17}O$ (J=2→1)
L183	1.9 ± 0.07(map)	< 3.3	
L1689A	2.6 ± 0.07(map)		
L1689B	3.73 ± 0.05(map)	2.0 ± 0.2(map)	1.8 ± 0.14 (map)
L63	2.1 ± 0.07(map)	< 2.7	
B133	1.56 ± 0.04(map)	0.63 ± 0.3	
L134		< 2.7	
L1544		1.1 ± 0.08	
L1517B		< 2.5	
L1517A		< 2.5	
L1512		< 2.1	

4.4 Single Spectra

I began by observing ten cores detected in the continuum by Ward-Thompson et al (1994), and found that six were detected in either the $C^{18}O$ (J=2→1) or the $C^{18}O$ (J=3→2) transition. L1689B was also sampled in $C^{17}O$ (J=2→1) as this is an even rarer isotope of carbon monoxide.

Table 4.1 presents the results of these observations, for each core and transition sampled. Either a 3σ upper limit is presented or the detected value of T_a^*(peak) is presented with an estimate of the single channel 1σ error. The cores which were mapped are indicated in the table, and the brightest value of T_a^*(peak) in the map is presented. Five out of five cores were detected in $C^{18}O$ (J=2→1) with T_a^*(peak)=1.5-3.8K. Three out of Nine cores were detected in $C^{18}O$ (J=3→2) with T_a^*(peak) = 0.6-2.0K, and the upper limits were 2.1-3.3 K for the other six.

4.5 Mapping Data

Five maps were made of cores in $C^{18}O$ (J=2→1), while L1689B was also mapped in $C^{18}O$ (J=3→2) and $C^{17}O$ (J=2→1). Data cubes were made from the separate spectra using SPECX. This allows one to make maps of the brightness temperature of the sources for different velocity slices.

4.5.1 Data Analysis

The instrument noise can be characterized by looking at the variation in signal from channel to channel at a different frequency from that of the spectral line. One can use the standard deviation of these values as a measure of the 1σ noise in each channel and hence as an error on T_a^*(peak). If we wish to integrate the signal across a velocity range (or number of channels, n) -say to get the total signal from the whole line, then the 1σ variation in this value should be $\sigma/\sqrt{n}$.

However two main problems became apparent which needed a more detailed treatment of the noise. First frequency switching was available for receiver B observations. This was used because twice as much time is spent 'on source' compared to the standard position switching, therefore gaining a $\sqrt{2}$ improvement in signal to noise. Unfortunately this technique also produces a sinusoidal-like baseline with short wavelength due to internal reflections within the DAS. This contributes to the uncertainty in T_a^*. Secondly when maps are made one wants to obtain a good estimate of the typical noise features. Clearly the more pointings in the map the larger the typical range of noise features. Because of these problems an extension of the simple channel to channel estimator of noise was developed for the maps.

One should be aware that the maps observed of the molecular brightness are a combination of the real structure plus noise structure, therefore before interpreting a structure as real it is important to try to quantify the typical noise structure one expects in the map. Again because the line observed occurs over a small part of the DAS bandwidth one can quantify the noise by analysing the off spectrum signal. One can for example make several realisations of the maps off the spectral line which will reveal the typical noise structures. A key parameter is the brightness difference between the minimum and maximum pixels- ie the peak to peak noise.

Several maps were made at frequencies off the spectral line, spanning the same velocity range (δ_v), but at different velocity offsets and histograms were plotted of the difference between maximum and minimum features in these maps. The distribution of this parameter was found not to be Gaussian. This process was then repeated for different values of the velocity range. Generally when the noise is totally random we would expect $\sigma \propto 1/\sqrt{\delta v}$ where δv is the velocity range. As an estimate of the average features seen in the noise maps, the average value of $(T_{max} - T_{min})$ was used.

Results for the L1689B $C^{18}O$ (J=2→1) and $C^{18}O$ (J=3→2) maps are presented in Figure 4.3. The $C^{18}O$ (J=2→1) map was made using position switching. The $C^{18}O$ (J=3→2) using frequency switching. In both cases the average values of $(T_{max} - T_{min})$ decreases with increasing δv. For both cases the results obtained for noise maps redshifted off the line (the crosses) and blueshifted off the line (the

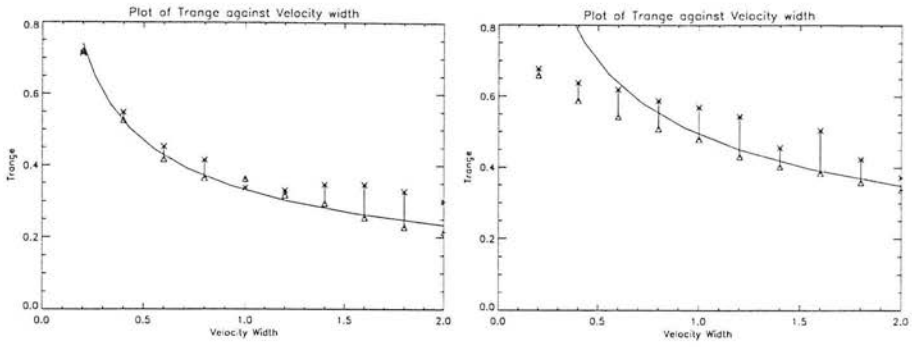

Figure 4.3: Example of type of graphs produced to help set contours. The graph shows the average value of the temperature range found in noise maps $\overline{T_{range}}$ against the velocity width integrated over. The first graph shows the results for the L1689B $C^{18}O$ (J=2→1) map and the second for the L1689B $C^{18}O$ (J=3→2) map. In both maps the triangular symbols show the average results for maps made in the range -4.0 km/s to 1.0 km/s and the crosses show the maps in the range 6.0 km/s to 11.0 km/s (blue shifted and redshifted from the line respectively). A $\overline{T_{range}} \propto v^{0.5}$ fit is given for both cases.

triangles) are presented. In both cases one can see that the redshifted maps are noisier, possibly due to an increase in receiver efficiency dependent on the position chosen in the DAS bandwidth. In both cases a $(T_{max} - T_{min}) \propto 1/\sqrt{\delta v}$ fit is shown. The $C^{18}O$ (J=2→1) position switched map follows this trend for all δ_v, but the $C^{18}O$ (J=3→2) map (frequency switching) has a flatter $(T_{max} - T_{min})$ for small δv. This illustrates the well-known fact that frequency switching produces small scale wavelets due to internal reflections. The point at which the fit breaks away from the observations indicates the velocity range over which the wavelets are coherently organised. They are not regularly spaced and it is not possible to fit a sinusoidal baseline. This limits the effectiveness of using frequency switching for high velocity resolution work.

In the maps constructed of $C^{18}O$ emission the contour interval used was the average value of $T_{max} - T_{min}$ measured in the noise maps. We will refer to features which are only one contour in height as one contour features. This means that although one-contour features occur in noise maps constructed off the spectral line, two contour features rarely do, and can be interpreted as being real when observed. In order to use the full velocity information, channel maps were produced (ie several maps were constructed by integrating over a velocity less than the line width). For small velocity-range maps the noise is often so high as to drown out any features. In such cases I increased δv (and adjusted the contour levels used in the map accordingly) until at least one of the channels contained double contour features, or until δv encompassed the whole line (this process is effectively trading velocity resolution for signal to noise).

4.5.2 $C^{18}O$ (J=2→1) maps of Four Prestellar Cores

Data relating to B133, L183, L63 and L1689A are presented in this section. I analysed the maps in the following way.

- I produced T_{range} against δv plots for noise maps in each case.
- I inspected the line profiles to see if the lines were single component Gaussians.
- Channel maps of small δv (0.2km/s) were made using the appropriate contour levels.
- If the maps were featureless (swamped by noise) then δv was increased, losing velocity resolution but increasing signal to noise.
- I repeated this procedure up to the point where δv was the same as the line width of the central spectrum.

This reason for using this procedure was to obtain maps with as high velocity resolution as possible given the signal to noise. The procedure essentially started with the highest velocity resolution obtainable, but the lowest signal to noise, and decreased the velocity resolution untill a significant amount of signal to noise in the maps was obtained. For B133, the value of δv had to be increased to cover the whole line width. The map (Figure 4.4) seems to have a ridge of high intensity running east-west. This feature has a brightness variation twice that seen due to noise alone.

For L183, the value of δv had to be increased to cover the whole line width. The map (Figure 4.4) seems to show three peaks one at 10 arc seconds to the north of the map centre; one 20 arc seconds to the southwest; and one 35 arc seconds to the east-northeast. These three features are brightness variations typically seen due to noise alone.

For L63 (Figure 4.5), the value of δv was increased to cover the line width. It seems to show a ridge running north south, and the brightness variation across the ridge is approximately twice that seen due to noise alone.

The L1689A map had three spectral components. A map showing the observed spectrum at each point is presented (Figure 4.5). A channel map showing the integrated intensity of the three components is also shown (Figure 4.6). This map seems to show the 3.4km/s component peaking to the south, the 4.2km/s component to the north and the 5.0km/s component peaking to the north west. These features

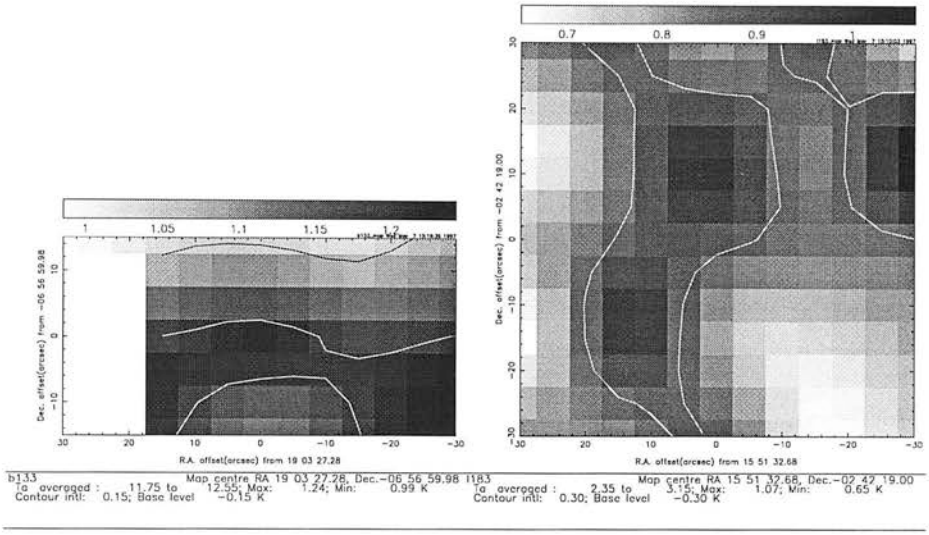

Figure 4.4: $C^{18}O$ (J=2→1) maps of B133 and L183.

are brightness variations respectively 5, 2 and 3 times larger than the variations seen due to noise alone. The maps at 2.6km/s and 5.8km/s are maps off the line and show noise features only.

In these four maps the cores are clearly detected. Even though some variations in surface brightness is detected, these variations are small compared to the average surface brightness. Consequently I have not detected large surface brightness variations in these four objects. This may indicate a genuine lack of density variation, or it may mean that the observed spectral lines are optically thick in these sources.

4.5.3 L1689B Maps in Three Transitions

L1689B was found to be considerably brighter than any of the other cores. $C^{18}O$ (J=3→2), $C^{18}O$ (J=2→1) and $C^{17}O$ (J=2→1) maps were made and are presented here. The maps were reduced in the same way as in the previous section. The $C^{18}O$ (J=3→2) map (Figure 4.7) had to be integrated over the entire line width in order to increase the signal to noise. One can see that there seems to be a broad peak on the centre of the map, which displays a brightness variation typically twice as large as those seen due to noise alone. $C^{17}O$ (J=2→1) displays hyper-fine splitting. This leads to a broadening of the line. In general two distinct velocity components were resolved. In order to increase the signal to noise the map presented in Figure 4.7 was integrated over the velocity range 2.4 to 4.5 km/s, thus encompassing both of the velocity components. Again there seems to be some peaking on centre but here this extends well out to the east and south, and the variation in the surface brightness is again only twice that seen due to noise alone.

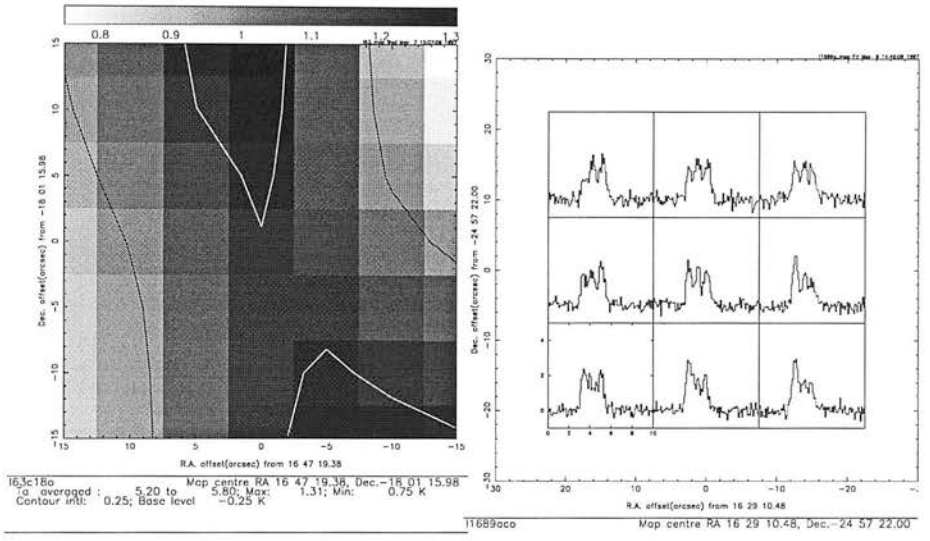

Figure 4.5: $C^{18}O$ (J=2→1) map of L63 and grid-spectrum map of L1689a showing velocity confusion.

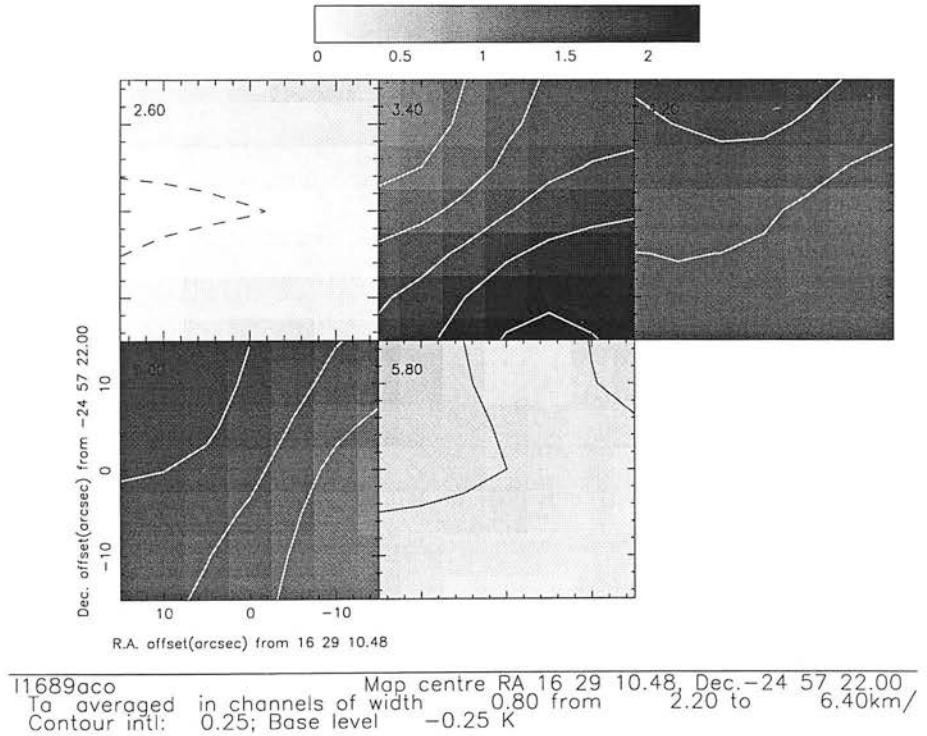

Figure 4.6: $C^{18}O$ (J=2→1) channel map of L1689a.

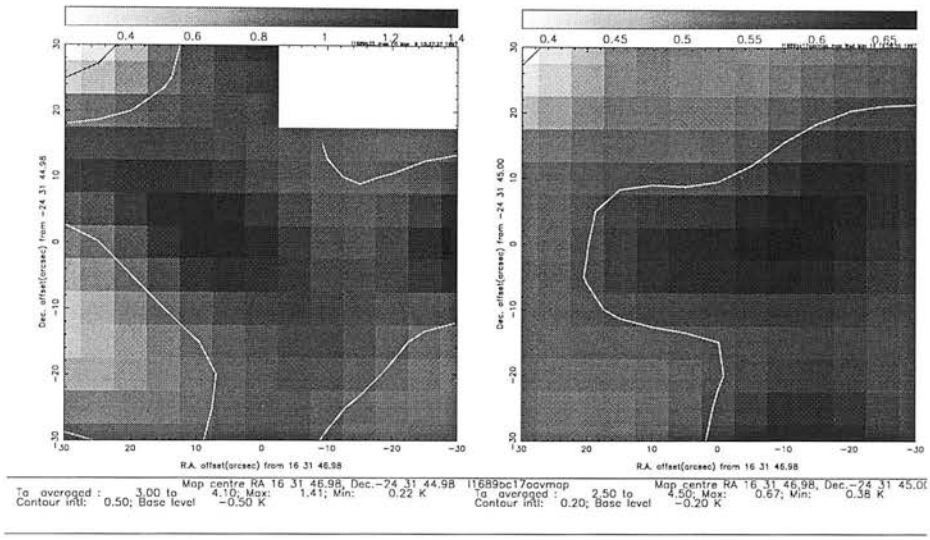

Figure 4.7: $C^{18}O$ (J=3→2) and $C^{17}O$ (J=2→1) map of L1689B.

The $C^{18}O$ (J=2→1) map (Figure 4.8) was found to have high enough signal to noise to show structure when integrated over a velocity range of only 0.2km/s. The maps constructed which were blue shifted from the average line centre ($> 3.7 \text{kms}^{-1}$) peaked on the continuum centre. However the redshifted maps seemed to peak to the east and west. Although this map is the only one constructed which displayed a structure significantly above the noise, the surface brightness in this map still has a low dynamic range (as is illustrated in the following section).

4.6 Summary of the L1689B Observations.

There is a very large amount of data (several individual pointings at different positions for different transitions and isotopes, each of which has velocity information) in each map. In order to facilitate a comparison with spherically symmetric models of the cores, the $C^{18}O$ (J=2→1) and $C^{18}O$ (J=3→2) spectra of L1689B, observed at the same angular displacement from the centre of the core were compared.

A central position 7 arc seconds to the west of the continuum peak was chosen as the core centre, due to the fact that this was where the $C^{18}O$ (J=2→1) seemed to peak. This difference is little more than the pointing error of the JCMT (as shown in Figure 4.1). In terms of angular displacement from the centre, the maps contain in each transition: 2 spectra at 7 arcseconds; 4 at 16 arcseconds; and 2 each at 22, 26 and 32 arcseconds displacement. The results of the comparison are presented in Figure 4.9. For the 4 displacements which had 2 spectra, error bars joining the two intensities are shown, while for the

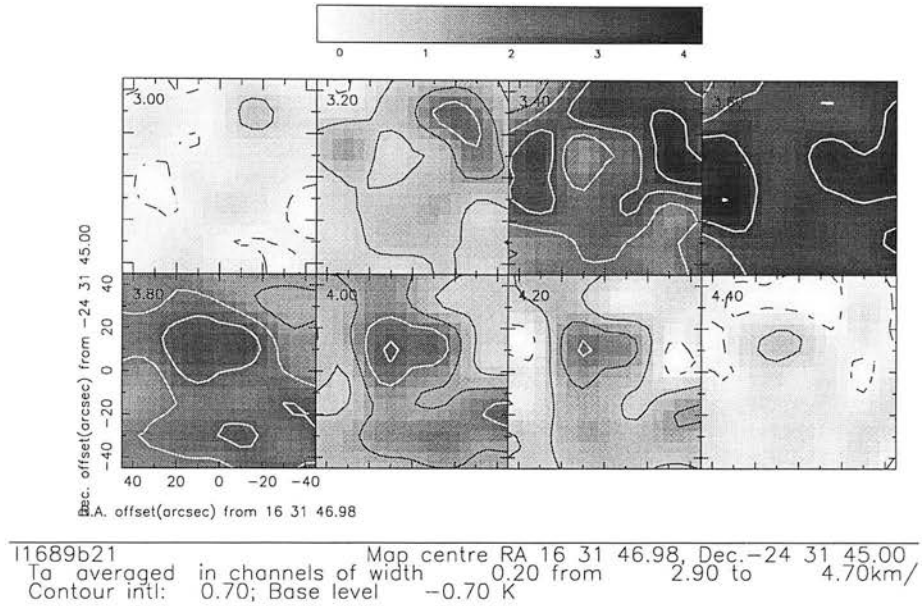

Figure 4.8: $C^{18}O$ (J=2→1) channel map of L1689b.

displacement which had 4 spectra, the average and standard deviation were calculated and are plotted as the intensity and error. Equation 4.3 and 4.5 were used to convert the measured T_a^* into T_{mb}.

The $C^{18}O$(J=2→1)T_{mb}(peak) varies between 5.0K and 6.0K, and the $C^{18}O$(J=3→2) T_{mb}(peak) varies between 3.8K and 4.8K. This range in intensities is little more than the relative calibration errors (see Figure 4.2 and discussion in text or error bars on equations 4.3 and 4.5). Hence one can summarise the $C^{18}O$ observations of L1689B as having 3 main properties:

- The $C^{18}O$(J=2→1) T_{mb}(peak) at the centre is 5.5K.
- The $C^{18}O$(J=2→1)(32") / $C^{18}O$(J=2→1)(central) ratio = 1.0 ± 0.1.
- The $C^{18}O$(J=3→2)(central)/ $C^{18}O$(J=2→1)(central) ratio = 0.78 ± 0.09.

These values are obtained from Figure 4.9 which gives more reliable results than the grey scale, contour maps produced by SPECX. These measurements on their own can be used to put strong constraints on the model of L1689B presented in the next chapter. L1689B was also mapped in $C^{18}O$(J=2→1). The hyper fine splitting of the line was resolved but the signal to noise obtained was not high enough for a $C^{18}O$(J=2→1 to trace any significant structure in L1689B.

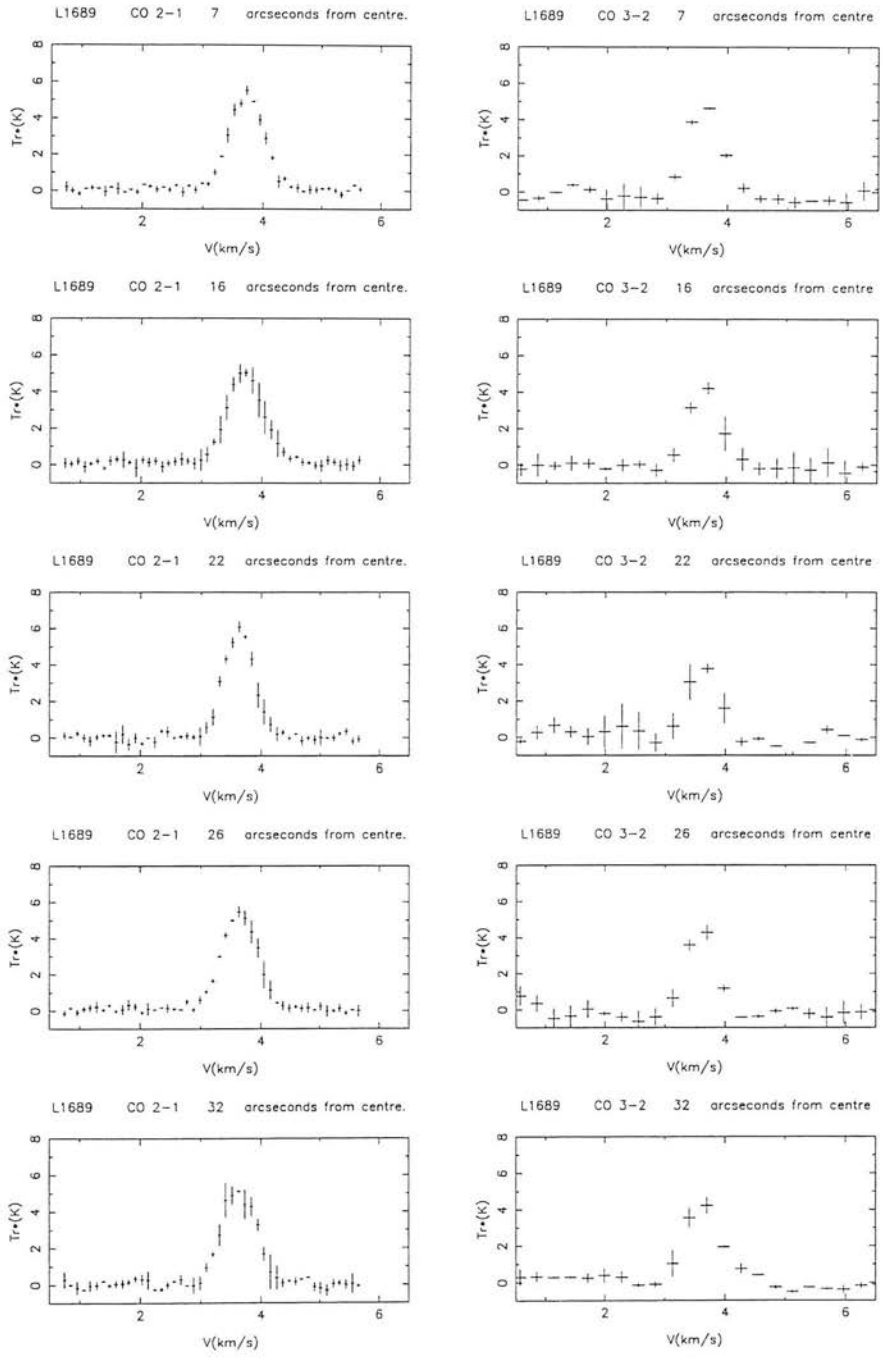

Figure 4.9: Azimuthally binned spectra of L1689B.

4.7 Conclusions

High resolution maps and observations of molecular cloud cores obtained at the JCMT have been presented. A detailed analysis of the calibration of the observations was described. $C^{18}O(J=2\rightarrow1)$ was detected in 5 out of 5 cores and $(J=3\rightarrow2)$ was detected in 3 out of 9. Maps made of the central 20 to 50 arcseconds of 4 cores shows that on these scales the cores have a relatively constant $C^{18}O$ surface brightness. Although there is little evidence for internal structure on these scales, the intensities measured and the surface brightness gradients, are measurements which can be used to put limits on the models of the cores. For the brightest core, L1689B, and the one which seemed to show most evidence of spherical symmetry and of intensity variation, these values were measured by azimuthally binning the spectra. Three key parameters were derived for this core (which will be used in the next chapter to constrain physical models): the $T(J=2\rightarrow1)$ brightness; the ratio of the $T(J=3\rightarrow2)/T(J=2\rightarrow1)$; and the brightness gradient measured moving away from the core centre. In the next chapter a detailed radiative transfer model of L1689B will be described, and the physical parameters of the core will be derived.

Chapter 5

Modelling Prestellar Cores.

5.1 Introduction

In the previous chapter maps were presented of a few starless molecular cloud cores in various isotopomeric transitions of CO. In this chapter detailed modelling of the submillimetre emission observed from the brightest of these cores, L1689B, is presented. For simplicity the chosen model assumes spherical symmetry and functional forms of the density, temperature and abundance profiles of the tracers. As was stated in the introduction magnetic support models are intrinsically asymmetric; MHD turbulence can produce elongation along field lines and therefore is expected to produce prolate structures, while ambipolar diffusion supports clouds perpendicular to the field lines, and therefore produces oblate structures. Any conclusions reached in this chapter are therefore limited by the assumption of spherical symmetry if magnetic fields play an important role. The aim, bearing in mind these limitations, is to constrain the physical characteristics of L1689B and to attempt to predict its future evolution. The surface brightness gradient of L1689B, the absolute brightness of $C^{18}O(J=2\rightarrow1)$ and the ratio of $C^{18}O(J=3\rightarrow2)$ brightness to $C^{18}O(J=2\rightarrow1)$ have been measured in chapter 4. These properties alone will prove capable of constraining the model.

The model presented has been parameterised in such a way that I can test amongst others; the model suggested by Andre et al (1996), the theoretical models suggested by Shu (1987) and Mouschovias (1991), as well as investigating the isothermal assumptions inherent in all these models. First the emission expected in the millimetre continuum is derived, and compared to measurements made at 1.3mm of L1689B by Andre et al (1996). A description of a numerical code (the Stenholm code) which can solve

the radiative transfer of millimetre line emission is then presented. An investigation is then made into how the measured parameters for L1689B are dependent on the free parameters in my model, and hence what restrictions the $C^{18}O$ observations of chapter 4 put on L1689B's structure. Combining both sets of results (the continuum and molecular line observations) I present two models of L1689B which seem consistent with both sets of observations, and can only be distinguished given a detailed understanding of molecule/dust interactions. The modelling rules out the isothermal singular model suggested by Shu (1987), but the models suggested both by Andre et al (1996) and Mouschovias (1991), are acceptable. The gas phase abundance of the $C^{18}O$ seems to fall towards the centre of the core, as might the temperature. Finally an analysis of the forces acting on the core is presented and discussed. It is argued that L1689B has little or no pressure support within its central regions and is highly unstable to gravitational collapse. This strongly implies the need for another support mechanism, the most likely of which is magnetic.

5.1.1 A Simple Model of L1689B.

Theoretical models of prestellar cores are available but are widely varying in their predictions of the structure of the cores. Some models predict a $\rho \propto r^{-2}$ density profile throughout the core - a so called 'singular' core (Shu et al 1987), while other works studying the stability of spheres in hydrostatic evolution (Bonnor 1956) or supported by magnetic fields (Mouschovias 1991) show more flattened inner density profiles. The wide range of models creates difficulties if one wishes to compare the models with detailed observations in a systematic way, or determine unique observational characteristics of each model. Therefore I have chosen a model which allows certain key physical processes and characteristics (specifically flattening of the inner density profile, falling of temperature, and falling CO abundances) to be represented in terms of simple analytical functions, and which at the same time incorporates either exactly (ie the isothermal singular sphere) or qualitatively (the magnetically supported models) the various physical models suggested. In this way by exploring how the observed appearance of L1689B is dependent on certain aspects of the model one can hope to find out which of the theoretical models of prestellar evolution best describes the observations of L1689B.

The model L1689B is assumed to consist of an isothermal envelope of radius 0.07pc with an inner core of radius 0.02pc as suggested by Andre et al (1996). This is the radius at which a break in the power law density profile is observed in the continuum data, a radius which I will also refer to as the critical radius. To ensure that the profiles stayed finite I also set an inner radius of the core equal to 0.004pc - well within the resolving power of the JCMT or IRAM.

The envelope outside of the critical radius has a constant temperature, a density profile $\rho \propto r^{-2}$, and

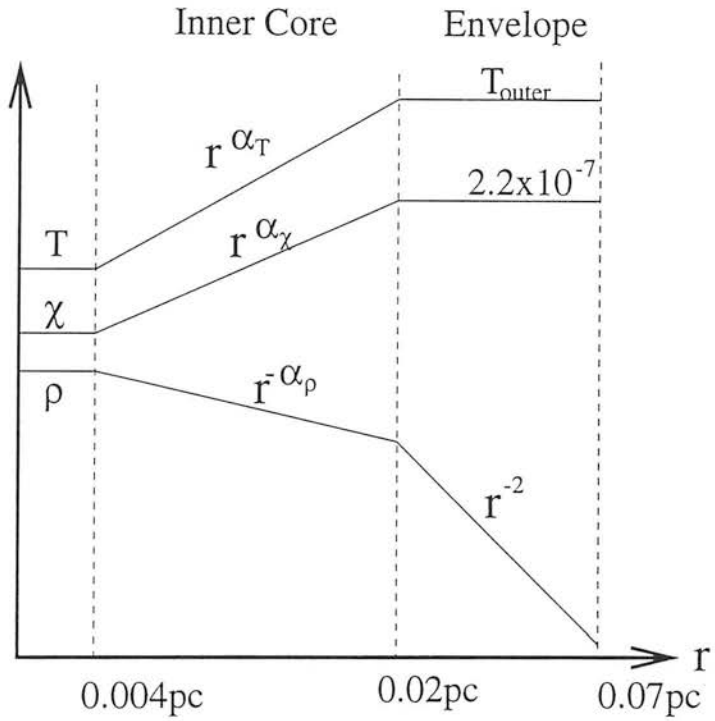

Figure 5.1: The model core for L1689B is based on that suggested by Andre et al (1996). The core has an outer envelope with a density profile which falls as r^{-2}. The outer envelope is isothermal and is assumed to have the CO abundance typical of the Ophiuchus cloud. An inner core region can have a more flattened density profile as suggested by the continuum observations, and consistent with theoretical models of cores like those suggested by Mouschovias (1991) and Bonnor (1956). The inner core is not assumed to be isothermal, and the CO abundance can also fall. In order to keep all parameters finite, the core has an inner radius of 0.004pc, well below any current single dish millimetre telescope's resolution, within which all physical conditions are homogeneous.

χ the $C^{18}O$ to H_2, ratio is assumed to be 2.1×10^{-7} (using a value of $C^{16}O$ to H_2 of 9.5×10^{-5} and a ratio of $C^{18}O$ to $C^{16}O$ of 1:450 (Wild 1990)). The inner core has a density profile, a temperature profile and an abundance profile of carbon monoxide, all of which are described by power laws; $r^{-\alpha_\rho}$,r^{α_T}, and r^{α_χ} respectively. Hence there are 5 free parameters in the model: the central density; the central temperature; and the value of the three indexes in the power laws, $\rho(r) \propto r^{-\alpha_\rho}$, $T(r) \propto r^{\alpha_T}$, and $\chi(r) \propto r^{\alpha_\chi}$. The model is illustrated in Figure 5.1.

5.2 The Millimetre Continuum Appearance of L1689B.

I first start by modelling the submillimetre continuum emission of L1689B. At these wavelengths the emission is optically thin (Andre et al 1996) and scattering is not significant because the wavelength of the radiation is much larger than the grain sizes (Hildebrand 1983). By assuming for the moment that the grain abundances and properties are constant throughout the core (two properties of L1689B that may not hold, as is discussed later) one can present the following analysis:

The millimetre continuum arises due to dust grains emitting thermally (Hildebrand, 1983). In this situation the source function is given by:

$$S_\nu = B_\nu(T) \tag{5.1}$$

and the opacity is given by (cf equation 3.10):

$$\kappa_\nu = \pi n_g \langle a \rangle^2 Q(\nu)$$

where n_g is the number density of dust particles, $Q(\nu)$ is the average emissivity of the dust grains and $\langle a \rangle$ is the average dust grain radius. At 1.3 mm, $(h\nu/k) = 0.5K$, which is well below the expected temperature of the dust within the core, so that the Rayleigh Jeans approximation can be used for the Source Function; $S_\nu = 2k\nu^2T/c^2$. Hence if the dust properties are constant throughout the cloud (ie constant grain size distribution, abundance with respect to H_2 and emissivity) then the intensity arising from an element of length dx at a given frequency is,

$$dI(x) \propto \rho(x)T(x)dx, \tag{5.2}$$

where $\rho(x)$ is the density profile along the line of sight and T(x) is the temperature profile of the dust along the line of sight.

If one is dealing with a spherically symmetric system (like the model of L1689B presented here) then one can ask what will be the projected surface brightness along a line of sight which at its closest point passes a distance R from the centre of the cloud of radius R_c:

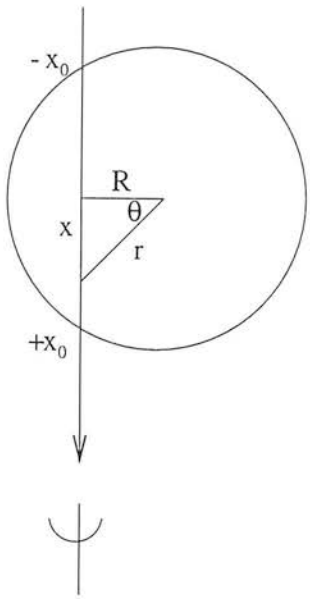

If the density profile $\rho(r)$ and the temperature profile T(r) are known, where r is the radial distance from the cloud centre, then the observed surface brightness I(R) is given by the equation of radiative transfer (2.2) which becomes,

$$I(R) \propto \int_{-x_0}^{+x_0} \rho(r)T(r)dx. \tag{5.3}$$

Making the substitutions $R = \cos\theta r$ and $dx = d\theta R/\cos^2\theta$ one derives:

$$I(R) \propto R \int_{-\arccos(R/R_c)}^{\arccos(R/R_c)} \rho(R/\cos\theta)\ T(R/\cos\theta)\frac{d\theta}{\cos^2\theta}. \tag{5.4}$$

For the model of L1689B presented here, the density profiles and temperature profiles are both represented by power laws $\rho \propto r^{-\alpha_\rho}$ and $T \propto r^{\alpha_T}$ so that the equation approaches the solution,

$$I(R) \propto R^{(1-\alpha_\rho+\alpha_T)} \int_{-\pi/2}^{\pi/2} (\cos\theta)^{(-2-\alpha_\rho+\alpha_T)} d\theta. \tag{5.5}$$

as the radius of the core becomes infinite.

The integral on the right hand side is independent of R and therefore, $I(R) \propto R^{(1-\alpha_\rho+\alpha_T)}$ (see Andre et al 1996) for an infinite core.

Because in the model of L1689B both the density and temperature profiles are described by power laws and the emission is proportional to both it makes sense to simplify equation 5.5 by defining $\alpha_\epsilon = \alpha_\rho - \alpha_T$ so that one gets a simple description of the brightness profile $I(R) \propto R^{(1-\alpha_\epsilon)}$. In the case of the model of L1689B presented here for $r > r_{crit}$: $\alpha_\rho = 2$ and $\alpha_T = 0$ in the envelope so that one expects $I(R) \propto R^{-1}$ in the envelope as is observed in the continuum by Andre et al (1996).

For the inner core the equation for the projected surface brightness (equation 5.4) becomes:

$$I(R) \propto \frac{2}{r}\left(\frac{\pi}{2} - \arccos(r) + r^{(2-\alpha_\epsilon)}\int_0^{\arccos(r)} \cos^{\alpha_\epsilon - 2} d\theta\right) \tag{5.6}$$

where $r = R/r_{crit}$.

I have evaluated this for several values of α_ϵ ranging between 0.4 and 1.4 and the results are presented in Figure 5.2. The continuum surface brightness distribution suggested by Andre et al (1996) for this region is plotted as a set of data points. Andre et al (1996) found a best fit for the surface brightness was a power law $I(R) \propto r^{-0.3\pm0.2}$, after taking into account the effects of the beam size and the observational procedure. The data points in Figure 5.2 represent the value of this fit at every 4 arcseconds, the sampling used by Andre et al (1996).

On examination it can be seen that the value of α_ϵ is roughly 0.4-0.6 which is considerably different from the value stated by Andre et al (1996) who derived $\alpha_\epsilon = 1.3$. The difference is due to the fact that a considerable proportion of the intensity emitted comes from the outer core even when looking at lines of sight passing through the inner cores (Andre et al 1996 applied the equivalent of equation 5.5 to the inner region rather than the more exact equation 5.6 and overestimated α_ϵ). Values for α_ϵ of even less than 0.4 could be acceptable.

The continuum data alone constrains the model of L1689B. Assuming that the fractional abundance of the dust is constant throughout the core then the value of α_ρ-α_T is approximately 0.4-0.6 and clearly inconsistent with the isothermal singular sphere model. The next few sections examine what limits the molecular observations can add to the model of L1689B.

5.2.1 The Stenholm Iterative Code.

I obtained a well used and tested code referred to as the Stenholm code from the University of Kent (Heaton et al 1993). The following section briefly summarises how the code iteratively solves the population levels (see also the thesis of Buckley 1997).

The code models a spherically symmetric cloud or core as a set of shells with uniform physical conditions. For each shell it requires the H_2 density, the H_2 temperature, the abundance of the radiating molecule (eg $C^{18}O$) with respect to H_2:- χ, and the bulk motion of the shell with respect to the core centre. Because molecular line widths are generally greater than predicted from simple thermal line broadening a microturbulent component of velocity δV is also specified for each shell.

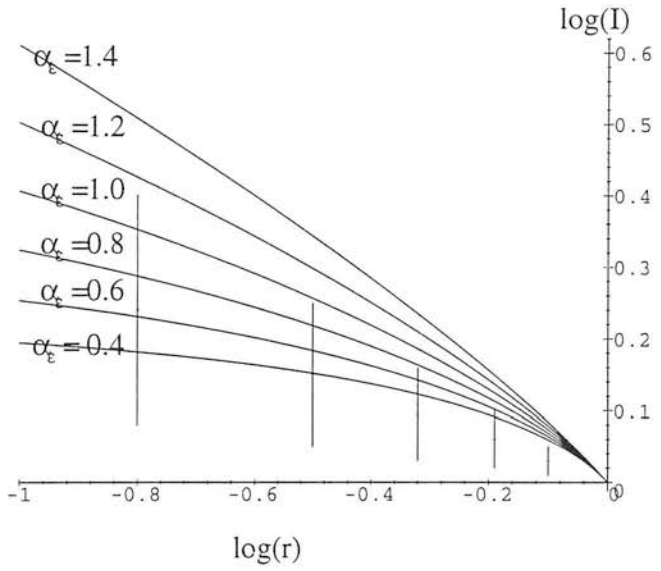

Figure 5.2: Expected projected intensity profile of L1689B for different inner core profiles. The points measured by Andre et al (1996) are marked with vertical error bars. From the graph it appears that $\alpha_\epsilon = \alpha_\rho + \alpha_T = 0.4$.

The code starts by choosing population levels which are consistent with the Boltzmann distribution (equation 2.15) at the H_2 temperature. The equation of radiative transfer is then numerically solved to get I_ν in each shell. Using this radiation field the rate equation (equation 2.20) is then solved to give a new set of population levels. The equation of radiative transfer is solved using this new set of level populations and the procedure of calculating n_j (the population levels of the molecules) followed by I_ν (the radiation field) is continued until a stable solution is approached. The exact method by which the Stenholm code approaches a stable solution is known as Lambda Iteration (see Buckley 1997), and throughout the work presented, a stable solution was taken when the population levels changed by less than 0.1 percent from one iteration to the next. The modelling presented of the core generally had low optical depths which meant that both the exact method of iteration and the convergence criteria were not as important as they are when one studies extremely optically thick species (the number of iterations to get to a final solution, in this work, is small $\sim 2-10$). Once final population levels are obtained the code can then solve the radiative transfer equation for lines of sight through the core and simulate observed line profiles by smoothing with a Gaussian spatial profile similar to a telescope beam profile.

The H_2 collision rates for the model were obtained from Flower and Launey (1985). They calculated the collision rates with para H_2 up to the J = 11 rotational level for temperatures between 10 and 250K and for ortho H_2 up to the J = 6 level between 10 and 100K. In order to extend my ability to examine how the radiative transfer was dependent on the ortho:para ratio collision rates appropriate for an ortho to para ratio of 1:1 were produced by averaging the two set, these are presented in Table 5.1.

Throughout the simulations (unless otherwise stated) the model core representing L1689B had the following properties: The model core consisted of 20 logarithmically spaced shells (giving increased resolution towards the centre of the core) of radii 0.004, 0.0047, 0.0055, 0.0064, 0.0074, 0.0086, 0.0100, 0.0116, 0.0135, 0.0156, 0.0181, 0.0211, 0.0245, 0.0285, 0.0331, 0.0384, 0.0447, 0.0519, 0.0603, 0.0700 parsecs and a critical radius $r_{crit} = 0.02$pc marking the boundary between the inner core and envelope. The velocity of the shells was set to zero. The microturbulence velocity component for each shell throughout the cloud was given by $\delta v(r) \propto r^{0.3}$ rising to 0.8km/s at the outside. This was chosen to be consistent with Larsons law (Larson 1984) who found a similar relationship for a wide range of clouds, and to fit the observed line widths. Although values of $\delta v(r) \propto r^{0.5}$ might be preferred (Myers 1983), it is shown later that the exact form of this microturbulent profile does not significantly alter the results. The ortho to para ratio of H_2 was held at 1 to 1. The other parameters were taken from the model of L1689B discussed earlier.

A representation of the code's results are shown for a fit to L1689B where $\alpha_\rho = -0.6$,$\alpha_T = 0.6$ and $\alpha_\chi = 0.6$, is given in Figure 5.3. For simplification the microturbulence profile is constant in this example throughout the core.

J	J′	10K	20K	40K	60K	100K
1	0	3.9E-11	3.4E-11	3.9E-11	4.5E-11	5.4E-11
2	0	5.6E-11	5.6E-11	5.6E-11	5.6E-11	5.6E-11
3	0	4.0E-12	4.8E-12	5.8E-12	6.4E-12	7.4E-12
4	0	7.4E-12	7.8E-12	8.3E-12	8.6E-12	8.9E-12
5	0	1.1E-12	1.3E-12	1.6E-12	1.9E-12	2.4E-12
6	0	1.0E-12	1.2E-12	1.5E-12	1.7E-12	2.0E-12
2	1	4.7E-11	5.0E-11	5.8E-11	6.6E-11	7.8E-11
3	1	8.6E-11	8.8E-11	9.0E-11	9.2E-11	8.8E-11
4	1	7.4E-12	1.0E-12	1.3E-11	1.4E-11	1.6E-11
5	1	1.3E-11	1.3E-11	1.4E-11	1.6E-11	1.6E-11
6	1	2.1E-12	2.6E-12	3.5E-12	4.2E-12	5.5E-12
3	2	3.8E-11	5.0E-11	6.5E-11	7.4E-11	8.6E-11
4	2	9.2E-11	1.0E-10	1.0E-10	1.0E-10	1.0E-10
5	2	7.5E-12	9.8E-12	1.4E-11	1.6E-11	2.0E-11
6	2	1.6E-11	1.6E-11	1.8E-11	2.0E-11	2.1E-11
4	3	3.9E-11	5.2E-11	6.8E-11	7.8E-11	9.0E-11
5	3	1.1E-10	1.1E-10	1.1E-10	1.1E-10	1.1E-10
6	3	1.0E-11	1.2E-11	1.8E-11	2.1E-11	2.6E-11
5	4	3.5E-11	4.8E-11	6.8E-11	8.2E-11	9.9E-11
6	4	1.2E-10	1.2E-10	1.3E-10	1.3E-10	1.2E-10
6	5	4.2E-11	5.2E-11	6.9E-11	8.1E-11	9.7E-11

Table 5.1: Collision rates between H_2 and CO for an ortho to para mix of 1 to 1.

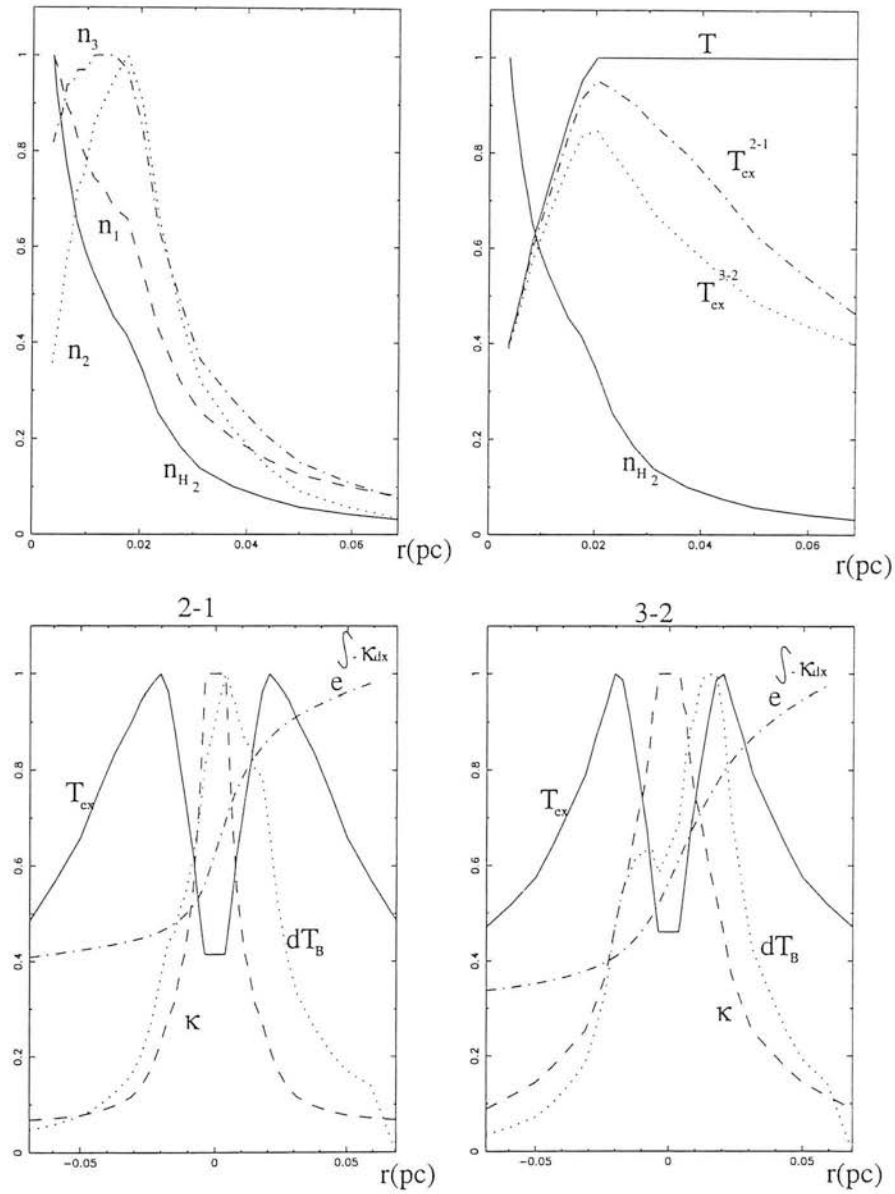

Figure 5.3: Explanatory plot of the radiative transfer, and line strengths. All the line plots are normalised so that the maximum value is equal to 1 in order to avoid over confusing the plot. The dotted lines in the bottom two plots show what fraction of the observed emission comes from each radius.

In the first plot the number densities of H_2, $C^{18}O(J = 1)$, $C^{18}O(J = 2)$ and $C^{18}O(J = 3)$ are shown as n_{H_2}, n_1, n_2, n_3 respectively. In the next plot the H_2 temperature, the $T_{ex}(J{=}2{\rightarrow}1)$, and the $T_{ex}(J{=}3{\rightarrow}2)$ are presented. The excitation temperatures are calculated from the population levels according to equation 2.15. The excitation temperatures are less than the kinetic hydrogen temperature because of the non-LTE state of the shells. The third and fourth plots concern the $(J{=}2{\rightarrow}1)$ and $(J{=}3{\rightarrow}2)$ brightness towards the centre of L1689B. Each shows the opacity per unit length, $\rho\kappa_\nu$, the transmission fraction, $\exp\left(-\int_0^r \rho\kappa_\nu dx\right)$, towards the observer from each shell, the excitation temperature and the brightness temperature per unit length observed from each shell, which is given by the equation:

$$\delta T_B(r) \propto T_{ex}\rho\kappa_\nu \exp\left(-\int_0^r \rho\kappa_\nu dx\right), \tag{5.7}$$

and plotted as a dotted line in each plot. The line shows where in the core the observed emission originates from. One can see that the emission is asymmetric - ie more of the observed line intensity originates from the near side of the cloud than the far side- as would be expected.

I developed a perl script that allowed multiple simulations to be run. The script fitted the specified $C^{18}O(J{=}2{\rightarrow}1)$ central brightness by changing the central density of the core, increasing the density if the predicted intensity was too low, decreasing the density if it was too high and iterating until the specified intensity was achieved. This normalised the results to fit the observed $C^{18}O(J{=}2{\rightarrow}1)$ brightness. The following sections investigate the effect of varying 4 of the free parameters in the model core, α_T, α_ρ, α_χ, and T_{outer}, (ρ_c, the central density and the fifth free parameter in the model of L1689B is set by normalising the simulations to reproduce the central brightness of the core).

5.3 Results of Molecular Radiative Transfer

5.3.1 Is L1689B Isothermal?

The simplest models of cloud cores assume isothermality. I investigated how the predicted appearance of L1689B is dependent on the density profile $\rho \propto r^{-\alpha_\rho}$ and the isothermal temperature T: within r_{crit} the shell densities were given by $\rho \propto r^{-\alpha_\rho}$.

The predicted appearance for the set of cores with temperatures between 14 and 24K and α_ρ between 0 and 2 was calculated and the values of the ratio of $J{=}3{\rightarrow}2$ to $J{=}2{\rightarrow}1$, the brightness gradient, the central density used to normalise the cores, and the optical depth are all plotted in Figure 5.4, as functions of α_ρ and T.

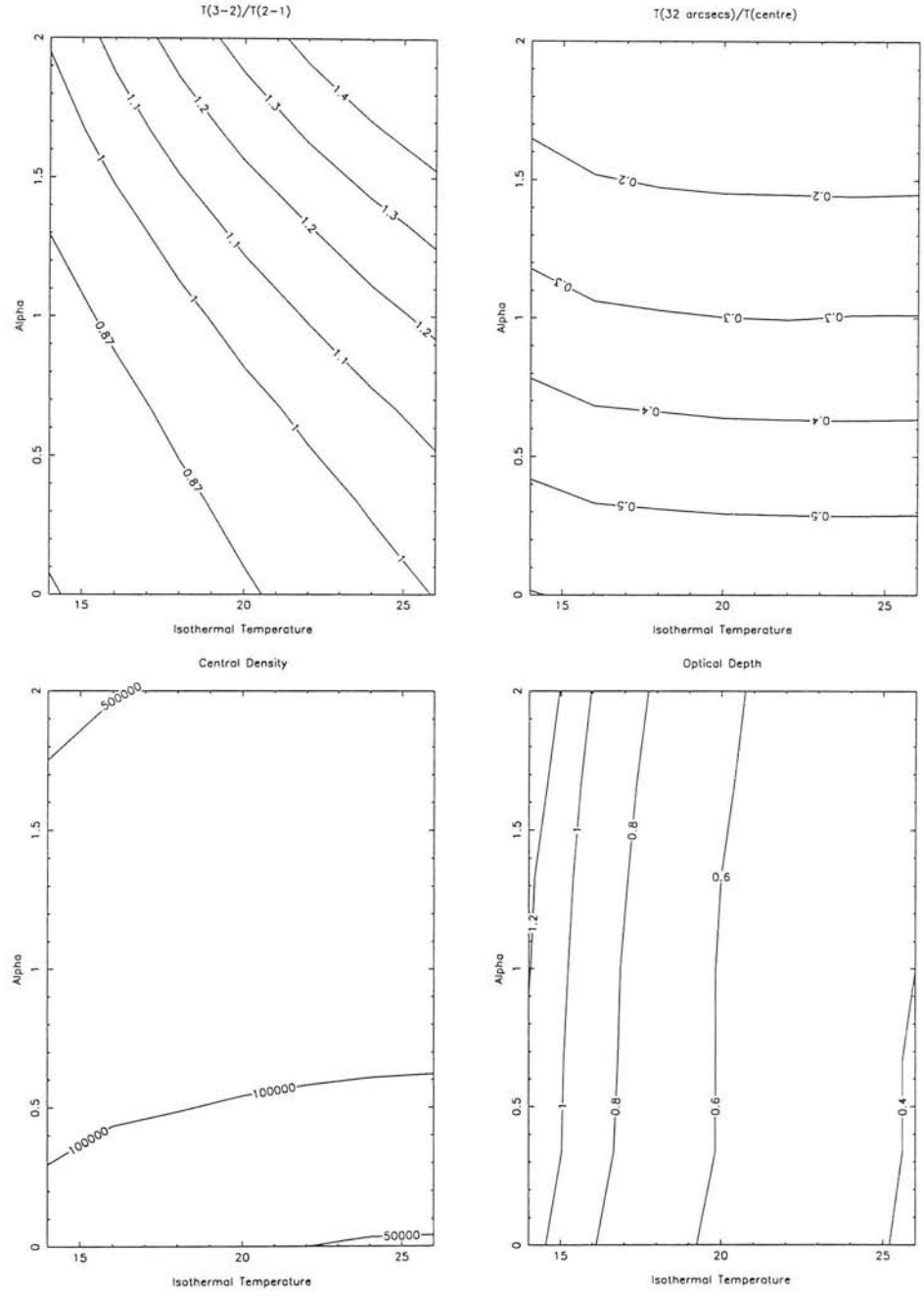

Figure 5.4: The predicted appearance of the set of isothermal cores (with T varying between 14 and 26K), and with the density profile $\rho \propto r^{-\alpha_\rho}$. The cooler cores with flat density profiles can predict the observed ratio of J=3→2 to J=2→1 observed in L1689B but none of the cores could predict the flat brightness gradient. The measured values of J=3→2 to J=2→1 is 0.67-0.87, and the value of T(32 arseconds)/T(centre) was 0.9-1.1.

The first graph shows that the J=3→2 to J=2→1 brightness ratio at the centre of the core varied between 0.67 and 1.57 increasing with both the temperature and the value of α_ρ, due to the upper levels becoming more populated as the temperature and density increases. As stated earlier the measured value of this ratio is 0.69-0.87 for L1689B. The second graph shows that the brightness gradient varied between 0.1 and 0.35 and increased mainly as the density profile of the cores flattened - this is due to the column density of material along the different lines of sight becoming more constant. Remember that the observed value in chapter 4 was 0.9-1.1

The isothermal models could produce the J=2→1 brightness seen towards the centre of L1689B, and the cooler and less centrally peaked models were capable of producing the observed ratio of J=3→2 to J=2→1 brightness ratio in L1689B. However none of the cores will reproduce the slow fall off of $C^{18}O$ surface brightness observed for L1689B. I can therefore rule out the simplest isothermal models of L1689B unless other factors such as abundance variations are also important (see below). The lower 2 plots show that the central density used fell as the density profile flattened, and the optical depth increased as the temperature dropped.

5.3.2 A Falling Temperature Towards the Centre of L1689B.

In order to investigate the effect a falling temperature profile would have on the appearance of the core the predicted appearance was calculated for a set of cores with $\rho \propto r^{-\alpha_\rho}$ inside the critical radius. The collision rates given by Flower and Launey (1985) did not extend below 10K giving a minimum temperature which can be investigated. The temperature profile was continuous at $r = R_{crit}$ and fell as $T \propto r^{\alpha_T}$ until the inner radius was reached or until the temperature fell to 10K.

The predicted appearance of the set of cores with α_T between 0 and 2 and α_ρ between 0 and 2 was calculated and the results are plotted for the set of cores with an outer temperature of 20K in Figure 5.5 and for the set of cores with an outer temperature of 25K in Figure 5.6. The central density needed to produce the observed J=2→1 brightness increased as the inner density profile steepens and the optical depth appears to increase both with a falling inner temperature and an increasing central density as shown in the lower plots.

The ratio of the J=3→2 to J=2→1 brightness predicted varied between 1.5 and 0.7. This ratio was strongly dependent on the lowest temperature in the core (NB when α_T is greater than approximately 0.6 the minimum temperature is held at 10K and the ratio is roughly constant). The simulations predicted that the brightness gradient observed would vary between 0.1 and 1.0 and fall both as the inner cores

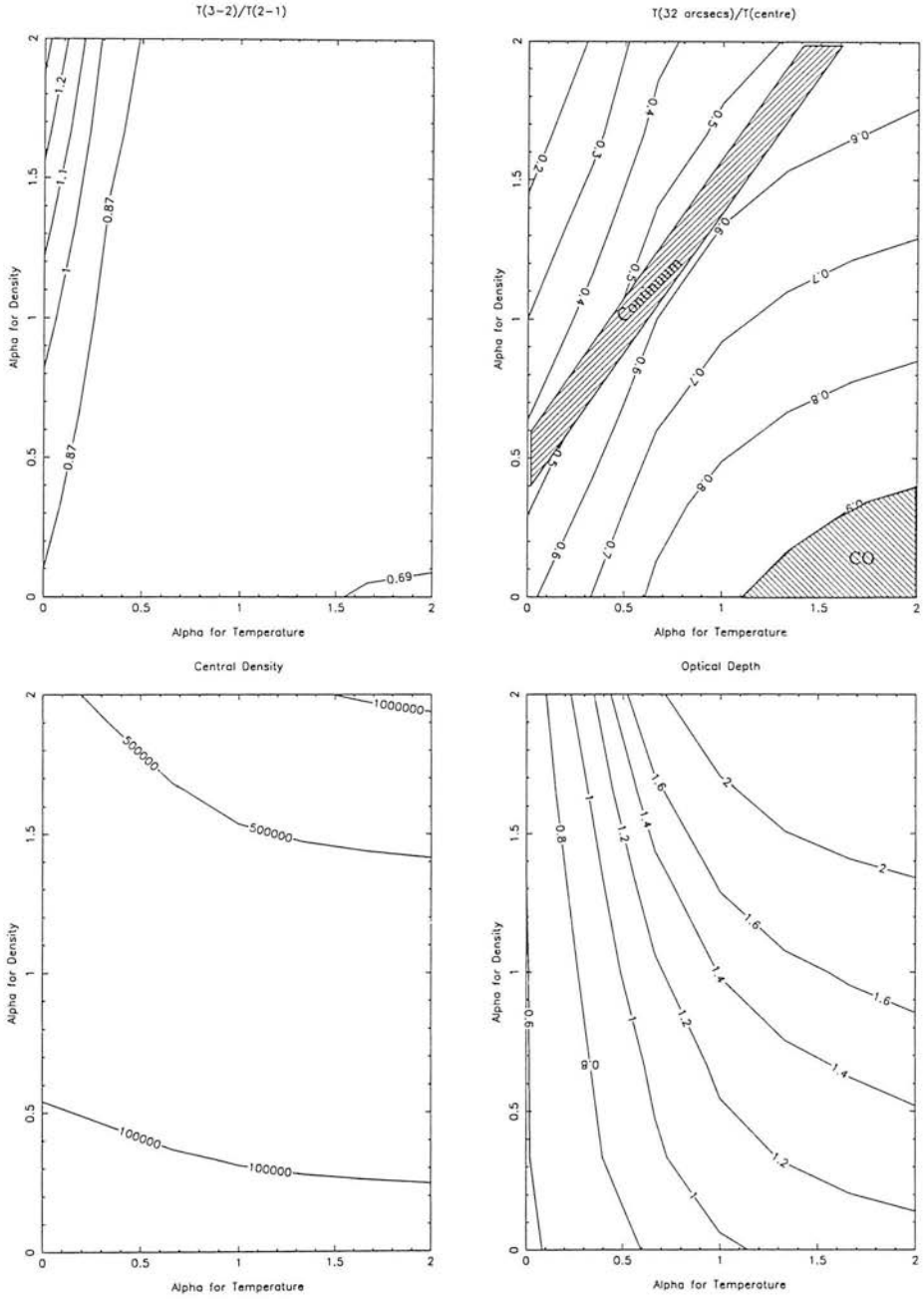

Figure 5.5: The predicted appearance of the set of cores with inner density profile given by $\rho \propto r^{-\alpha_\rho}$ and inner temperature profile $T \propto r^{\alpha_T}$. The outer T was 20K. The profiles which have a very flat density profile and a steep temperature drop can predict the appearance of L1689B.

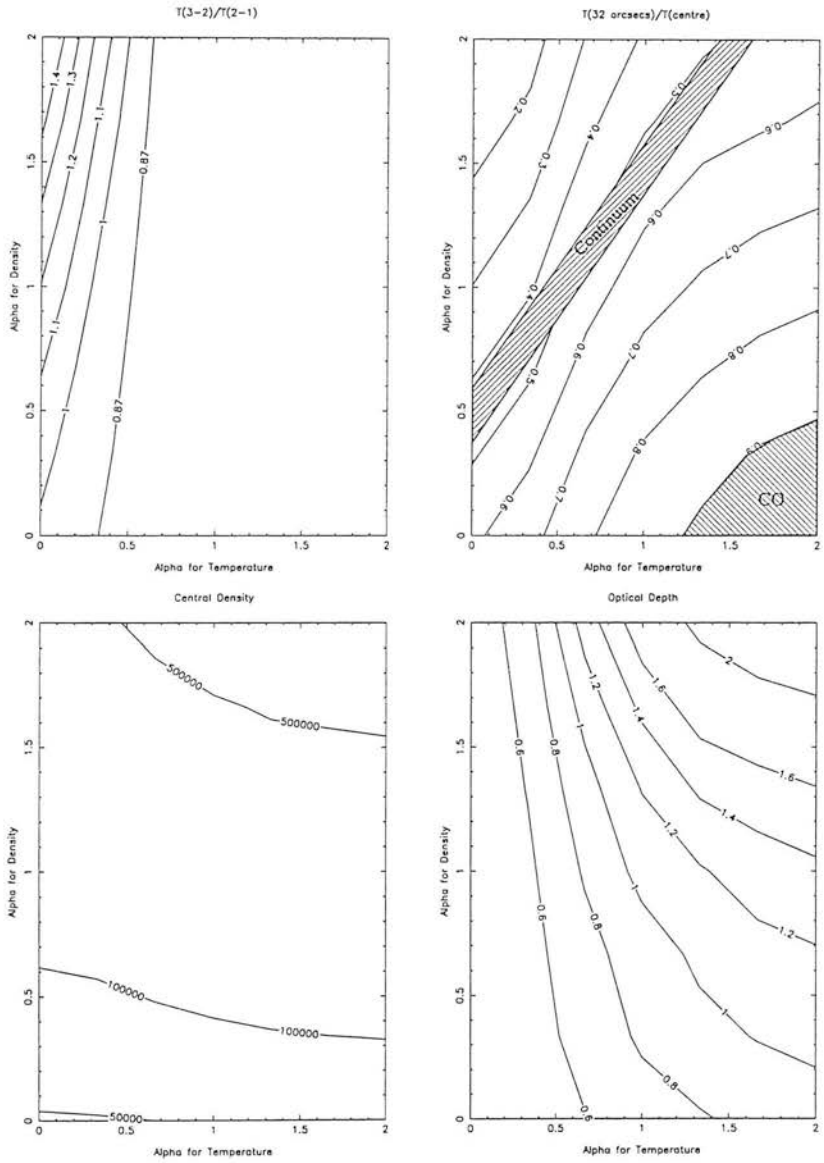

Figure 5.6: The same model as in figure 5.5 but with a warmer outer envelope (T=25K). The predicted ratio of J=3→2 to J=2→1 is slightly higher, while the optical depths and central densities are slightly lower.

density profile becomes flatter and as the rate at which the temperature falls increases. Increasing the outer temperature increased the ratio of J=3→2 to J=2→1 brightness but made little difference to the brightness gradients predicted. It also decreased the central densities required to produce the observed J=2→1 brightness and decreased the optical depth of the cloud.

A flat inner density profile and a very steep temperature drop can predict the observed appearance of L1689B. However the continuum fit, $\alpha_\rho - \alpha_T$=0.4-0.6 is shown as a hatched area in the plots, and clearly under predicts the ratio of T(32 arcseconds)/T(centre) by a factor of 2. Therefore a falling temperature can predict the molecular appearance alone , but is unable to predict both the continuum and molecular appearance of L1689B simultaneously.

5.3.3 Freezing Out of CO in the centre of L1689B

There are three main processes, which are thought to play a role in keeping the relatively volatile molecules like CO from freezing out onto dust grains Willacy et al 1994). Effective desorption mechanisms result in the volatile CO molecule remaining in the gas phase; although CO molecule is allowed to be absorbed onto a grain surface, it is expected to be rapidly ejected. The first ejection mechanism occurs when Cosmic Rays absorbed by a grain create hot spots where volatile molecules are ejected - known as cosmic-ray heating. The second ejection mechanism occurs because Cosmic Rays also ionize H_2 molecules, producing energetic electrons and excited H_2 molecules and a molecule destroying UV field. The dissociated products then heat the ices on the grains to the point of desorption - this process is known as Cosmic-ray-induced photodesorption. The third process occurs when an H_2 molecule is formed on a grain surface, the chemical reaction is exothermic, and local heating occurs, again producing desorption of volatile molecules.

As the density of a cloud gets larger, the CO abundance might fall due to the number of CO molecule/dust collisions increasing and the desorption becoming less frequent eg the ionization level falls so that the Cosmic-Ray-induced photodesorption process becomes less efficient and the number of hydrogen atoms also falls, reducing the rate of H_2 formation.

In order to investigate the effect of a dropping CO abundance on the appearance of L1689B the set of cores with an isothermal temperature, inner density gradient $\rho \propto r^{-\alpha_\rho}$, and CO abundance fraction $\chi \propto r^{-\alpha_\chi}$ was investigated within the region $0 < \alpha_\rho < 2$ and $0 < \alpha_\chi < 2$. The appearance of the cores was calculated and is presented in Figure 5.7 (for 20K) and Figure 5.8 (for 25K).

The central density needed to explain the central J=2→1 brightness varied between approximately

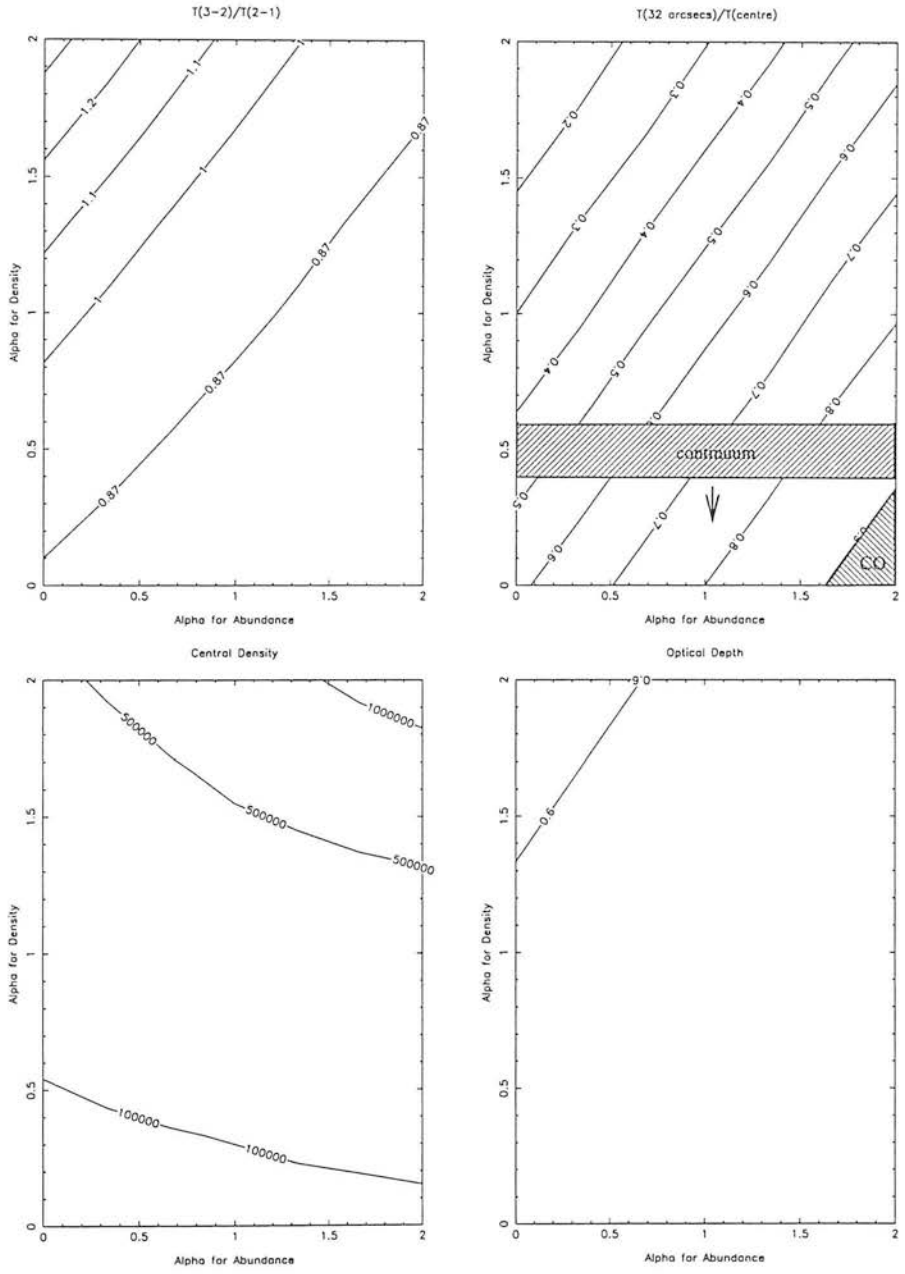

Figure 5.7: The predicted appearance of the set of isothermal cores with T=20K, $\rho \propto r^{-\alpha_\rho}$, and CO abundance fraction $\chi \propto r^{-\alpha_\chi}$. The profiles with a flat density profile and very sharp drop in CO abundance can predict the appearance of L1689B.

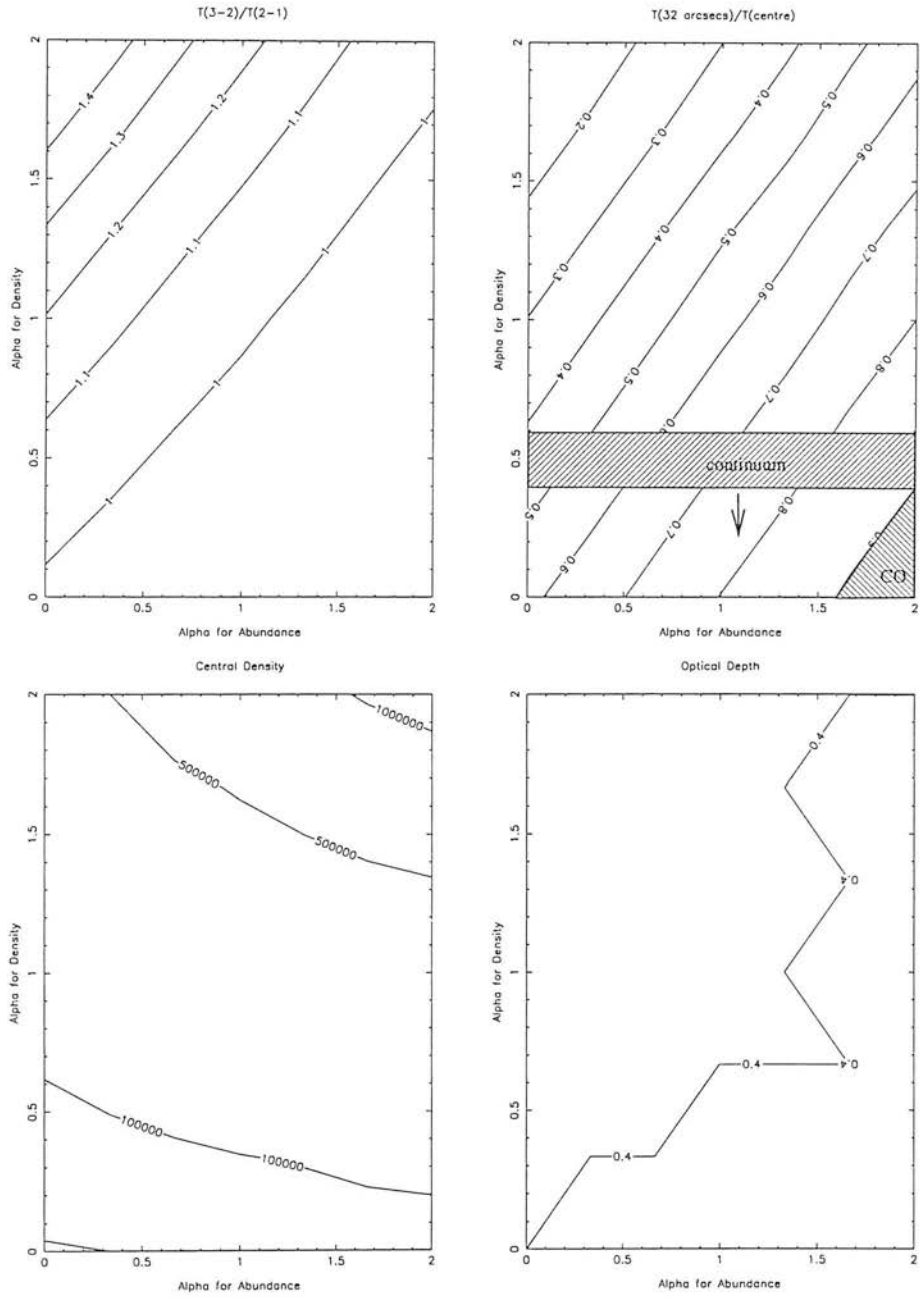

Figure 5.8: The same as figure 5.7 but with an envelope temperature of 25K. The increase in temperature increases the predicted ratio of J=3→2 to J=2→1, and decreases the required central densities and optical depths.

Table 5.2: Table summarising results of radiative transfer modelling.

Continuum models	Predict $\alpha_\rho - \alpha_T \sim 0.4 - 0.6$
Isothermal Molecular models $\alpha_\chi = 0$	Brightness gradient too steep.
Molecular models $\alpha_\rho = 0$, $\alpha_T = 2$, $\alpha_\chi = 0$	Predict L1689B's molecular appearance.
Isothermal Molecular models $\alpha_\rho = 0.5$, $\alpha_\chi = 2$	Predict both continuum and CO.

10^5 and 10^6 and fell as the density profile flattened. The optical depth towards the centre remained almost constant and was relatively independent of either the density or abundance profiles.

The ratio of the J=3→2 to J=2→1 brightness varied between approximately 0.7 and 1.5, falling as the density profile in the inner core flattened and as the abundance drop within the inner core steepened. The brightness gradient varied between 0.1 and 1.0 and increased as the density profile flattened and the abundance steepened. Increasing the temperature increased the ratio of J=3→2 to J=2→1, had little effect on the brightness profile, slightly decreased the central density needed to produce the observed $C^{18}O$(J=2→1) brightness and decreased the optical depth.

One can conclude that a flat density profile and a very steep abundance drop can predict the observed molecular appearance of L1689B. What is more, unlike the model with a pure temperature drop, the abundance drop can predict the continuum appearance at the same time.

5.4 Summary of Results.

The results of the modelling of the millimetre continuum emission and submillimetre spectral line emission presented so far are summarised in Table 5.2.

In the three dimensional parameter space defined by α_ρ, α_T, and α_χ, there is a region defined by α_ρ-α_T=0.4-0.6, which will predict the continuum observations. There is also a set of solutions in the parameter space which predict the molecular appearance- of which 2 points have been presented ie $(\alpha_\rho = 0, \alpha_T = 2, \alpha_\chi = 0)$ and $(\alpha_\rho = 0, \alpha_T = 0, \alpha_\chi = 2)$. They both independently rule out the isothermal singular sphere model, and taken together the continuum observations and the molecular observations seem to indicate a unique solution i.e. $(\alpha_\rho = 0.5, \alpha_T = 0, \alpha_\chi = 2)$. Taken in combination some part of the degeneracy is apparently lifted, and a unique or best fit model for L1689B seems to be obtained. However the conclusions now become dependent on the mechanism by which the molecular abundance falls and

the, influence that this has on the dust opacity and emissivity. The exact form of the molecular dust interactions become critically important. Before discussing this however I present several other minor factors which affect the modelling.

There are several other factors than the three discussed above which may change the conclusions of the modelling. It is worth fully discussing these before engaging in an attempt to find a unique or best fit model for L1689B.

The ortho to para ratio in these cores is not well defined. Because the ortho form of H_2 has a higher cross section for collisions with CO the ortho to para ratio will affect the conclusions drawn. In order to investigate this the first model presented (Figure 5.4) was rerun with purely para hydrogen. The results are plotted in Figure 5.9. Comparison with Figure 5.4 shows that decreasing the fraction of ortho H_2 increases the surface brightness gradient slightly, and increases the ratio of J=3→2 to J=2→1.

Likewise the precise form of the microturbulence profile will influence the appearance of the core. For example it was found that when using a constant δv microturbulence profile the brightness gradient decreased slightly (eg T(32 arcsec)/T(centre) increased by $\sim$ 0.1). However neither of these two factors affect the appearance of L1689B strongly enough to affect the conclusions drawn above.

However if one accepts the assumptions presented then it seems clear that simple isothermal models cannot predict the appearance of L1689B. As discussed above one may introduce freezing out of molecular material onto the dust grains - but how? The CO may freeze out onto the dust grains either as a result of a temperature drop or the UV field becoming blocked out (Willacy et al 1994, Ossenkopf and Henning 1994). This will lead to a change both in the molecular abundances, a change in the dust opacities and sizes, and an increased brightness gradient in the continuum (which will change the continuum fit in the manner shown by the arrows in Figure 5.7 and 5.8). Hence even though it is clear that CO depletion is necessary to explain the difference in continuum and molecular appearance of L1689B, a proper understanding of dust molecule interactions and their dependence on temperature will affect the conclusions of the modelling. Because the dust molecule interactions are so critical in determining a unique solution, I present two models illustrating two different scenarios.

The first considers a core with an equation of state in which the temperature falls with increasing density, and in which CO freeze out occurs because of the decrease in temperature. This model has $\alpha_\chi = \alpha_T = \alpha_\rho = 0.6$ and is hereafter referred to as model 1.

The second model is the unique solution presented in figure 5.8, with an abundance fall alone (which in this case might be attributable to UV light being blocked out, and grain mantles becoming stable, or

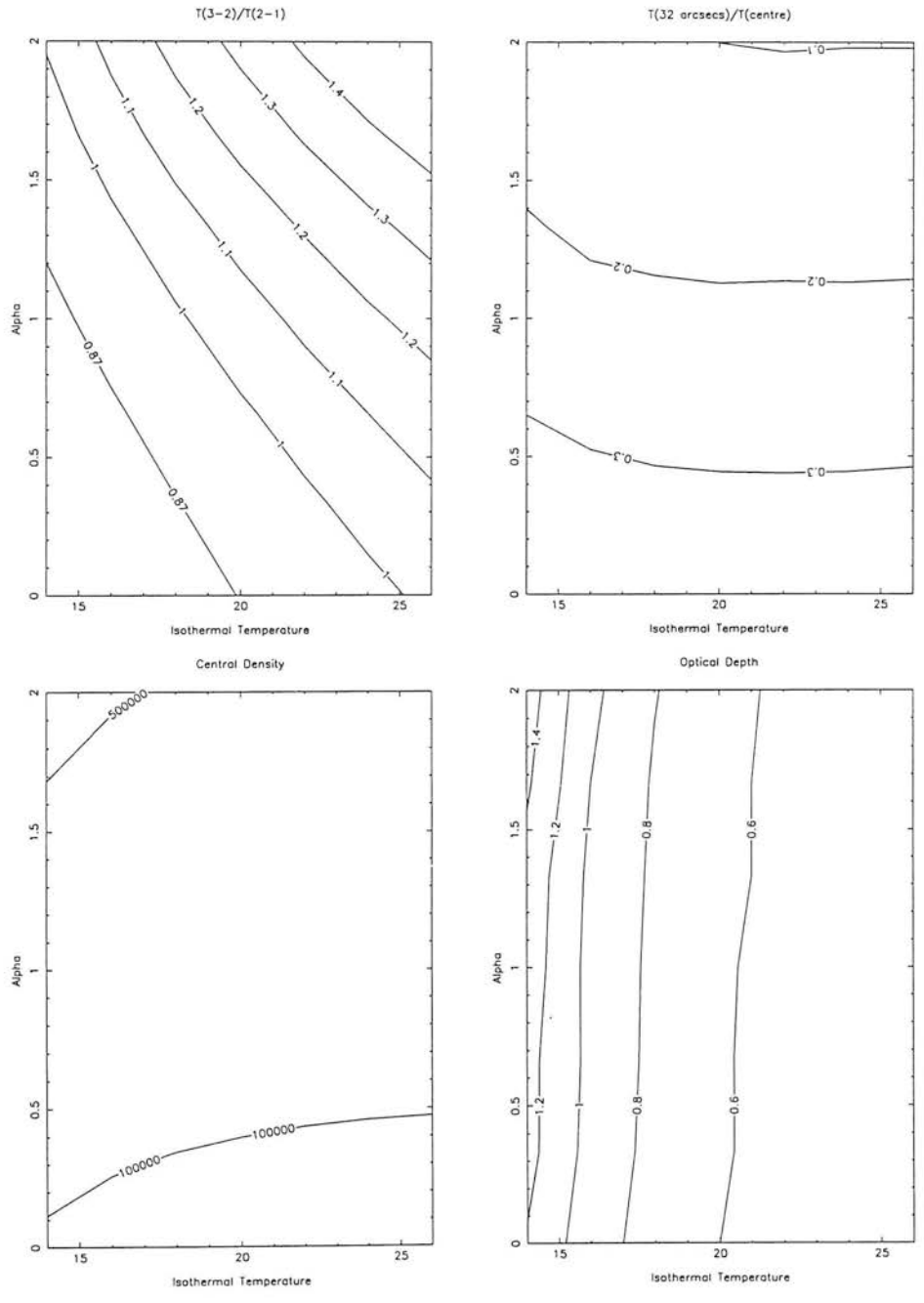

Figure 5.9: An isothermal core model with an inner density profile $\rho \propto r^{-\alpha}$, and purely para H_2.

chemical effects, or a long timescale associated with freezing out), is described by $\alpha_\chi = 2.0$, $\alpha_T = 0$, and $\alpha_\rho = 0.5$, and is hereafter referred to as model 2.

As was discussed in section 5.4.3, the simultaneous explanation of continuum and molecular appearance is mainly dependent on α_χ. Because the two models above have very different values, (one has α_χ =2.0, the other α_χ =0.6) they illustrate two different scenarios which might be distinguishable given a good understanding of dust/molecule interactions.

5.5 Two different Scenarios.

The predicted molecular appearance of the model where $\alpha_\rho = -0.6$,$\alpha_T = 0.6$ and $\alpha_\chi = 0.6$ is shown as a dotted line in figure 5.10. The predicted molecular appearance of the model with $\alpha_\chi = 2.0$, $\alpha_T = 0$, and $\alpha_\rho = 0.5$, model 2, is plotted as a solid line. The predicted spectra are plotted over the L1689B observations presented in chapter 4.

Both fits seem capable of explaining the molecular appearance, although model 1 under predicts slightly the intensity at the larger radii. If one considers the requirement from the continuum that $\alpha_\rho - \alpha_T \sim 0.4 - 0.6$ model 2 has $\alpha_\rho - \alpha_T = 0.5$, while model 1 has $\alpha_\rho - \alpha_T = 0.0$. This discrepancy however may be due to freezing out leading to an increase in grain opacity, κ_ν, due to both the build up of an icy mantle, and a change in grain size (Ossenkopf and Henning 1994) and model 1 may actually be better at explaining the continuum data.

The geometry of the core as a whole may change the exact form of the solutions found. In particular there are two main problems which should be considered - a break from spherical symmetry which is predicted in magnetically controlled collapse models, and a break from the homogeneous assumption - ie clumpiness within the core. Both are likely to affect the predicted appearance of the cores in millimetre observations. This is clearly beyond the scope of the work presented here, and therefore the fits are presented with the caveat that they are strongly dependent on the specifics of the dust/gas interactions within L1689B, and the geometry of the core.

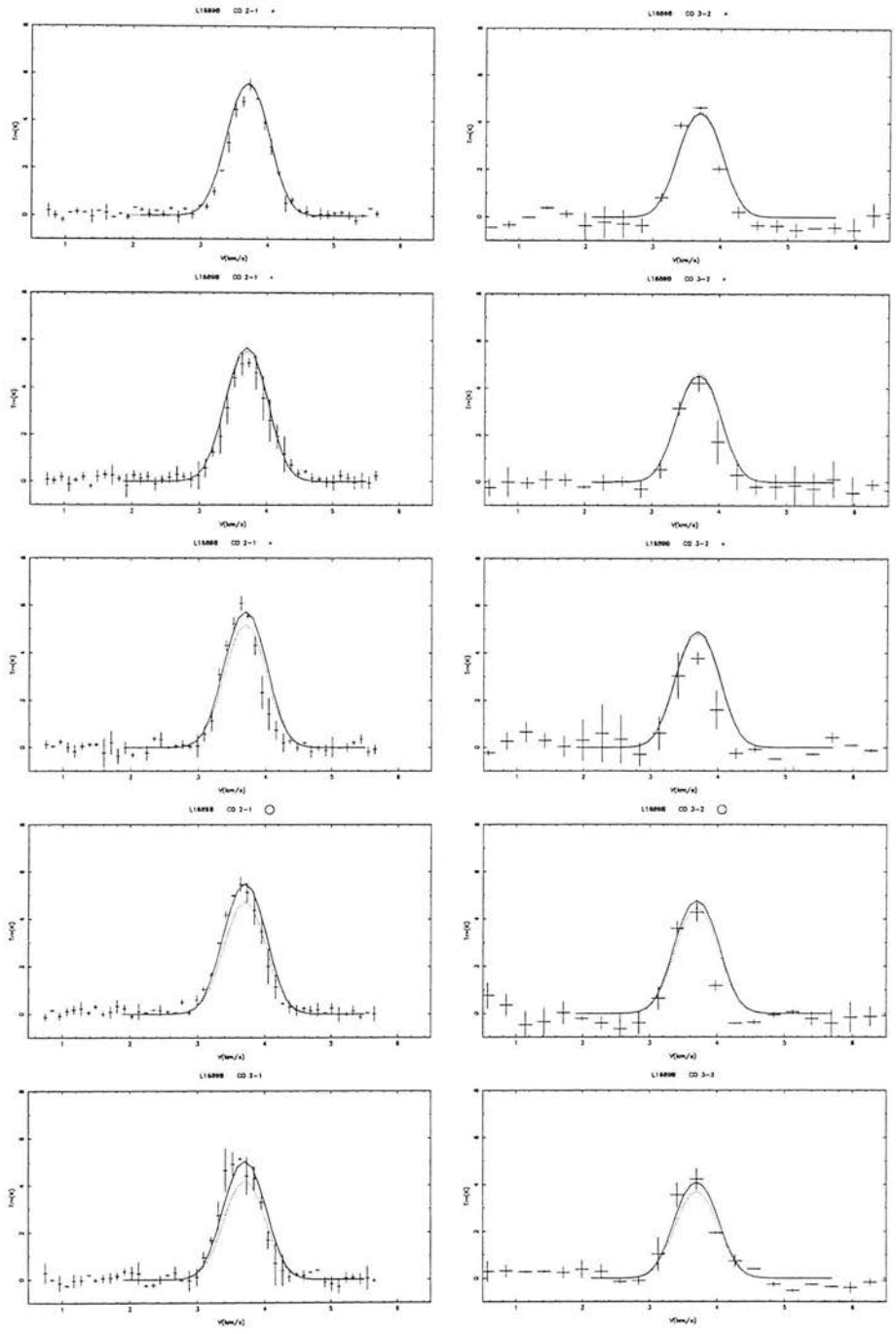

Figure 5.10: Azimuthally binned spectra of L1689B with two models shown. The dotted line shows a model where the temperature falls towards the centre of the core leading to freeze out of CO (model 1). The solid line illustrates a model where the CO abundance falls steeply (model 2).

5.6 Support Versus Gravity in L1689B: Is it Prestellar?

The temperature within the inner region of L1689B is roughly 20K in the two fits and the density within the inner cores is between 5×10^4 and $1.5\times10^5 cm^{-3}$. Similar fits can be found for lower temperatures and higher densities. These two values are highly dependent on each other, and a lower temperature will lead to higher inferred densities. Therefore the fact that the fits presented are slightly warmer and less dense than the model suggested by Andre et al (1996) is not thought to be significant (they are not unique and not presented as definitive cases). Only when the temperature of the whole core falls to 10K does the data start to constrain the model; the lines become extremely optically thick and flattened. The following section investigates how the temperature of L1689B will affect its future evolution.

The inner core is defined as the region within the critical radius (0.02 pc from the centre) and the envelope as the region outside the critical radius. The break in the density power laws occurs at the critical radius. The Jeans mass associated with a density and temperature similar to that in the inner core is $\sim 5M_\odot$. Although the inner core itself ($0.2M_\odot$) is not above this critical mass, the clump in which L1689B is embedded is thought to have a mass of $\sim 40M_\odot$ (Andre et al 1996). The free fall timescale of the inner core is $< 50{,}000$ years, which is very short compared to either the protostellar lifetimes, or the prestellar lifetimes inferred in Chapter 3. Therefore if L1689B is gravitationally unstable it is likely that some other form of support, most likely due to magnetic fields, is occurring within the inner core.

The future dynamical evolution of L1689B is dependent on the net forces acting on it. The gravitational force per unit mass is given by,

$$g = \frac{G\int 4\pi r^2 \rho(r) dr}{r^2} \tag{5.8}$$

and in both models is roughly proportional to $r^{0.5}$ in the inner core and r^{-1} in the outer envelope. The gravitational force therefore increases as one moves towards the centre in the envelope, but begins to decrease as one passes through the critical radius. It behaves in the same way for both models presented (NB: they only differ in their temperature, and abundance profiles, not in their density structures).

The pressure within the core is given by nkT and the force per unit mass due to pressure gradients is given by

$$\frac{1}{\rho}\frac{d}{dr}(nkT). \tag{5.9}$$

In both models this force falls as r^{-1} in the outer envelope, but behaves differently in the inner region. In model 1, because the temperature decreases as the density increases the pressure is roughly constant and there is no force due to pressure gradients at all. In model 2, the pressure force decreases away from the centre as r^{-1}. In model 1 the inner core is highly unstable to collapse but in model 2, the situation

is more complex.

However the situation is further complicated by the uncertainties in temperature. Figure 5.11 illustrates the behaviour of the two models at a high temperature and then at a lower temperature. In the high temperature case the gravitational force in the envelope is consistently larger than the force due to pressure gradients, in the lower temperature case the pressure force is consistently smaller than that due to gravity. The main difference between these two is due to temperature: a higher temperature increases the pressure and the pressure gradients but does not alter the gravitational field, and therefore cooler cores experience larger contracting forces.

The data presented in this chapter do not uniquely constrain the temperature. However given the lack of an internal heating source in L1689B, and in line with the previous work of Andre (1996), we favour lower temperature models (T <15K).

For both models 1 and 2 with envelopes of 20 K and average inner core density of $10^5 cm^{-3}$ the gravitational force just outside the critical radius is approximately one third that of the force due to pressure gradients. For similar models at 15 K the gravitational and pressure forces differ by a factor $\sim$ 1.5 and only for temperatures less $\sim$13 K is the gravitational force greater than the pressure force throughout the core. In addition a greater r_{crit} will also increase the ratio of gravitational force to pressure force in the envelope.

In model 2 there seems to be a problem because the inner region experiences a net outwards force whatever the envelope temperature. This is most likely to be due to the simple nature of the chosen density profile (ie two power laws) and probably only affects the very inner region. In reality this would relax on a very short timescale to a smoother density distribution and the region of outwards force would rapidly disappear as the core evolved towards hydrostatic equilibrium (eg a Bonnor-Ebert sphere).

I now consider what will happen dynamically to L1689B in the two model cases given a sufficiently low temperature in the envelope (ie T < 13K). Similar situations have been considered by Boss (1997) - model 2 - and Whitworth et al (1998) - model 1. Whitworth et al (1998) shows that the temperature drop of model 1 leads to a dynamical instability and subsequent collapse and fragmentation. Boss (1997) showed that a case similar to model 2 will also collapse and fragment. The only difference between these two being that model 1 would collapse and fragment sooner than model 2. If the core is magnetically supported, the inner region of model 1 will have a higher ambipolar diffusion velocity than model 2. However in both models previous work suggests that L1689B will ultimately collapse to form a star.

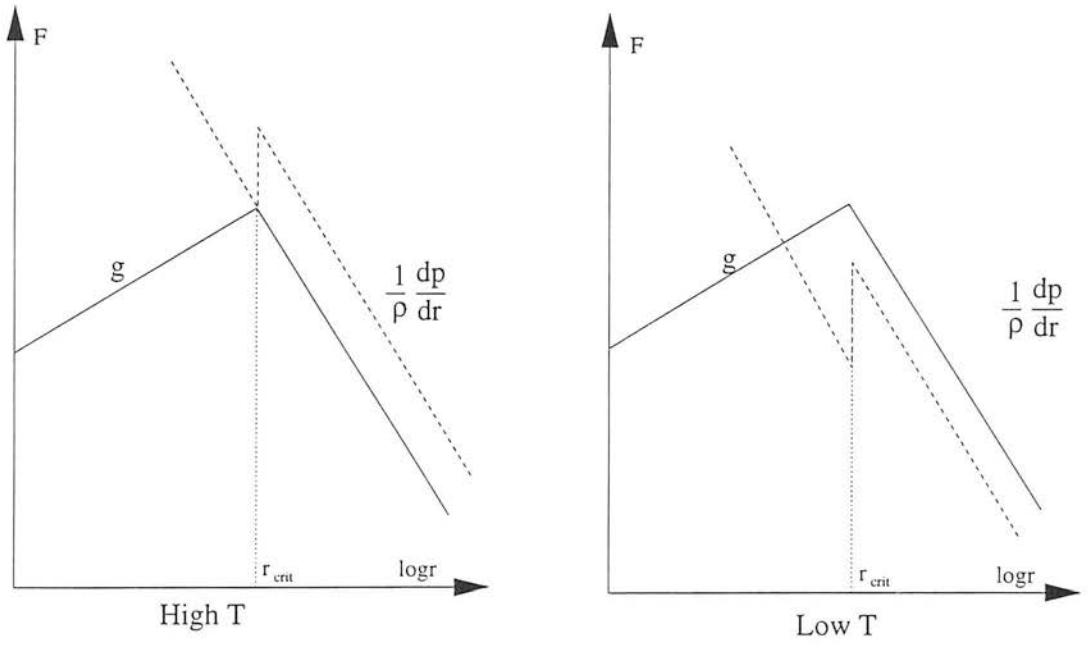

Figure 5.11: Sketch showing the local gravity, the pressure and the force due to pressure gradients. The sketch shows the results for a cold and a relatively hot core. The solid line shows the gravitational force, the dashed line shows the force due to pressure gradients in model 2, while the dotted line shows the force due to pressure gradients in model 1. For relatively hot cores the central region of model 1 experiences a net inwards force while its envelope experiences a net outwards force. Model 2 experiences an outwards force everywhere. For cool cores, both model's experience a net inwards force throughout, only the very inner region of the model 2 experiences an outwards force which is likely to be short lived. For L1689B the boundary between the two scenarios is estimated to occur when the envelope's temperature is $\sim$ 13K.

5.7 Conclusions

A simple model for the core L1689B has been presented which is parameterised in such a way that one can investigate the constraints that observations of the core place on the physical processes occurring in L1689B. It is found that the continuum places constraints on the temperature and density profiles of the cores. Analysis of the molecular radiative transfer shows that a simple model which assumes an isothermal structure and constant CO abundance cannot predict its appearance, the core must either have a drop in temperature towards its centre or a drop in CO abundance. To obtain a consistent fit between the molecular and continuum appearance of L1689B the abundance of CO must fall towards the centre.

Several problems which make the derivation of a unique solution, given the data, for the structure of L1689B have been discussed, among them microturbulence profiles, ortho to para ratios, geometry, and dust molecule interactions. Two models are proposed: one assuming that an increased density leads to a drop in temperature. The second assumes that the core is isothermal and the CO abundance drops steeply. Both scenarios have short free fall timescales. If the temperature of L1689 is less than $\sim$ 13K both models are unstable. Even if the temperature is greater than this value the inner region of L1689B is unstable if the temperature towards the centre drops. If L1689B is gravitationally unstable it is likely that some other form of support, most likely due to magnetic fields, is occurring within the inner core.

Chapter 6

Summary and Conclusions

6.1 Overview

In this thesis I have studied star formation in molecular clouds. I started by presenting a study of the star formation in low opacity, isolated clouds drawn from an all sky database. Using various techniques, I derived the typical physical conditions occurring in the densest regions of these clouds, and found statistical evidence that they do form stars, though somewhat more slowly than denser and more opaque clouds. The final conclusions of this study seemed to indicate that star formation in a wide range of different environments (including Bok globules and a range of different molecular clouds) might be describable in terms of one general theory of star formation.

In the second half of the thesis I studied individual examples of cloud cores which have not formed stars, with the aim of trying to investigate the physical processes in the interstellar medium that lead up to the formation of a star. Because detailed observational maps were available one particular core, L1689B, was investigated in detail. Using the tools of radiative transfer modelling, I found that several physical characteristics of the core could be inferred. On further study these proved to place strong constraints on the possible future evolution of the core. Although this work concentrated on only one core, some of the techniques developed, and methods used, may well prove applicable to a wider sample of objects, allowing conclusions to be drawn about the general star formation process.

6.2 Star Formation

I began by presenting a summary of what is known about the star formation process in the Galaxy. In particular those areas relevant to the work later in the thesis were discussed. I presented, amongst other things, the measured initial mass function of stars in the solar neighbourhood, and the structure and constituents of the inter stellar medium. I outlined the evidence that star formation is observed to occur in molecular clouds, and in particular in the most opaque, and dense regions of these clouds, referred to as cloud cores. I also discussed the star formation efficiency observed in different environments within the Galaxy, and the possible evidence for two different modes of star formation, one which produces high mass stars, the other only low mass stars.

I discussed the evolution leading to the formation of low mass stars in cloud cores, with reference to both theoretical work and observations. I argued that an understanding of this part of the star formation process is of particular relevance to later protostellar evolution.

Chapter 2 was a summary of the basic physics which would be used in the thesis. I presented the radiative transfer which would be used later to help interpret astronomical observations. I also discussed some of the key physical processes believed to be relevant to the formation of stars within the inter stellar medium, in particular the physics of thermal and magnetic support. Ambipolar diffusion was presented as a possible way to overcome magnetic support, and both the ambipolar diffusion velocity and the ambipolar diffusion timescale were derived.

6.3 Cloud Cores

The aim of chapter 3 was to produce a catalogue of cloud cores situated in medium opacity, isolated molecular clouds, and then investigate what role, if any, these cores play in the overall process of low mass star formation within the Galaxy. I developed a technique for identifying and producing optical depths maps of isolated clouds using the ISSA dataset (the IRAS Sky Survey Atlas) and the uncertainties and errors associated with the technique were outlined.

A number of isolated medium opacity clouds were then selected and presented along with estimates of their distances (mainly using associations with known clouds or complexes). From these clouds a set of cores were catalogued and the size, column density and mass of each core was derived. The errors associated with these derived properties were discussed, and the principle amongst them was found to be

due to uncertainties in the the dust to gas ratio and the distances to the cores.

An analysis of the cores showed that the majority are Jeans unstable, which implies that they are likely to contract or collapse. Evidence of star formation in a small number of the cores was found: several of the cores have IRAS point sources associated with them which are consistent with embedded pre-main-sequence stars. These were found not to be chance associations, and I therefore concluded that the cores in isolated low opacity clouds are forming stars and do contribute to the Galactic star formation process.

6.4 Ambipolar Diffusion

A comparison of the star formation in isolated medium opacity clouds, with similar studies of Bok Globules and high opacity molecular cloud cores was also presented in chapter 3. Three key properties were derived for each study: the typical optical depth of the cores; the typical volume densities of the cores; and a statistical estimate of the timescale taken for stars to form in the cores (the prestellar timescale). A clear trend was found for the prestellar timescale to decrease as both the typical opacity and volume density of the cores increases, and a simple $\tau \propto n^{-0.85}$ trend was discovered (where τ is the prestellar timescale and n is the volume density in the cores). No other obvious difference in prestellar timescale was seen - a fact that is surprising given the very different environments of Bok globules, and cloud cores situated in larger star forming molecular clouds. The $\tau \propto n^{-0.85}$ trend is inconsistent with a simple model of molecular clouds where thermal support is dominant. In this model the cores would collapse to stars on a timescale comparable to the free fall timescale. This timescale not only varies as $n^{-0.5}$, but is also too small by an order of magnitude to explain the observations. The ambipolar diffusion timescale is expected to be larger than the free fall timescale and in chapter 2 I had already shown that the ambipolar diffusion rate was proportional to the ionization level in a cloud. This ionization could be caused by cosmic rays alone (in which case one expects $\chi_e \propto n^{-0.5}$ eg Mouschovias 1991), or cosmic ray *and* UV ionization (in which case $\chi_e \propto n^{-0.75}$ eg McKee 1989). This latter model proved consistent with the data within the errors. I therefore concluded that $\tau \propto n^{-0.85}$ is consistent with ambipolar diffusion models if the ionization in cloud cores is due to both cosmic rays and the interstellar U.V. field.

The assumptions used to draw these conclusions were discussed, and it was emphasised that a very simple star formation model was assumed. In particular the conclusions are dependent on the assumption that the luminosity function or initial mass function of the protostellar sources found in cloud cores does not vary significantly from study to study. Another assumption is that all the cores without stars in

each sample will go on to form stars (ie are prestellar), and not be disturbed by external factors, like supernovae or shocking.

6.5 Spectroscopic Observations

In chapter 4, I presented an observational study of cloud cores without stars, which had previously been studied and detected in the submillimetre continuum. I observed the cores in a number of millimetre and submillimetre spectral lines (mainly concentrating on $C^{18}O$) and the results were presented. I discussed the methods used to reduce the observations, and the errors associated with the pointed observations and maps. I investigated in detail what features in the maps should be interpreted as real, and presented a method for setting contour levels which ensures that random features produced by noise are not displayed. I also found (unsurprisingly) that there is a trade off between velocity resolution and signal to noise in the maps.

Several of the cores were detected in $C^{18}O(J=3\rightarrow2)$ and mapped in $C^{18}O(J=2\rightarrow1)$. Only one core, L1689B, was found to be particularly bright in the $C^{18}O$ transitions (perhaps because it is situated in the relatively warm Ophiuchus cloud) and was mapped with enough signal to noise to allow a detailed study. L1689B shows evidence of velocity structure but, perhaps surprisingly, there is no indication of rotation - if anything the velocity structure is indicative of slow contraction.

6.6 Modelling L1689B

In chapter 5, I presented a model of L1689B and investigated what constraints the molecular observations and previously published continuum data (Andre et al 1996) put on the structure of L1689B. The millimetre continuum appearance of the model was derived, and by comparison with the actual 1.3mm appearance of L1689B I found that one could *rule out* the simple singular isothermal sphere model of L1689B. The continuum observations seem to predict that L1689B has too flat a density profile in its inner regions to be consistent with the simple singular isothermal sphere. The $C^{18}O$ appearance of the model was also investigated with the help of a radiative transfer code. Comparison of the model's predictions with the $C^{18}O$ observations also confirmed that a simple singular isothermal sphere model for L1689B is inappropriate. In order to predict the molecular appearance of L1689B, the model had to have a flattened inner density profile , *and* either a temperature fall, a $C^{18}O$ abundance fall towards the centre, or possibly some combination of the two.

I found that in order to explain both the continuum and molecular appearance of L1689B simultaneously a temperature drop alone was inadequate; it was necessary to invoke a drop in $C^{18}O$ towards the centre of L1689B. However, because of uncertainties in the details of gas/dust interactions and the effect that freezing out of CO would have on the opacity of the dust, it was not possible to find a unique solution describing L1689B. A number of models were found to be consistent with the data.

Two scenarios were therefore presented. One was a model in which the temperature in the centre of the cores falls, and some $C^{18}O$ freezes out of the gas phase onto the dust grains. The other model presented is isothermal but has an even steeper drop in $C^{18}O$ abundance. Both models were found to predict the $C^{18}O$ appearance of L1689B. However it is difficult to decide which is more consistent with the continuum data.

Both these models were found to have a Jeans mass below the actual mass observed for L1689B and it's surroundings. I found that for the model with a falling temperature in L1689B the centre is unstable because of a lack of pressure gradients to support it against its own self gravity. Because of a short free fall timescale, it is unlikely that this core would be observed unless it was supported by magnetic fields. The envelope of L1689B, and the central region (if L1689B is isothermal), were found to become susceptible to collapse if the envelope is less than about 13K.

Therefore I predict two possible mechanisms by which L1689B can be forming a star. One is the loss of thermal support in the centre, due to a fall in central temperature. The other is an overall loss of thermal support due to the whole core cooling below 13 K. Unfortunately the observations presented were not capable of proving beyond doubt whether either situation is occurring.

6.7 Future Work

Three of the basic assumptions commonly made in models of of star formation are worth investigating in the light of this thesis. Specifically they are the assumptions that cloud cores forming stars are 1) isothermal, 2) ionized predominantly by cosmic rays, and 3) of homogeneous density structure (ie not clumped on small scales). Assumption 3 is particularly important because it is implicit in many of the conclusions reached in the second half of this work.

These assumptions can be tested in two ways. Firstly through new observational studies of cloud cores, designed specifically to check the assumptions, and secondly by improving the methodologies used to analyse the observations.

A molecular study of a selected sample of cloud cores, in particular $C^{18}O$, an optically thin tracer of column density, observed in various millimetre and submillimetre transitions, with telescopes like IRAM and the JCMT, could be combined with millimetre observation of CS, a known volume density tracer. The degeneracy which exists between molecular freezing out and falling temperature could then be lifted by comparison with dust maps of the cores using the Sub Millimetre Bolometer Array (SCUBA) on the JCMT, and detailed modelling of the relationship between CO abundances on dust mantles and the dust opacity.

The code used in this work assumed homogeneous density distributions. Improving the code, allowing modelling of cores with clumping, would help to check the effects of this assumption and is perhaps achievable by introducing more than one population of gas within each volume element in the model or (though numerically more demanding) by using Monte Carlo methods.

The prestellar lifetimes derived in chapter 3 were effectively based on the assumption that all cloud cores experience a single burst of star formation, which forms stars from the same IMF, and that the resultant YSOs evolve in the same way - ie have similar lifetimes, accretion rates, and luminosities. The only way that this assumption can be tested is by making a detailed study of the YSO content of more than one set of cores. A study of two of the sets of cores presented, both in the infrared and the submillimetre could investigate the population of YSOs in each sample, by allowing a derivation of the spectral indices, the luminosity function of the sets of YSOs and their spectral classifications (Andre et al 1993). Such a study should allow a comparison of the typical masses and ages of YSOs in each set of cores, and will verify or cast doubt on the assumptions made that different sets of cores with different typical densities and physical conditions, lead to the formation of stars from a common IMF.

Two specific comparisons between the cores' YSO populations are possible. Submillimetre continuum observations preferentially detect young Class-0 objects; Infrared, the later Class Is and IIs. Any difference in the fraction of early to late type YSOs between the two samples would be indicative of different star formation histories in the two sets of cores.

In addition the typical luminosities of the YSOs could be compared. Higher luminosities are expected either because of higher mass YSOs or higher accretion rates (Beichman et al 1986), hence a marked difference in luminosity between the two sets of objects, will be a clear indication of either a different IMF for the two samples, or a different YSO lifetime. This comparison is particularly dependent on an accurate knowledge of the distance to the cores.

A subsample of the two catalogues produced by Wood et al (1992) and Myers et al (1983) would

almost certainly be the best. Not only do they they differ in typical densities by a factor of 4, and differ in the fraction of cores with young stellar objects, and hence the inferred prestellar timescale by a factor of 2, but they are also associated with large molecular clouds which means the distances to the cores are likely to be better known than for Bok globules, or medium opacity, isolated clouds. If no difference is found in the two populations this will confirm the conclusions reached in chapter 3, if not it will reveal a difference in the type of stars formed between the two sets of cloud cores.

In the last 100 years we have come to understand the nature of stars. How they form is however a more complicated and diverse problem which has proved much more enduring. This thesis has examined some small aspects of this problem, but much work remains to be done.

Bibliography

[1] Abt, H., Levy, S.G., 1976, ApJS, 30, 273

[2] Adams, F.C., Benz, W., 1992, McAlister, H.A., Hartkopf, W.I., (eds), in Compilmentary Approaches to Star Double and Multiple Star Research, IAU Colloqium 135

[3] Adams, F.C., Lada, C.J., Shu, F.H., 1987, ApJ, 312, 788

[4] Andre, P., 1997, in The Far Infrared and Submillimetre Universe, ASA Symposium 401

[5] Andre, P., Ward-Thompson, D., Barsony, M., 1993, ApJ, 406, 122

[6] Andre, P., Ward-Thompson, D., Motte, F., 1996, AA, 314, 625

[7] D'Antona, F., Mazzitelli, I., 1997, in Evolution of Low mass stars, eds Pallavicini, R., Micela, G., Mem.S.A.It., 68, no 4

[8] Bazell, D., Désert, F.X, 1988, ApJ, 333, 353

[9] Beard, S.M., MacGillivray, H.T., Thanisch, P.F., 1990, MNRAS, 247, 311

[10] Beichman, C.A., Myers, P.C., Emerson, J.P., Harris, S., Mathieu, J.P., Benson, P.J., Jennings, R.E., 1986, ApJ, 307, 337

[11] Beichman, C.A., 1987, ARAA, 25, 521

[12] Beichman, C.A., Neugebauer, G., Habing, H.J., Clegg, P.E., Chester, T.J. (Eds), 1988, Infrared Astronomical Satellite Catalogs and Atlases Explanatory Supplement , NASA RP-1190, Vol 1, US Goverment Printing Office, Washington D.C.

[13] Bergin, E.A. Langer, W.D., ApJ, 1997, 486, 316

[14] Berry, D., Starlink User Document ID29.0.

[15] Bonnor, W.B., 1956, MNRAS, 3, 351

[16] Boss, A. P., 1997, ApJ, 483, 309

[17] Bourke, T.L. Hyland, A.R., Robinson, G., 1995, MNRAS, 276, 1067

[18] Buckley, H. D., 1997, PhD Thesis, University of Edinburgh

[19] Burton, W.B., in Galactic and Extragalactic Radio Astronomy, eds Verschur, G.L., Kellermann, K.I., (1988), New York: Springer Verlag

[20] Cao, Y., Terebey, S., Prince, T.A., Beichman, C.A., 1997, ApJS, 111, 387

[21] Chandler, C.J., Gear, W.K., Sandell, G., Hayashi, S., Duncan, W.D., Griffin, M.J., Hazella, S., 1990 MNRAS, 243, 330

[22] Clark, C., 1995, Wijers, R.A.M.J., Davies, M.B., Tout, C.A., (eds), in Evolutionary Processes in Binary Stars, Kluwer Academic Publishers

[23] Clemens, D.P., Barvainis, R., 1988, ApJS, 68, 257

[24] Clemens, D.P., Sanders, D.B., Scoville, N.Z., 1988, ApJ, 327, 139

[25] Clemens, D.P., Yun, J.L., Heyer, M.H., 1991, ApJS, 75, 877

[26] Combes, F., 1991, ARAA,29,195

[27] Cox, D.P., Reynolds, R.J., ARAA, 1987, 25, 303

[28] Cunningham, C. T., Hayward, R. H., Wade, J. D., Davies, S. R., Matheson D. N., 1992, Int. J. Infrared Millimetre Waves, 13, 1827

[29] Dame, T.M., Ungerechts, H., Cohen, R.S., De Geus, E.J., Grenier, I.A., May, J., Murphy, D.C., Nyman, L.-A., Thaddeus, P., 1987, ApJ, 322, 706

[30] Davies, S. R., Cunningham C. T., Little L. T., Matheson D. N., 1992, Int. J. Infrared Millimetre Waves, 13, 647

[31] Diamond, C.J., Jewell, S.J., Panman, T.J., 1995, MNRAS, 274, 589

[32] Dring, A.R., Linsky, J., Murthy, J., Henry, R.C., Moos, W., Vidal, Madjar, A., Audouze, J., Landsman, W., 1997, ApJ, 488, 760

[33] Duley, W.W., Williams, D.A., 1984, Interstellar Chemistry, Academic Press

[34] Duquenney, A., Mayor, M., 1991, AA, 248, 485

[35] Elmegreen, B. G., 1990, ApJ, 357, 125

[36] Elmegreen, B.G., Falgarone, E.,1996, ApJ, 471, 816

[37] Emerson, D., 1996, Interpreting Astronomical Data, John Wiley and Sons

[38] EMLT, Figaro Users Guide, Starlink Document MUD/13

[39] Flower, D.R., Launey, J.M., 1985, MNRAS, 214, 275

[40] Foster, P.N., Chevalier, R.A., 1993, ApJ, 416, 303

[41] Gammie, C.F., Ostriker, E.C., 1996, ApJ, 466, 814

[42] Gautier, T.N., Boulanger, F., Pérault, M., Puget, J.L., 1992, AJ, 103, 1313

[43] Greaves, J.S., Ohishi,M., White, G.J., Sunada, K., 1995, AA, 299, 591

[44] Grenier, I.A., Lebrun, F., Arnaud, M., Dame, T.M., Thaddeus, P., 1989, 347, 231

[45] Hartmann, D., Burton, W.B., 1997, Atlas of Galactic Neutral Hydrogen, Cambridge University Press

[46] Heaton, B.D., Little, L.T., Yamashita, T., Davies, S.R., Cunningham, C.T., Moteiro, T.S., 1993, AA, 278, 238

[47] Herbig, G.H., 1962, Advances in Astronomy and Astrophysics, Volume 1

[48] Hildebrand, R.H., 1983, QJRAS, 24, 267

[49] Jeans, J.H., 1902, Phil. Trans. of Roy. Soc. London, 199,1

[50] Koo, B.-C., Heiles, C., Reach, W.T., 1992, ApJ, 390, 108

[51] Krugel, E, Chini, R., 1994, AA, 287, 947

[52] Kuiper, T.B.H., Langer, W.D., Velusamy, T., 1996, ApJ, 468, 41

[53] Kutner, M. L., Ulich B. L., 1981, ApJ, 250, 341

[54] Lada, C.J., Wilking, B.A., 1984, ApJ, 287, 610

[55] Lada, C.J., in Star Forming Regions, IAU Symposium 115, eds Peimbert, M., Jugaku, J, D. Reidel Publishing Company (1985)

[56] Lada, C., in Molecular Clouds and Star Formation, eds Yuan C., You J., World Scientific Publishing (1995).Supplement

[57] Lang, K.R., Astrophysical Data I Planets and Stars, 1992, Springer-Verlag

[58] Langer, W.D., Wilson, R.W., Goldsmith, P.F., Beichman, C.A., 1989, ApJ, 337, 355

[59] Larson, R.B., 1969, MNRAS, 145, 271

[60] Larson, R.B., 1981, MNRAS, 194, 809

[61] Lemme, C., Wilson, T.L., Tieftrunk, A.R., Henkel, C., 1996, AA, 312, 585

[62] Li, Z-Y, McKee, C.F., 1996, ApJ, 464, 373

[63] Loren, R.B., 1989, ApJ, 338, 902

[64] Lublow, S.H., Pringle, J.E., 1986, MNRAS, 279, 1251

[65] Lynds, B.T., 1962, ApJS, 7, 1

[66] Lynds, B.T., 1965, ApJS, 12, 163

[67] athews, H., JCMT Astronomers Reference Manual

[68] Mazeh, T., Goldberg, D., Duquennoy, A., Mayor, M., 1992, ApJ, 401, 265

[69] McCartney, M.S.K., 1997, PhD Thesis, University of Edinburgh

[70] McClaughlin, D.E., Pudritz, R.E., 1997, ApJ, 476, 750

[71] McKee, C.F., 1989, ApJ, 345, 782

[72] Mestel, L., Spitzer, L., 1956, MNRAS, 116, 503

[73] Mouschovias, T.S., Paleologue, E.V., 1980, ApJ, 237, 877

[74] Mouschovias, T.C., in The Physics of Star Formation and Early Stellar Evolution, eds Lada C.J.,Kylafis, N.D., 1991, Kluwer Academic Publishers

[75] Myers P.C., 1983, ApJ, 270, 105

[76] Myers, P.C., Linke, R.A., Benson, P.J., 1983 ApJ, 263, 716

[77] Myers, P.C., Benson, P.J., 1983, ApJ, 266, 309

[78] Myers, P. C., Dame, T. M., Thaddeus, P., Cohen, R. S., Silverberg, R. F., Dwek, E., Hauser, M. G., 1986, ApJ, 301, 398

[79] Myers, P.C. Mardones, D., Tafalla, M., Williams, J.P, Wilner, D.J., 1996, ApJ, 465, 133

[80] Ossenkopf, V., Henning. T, 1994, AA, 296, 797

[81] Padman, R., 1990, Specx Users Manual. MRAO, University of Cambridge